

THE UNIVERSITY OF NOTTINGHAM
SIR PETER MANSFIELD IMAGING CENTRE
SCHOOL OF PHYSICS AND ASTRONOMY

Developing Techniques for Quantitative Renal Magnetic Resonance Imaging

Author:
Alexander James DANIEL MSci

Supervisor:
Prof. Susan FRANCIS

29th January, 2021



Thesis submitted to the University of Nottingham for the degree of Doctor of Philosophy

Abstract

Science will happen, but this bit can be read by muggles on ‘tinterweb.

Contents

Abstract	i
Acknowledgments	vii
Abbreviations	viii
1 Introduction	1
1.1 Imaging in the Clinic	1
1.2 Clinical Motivation	2
1.3 Thesis Overview	4
1.4 References	6
2 Principles of Nuclear Magnetic Resonance Imaging	9
2.1 Source of the NMR Signal	10
2.1.1 Nuclear Spin	10
2.1.2 Application of an External Magnetic Field	11
2.1.3 Precession	12
2.1.4 Resonance	13
2.2 Relaxation and Contrast Mechanisms	14
2.2.1 Longitudinal Relaxation (T_1)	14
2.2.2 Transverse Relaxation (T_2 and T_2^*)	16
2.2.3 Dipole-Dipole Interactions	20
2.2.4 Diffusion Imaging	22
2.2.5 Optimisation of Tissue Contrast	23
2.3 Forming an Image	24
2.3.1 Signal Localisation	24
2.3.2 Image Acquisition Acceleration	30

2.3.3	Image Acquisition Schemes	32
2.4	Conclusion	37
2.5	References	38
3	Assessment of Renal T_2 Mapping Methods	39
3.1	Introduction	40
3.1.1	Theory	41
3.2	Methods	41
3.2.1	Acquisition Schemes	41
3.2.2	Post Processing	45
3.3	Results	47
3.3.1	Sequence Accuracy	47
3.3.2	Image Quality	50
3.3.3	In-Vivo	50
3.4	Discussion	54
3.5	Conclusion	54
3.6	Acknowledgements	54
3.7	References	55
4	Quantitative Methods to Measure Renal Oxygenation	59
4.1	Introduction	60
4.2	Methods	62
4.2.1	Susceptibility-Based Oximetry	62
4.2.2	T_2 Relaxation Under Spin Tagging	63
4.2.3	Inducing Changes in Oxygenation of Blood in the Renal Vein	69
4.3	Results and Discussion	71
4.3.1	Susceptibility-Based Oximetry	71
4.3.2	T_2 Relaxation Under Spin Tagging	73
4.4	Conclusions and Future Work	80
4.5	Acknowledgements	80
4.6	References	81
5	Automated Segmentation of Kidneys using Machine Learning	85
5.1	Introduction	87
5.2	Neural Networks for Image Segmentation	90
5.2.1	Artificial Neural Networks	90

5.2.2	Convolutional Neural Networks	93
5.3	Methods	95
5.3.1	MRI Data Acquisition	95
5.3.2	Manual Segmentation	96
5.3.3	Automated Segmentation Using a CNN Architecture	96
5.3.4	Statistical Analysis	99
5.4	Results	100
5.4.1	Characteristics of the Training Cohort	100
5.4.2	Reducing Acquisition Time	101
5.4.3	Accuracy of Manual Segmentation	102
5.4.4	Network Testing	104
5.5	Discussion	109
5.5.1	Evaluation of Methodology	110
5.5.2	Future Directions	112
5.6	Conclusions	114
5.7	Acknowledgements	114
5.8	References	115
6	Ex-Vivo Renal MRI	120
6.1	Introduction	121
6.2	Methods	123
6.2.1	Sample Acquisition and Fixation	123
6.2.2	T_1 Mapping	123
6.2.3	T_2 Mapping	125
6.2.4	T_2^* Mapping	126
6.2.5	Apparent Diffusion Coefficient	127
6.2.6	Diffusion Tensor Imaging	127
6.2.7	Layer Based Analysis	129
6.3	Results and Discussion	132
6.3.1	Fixation and Protocol Development	132
6.3.2	Monitoring Changes in MR Parameters Post Fixation	134
6.3.3	Comparing MR and Histological Measures in Aged Kidneys	139
6.4	Conclusions and Future Work	140
6.4.1	Protocol Validation on a Single Sample	141
6.4.2	Ex-Vivo Sample Coil	141

6.4.3	Human Organs	142
6.5	Acknowledgements	142
6.6	References	143
7	Conclusion	146

Todo list

█	Diagrams	2
█	Make sure these are in the correct order	4

Acknowledgements

Finally thank you to covid-19 for removing enough distractions to motivate me to write this thesis.

Abbreviations

ADC	Apparent Diffusion Coefficient
ADPKD	Autosomal Dominant Polycystic Kidney Disease
AKI	Acute Kidney Injury
ANN	Artificial Neural Network
ASL	Arterial Spin Labelling
BOLD	Blood Oxygen Level Dependent
CBF	Cerebral Blood Flow
CKD	Chronic Kidney Disease
CMRO₂	Cerebral Metabolic Rate of Oxygen
CNN	Convolutional Neural Network
CoV	Coefficient of Variation
CPMG	Carr-Purcell-Meiboom-Gill
CSF	Cerebrospinal Fluid
CT	Computed Tomography
DTI	Diffusion Tensor Imaging

eGFR	Estimated Glomerular Filtration Rate
EPI	Echo Planar Imaging
eTE	Effective Echo Time
ETL	Echo Train Length
FA	Flip Angle
FAIR	Flow-sensitive Alternating Inversion Recovery
FFE	Fast Field Echo
FID	Free Induction Decay
FOV	Field Of View
FSE	Fast Spin Echo
FSL	fMRI Software Library
GE	Gradient Echo
GFR	Glomerular Filtration Rate
GPU	Graphical Processing Unit
GraSE	Gradient Spin Echo
GUI	Graphical User Interface
H and E	Haematoxylin and Eosin
HASTE	Half-Fourier Single-shot Turbo spin Echo
HC	Healthy Control
ICC	Intraclass Correlation
ISMRM	International Society of Magnetic Resonance in Medicine

LSTM	Long Short-Term Memory
ME-TSE	Multi-Echo Turbo Spin Echo
MRI	Magnetic Resonance Imaging
NBF	Neutral Buffered Formalin
NHS	National Health Service
NIST	National Institute of Standards and Technology
NMR	Nuclear Magnetic Resonance
PBS	Phosphate-buffered Saline
PC	Phase Contrast
PET	Positron Emission Tomography
PLD	Post Label Delay
PSD	Pulse Sequence Diagram
PSF	Point Spread Function
PRELUDE	Phase Region Expanding Labeller for Unwrapping Discrete Estimates
RARE	Rapid Acquisition with Relaxation Enhancement
RBF	Renal Blood Flow
RNN	Recursive Neural Network
ReLU	Rectified Linear Unit
RF	Radio Frequency
RMRO₂	Renal Metabolic Rate of Oxygen
ROI	Region Of Interest

SAR	Specific Absorption Rate
SBO	Susceptibility Based Oximetry
SD	Standard Deviation
SE	Spin Echo
SENSE	Sensitivity Encoding
SNR	Signal to Noise Ratio
SPMIC	Sir Peter Mansfield Imaging Centre
TE	Echo Time
TFE	Turbo Field Echo
TFEPI	Turbo Field Echo Planar Imaging
TI	Inversion Time
TILT	Transfer Insensitive Labelling Technique
TKV	Total Kidney Volume
TLCO	Twelve Layer Concentric Objects
TR	Repetition Time
TRUST	T_2 Relaxation Under Spin Tagging
TSE	Turbo Spin Echo
UKKW	United Kingdom Kidney Week
WET	Water suppression Enhanced through T_1 effects

Chapter 1

Introduction

1.1 Imaging in the Clinic

From April 2019 to March 2020, the United Kingdom's National Health Service (NHS) performed 45 million medical imaging procedures, of these 4 million were Magnetic Resonance Imaging (MRI)[1]. This technique can be used to produce high resolution volumetric images of the body with exquisite soft tissue contrast. Unlike other modalities, such as Computed Tomography (CT) and Positron Emission Tomography (PET), MRI uses non-ionising radiation, making it more suitable for longitudinal analysis of patient progression and research involving healthy volunteers.

The superior soft tissue contrast of MRI compared to CT meant it first found widespread clinical adoption in the field of neuroimaging. Here MRI has been used for diagnosis of neurological disorders, monitoring treatment progression and research into cognition. Many of the techniques honed in the brain, can be applied to the abdomen, where similar tissue properties can exploit the same techniques; albeit in a somewhat more challenging environment due to respiratory motion and a more inhomogeneous tissue structure. The kidneys are ideally suited to this translation as they have similar tissue properties to the brain and are highly dynamic organs.

In addition to the acquisition of basic structural images, MRI can be used to collect quantitative information about the tissues being imaged. In this situation the numerical voxel values have physical significance, rather than simply representing signal intensity in

1.2. Clinical Motivation

arbitrary units [2]. Using quantitative MRI properties such as an organs oxygen consumption [3], perfusion [4], stiffness [5] and temperature [6] can be measured. Although many quantitative MRI techniques have been developed for the the kidneys, there is still many methods where development, translation from the brain or standardisation with the wider renal community would be highly desirable.

1.2 Clinical Motivation

The kidneys are two bean shaped organs found in the abdomen, just below the rib cage, symmetrical about the spine. They participate in the control of bodily fluids by regulating the balance of electrolytes, excreting waste product of metabolism and excess water from blood into urine [7].

Kidneys are made up of units called nephrons, each of which contains a renal corpuscle and a tubule. The renal corpuscle itself is made up of a glomerulus and a Bowman capsule. The glomerulus is a cluster of capillaries that allow wastes and fluid to pass out of the blood stream into the Bowman capsule, while larger structures such as blood cells and proteins remain in the blood. The substances that passed through the glomerulus are moved to the tubules, each of which has blood vessels running alongside; these vessels reabsorb many of the important components of the blood such as the majority of the water, minerals and nutrients. The remaining fluids and waste in the tubules are collected in the ureter and removed from the body [8].

Diagrams

Tissue in the kidney is separated into renal cortex, the outer portion of the kidney and renal medulla, the inner portion. The cortex contains the corpuscles with the tubules passing from the cortex to the medulla. Medullary tissue is compartmentalised into renal pyramids. Blood is supplied to the kidney via the renal artery, this branches into smaller vessels until it reaches the glomeruli then flows out via the renal vein.

Due to their vital function in the body and the toxins they encounter as they perform their role, the kidneys are susceptible to problems. Chronic Kidney Disease (CKD) is the progressive destruction of the kidneys and therefore decrease in renal function. More quantitatively, CKD can be assessed clinically by Glomerular Filtration Rate (GFR), the rate at which fluid is filtered through the kidneys, with a value below $60 \text{ ml/min}/1.73\text{m}^2$ of

1.2. Clinical Motivation

body surface area being diagnostic or the presence of albumin, the main protein in blood plasma, in the patients urine [9–11]. Common causes of CKD are high blood pressure and diabetes as these damage the nephrons with high blood pressure also posing a risk to the blood vessels within the kidney. Renal tissue is highly vascularised and as such, the risks associated with high blood pressure are especially prevalent in the kidneys. An estimated 5–11% of the global population suffer from CKD [12–16] making it a significant public health concern. Late referral of renal disorders results in an increase in mortality rate and treatment costs [17–19]. Given that in 2013/2014 renal services cost the NHS £586 million [20] there are clear health and economic advantages to an early diagnosis and improved treatment of CKD. This can either be achieved via directly aiding diagnosis i.e. developing tools used on to assess patients condition and tailor treatment, or via improving understanding of CKD leading to an earlier, more accurate diagnosis using existing techniques and thus more personalised medicine.

The current methods available to study CKD are not ideal for a variety of reasons. Histological samples are the gold standard for studying renal tissue however collecting them is an invasive process and as such they are not suitable for monitoring the progress of a patient's condition on a regular basis. This coupled with the fact that a small sample is not representative of the entirety of both kidneys means that this method has large drawbacks. Ultrasound can be used to gather structural information about the kidneys non-invasively, however, it suffers from low spatial resolution and the images being difficult to interpret [21]. The most common method of diagnosis is to estimate GFR from the creatinine content in a blood sample however this measure does not allow for the individual assessment of each kidney and is an indirect measure of kidney tissue damage.

MRI is an ideal modality for the study of kidney disease due to its non-ionising, non-invasive and quantitative nature. A current research interest at the Sir Peter Mansfield Imaging Centre (SPMIC) is the use of a multi-parametric quantitative renal MRI protocol to assess and predict CKD [22, 23]. This protocol is used to measure multiple quantitative properties of the kidneys with relative increases/decreases between measurements functioning as biomarkers and therefore indications of CKD progression. The implementation of new quantitative renal imaging methods can improve this protocol, thus increasing its clinical application. In addition to the CKD paradigm, we wish to apply these methods ex-vivo, both to allow a more direct comparison with current gold standards, such as histopathology, and to aid with assessment of renal allograft viability.

1.3 Thesis Overview

Chapter 2 provides the theoretical framework of Nuclear Magnetic Resonance (NMR) and MRI. A detailed description is given of the origin of the measured signal, processes that give rise to contrast between tissues and the methods of image formation.

Chapter 3 explores T_2 mapping within the kidneys. There is little consensus as to which method should be used within the kidneys [24], thus leading to inconsistent values quoted between studies [25]. Here multiple methods from the literature are compared assessing their quantitative accuracy and image quality in phantoms before five subjects are scanned to assess the methods in-vivo.

Chapter 4 aims to translate methods for measuring blood oxygenation from vessels in the brain to use within the kidneys. Focusing on Susceptibility Based Oximetry (SBO) [26] and T_2 Relaxation Under Spin Tagging (TRUST) [27] this chapter optimises the methods for use in the abdomen, verifying the modifications in the brain, then carries out an oxygen challenge in-vivo to measure changes in oxygen saturation within the renal vein.

Chapter 5 describes the development of a fully automated method to segment the kidneys from MRI data. Defining renal masks is an important, yet time consuming, aspect of many studies. The masks can be used to calculate Total Kidney Volume (TKV) or to inform downstream processing. Here a Convolutional Neural Network (CNN) is developed to segment the kidneys from T_2 weighted Half-Fourier Single-shot Turbo spin Echo (HASTE) images. Software is developed to provide an executable that allows anyone to segment the kidneys in a few seconds on regular office hardware.

Chapter 6 develops methods for scanning kidneys ex-vivo. The clinical gold standard for diagnosis of renal pathologies is biopsy followed by histological analysis. Comparison between this gold standard and recently developed quantitative MRI techniques is vital for clinical translation. Here a pipeline for multi-parametric imaging of the same kidney in-vivo, ex-vivo followed by histology is developed.

Chapter 7 concludes the thesis, highlighting key results and their current applications. It also provides an overview as to future research directions and how the methods developed

Make
sure
these are
in the
correct
order

1.3. Thesis Overview

could be applied to new paradigms or expanded upon.

1.4 References

1. *Diagnostic Imaging Dataset Annual Statistical Release 2019/20* <https://www.england.nhs.uk/statistics/statistical-work-areas/diagnostic-imaging-dataset/diagnostic-imaging-dataset-2019-20-data/> (2021).
2. Tofts, P. *Quantitative MRI of the Brain: Measuring Changes Caused by Disease* 688 pp. ISBN: 978-0-470-84721-3. Google Books: RbFrAAAAMAAJ (Wiley, 2003).
3. Zhang, J. et al. Quantitative Mapping of Cerebral Metabolic Rate of Oxygen (CMRO₂) Using Quantitative Susceptibility Mapping (QSM). *Magnetic Resonance in Medicine* **74**, 945–952. ISSN: 1522-2594 (1st Oct. 2015).
4. Karger, N. et al. Quantitation of Renal Perfusion Using Arterial Spin Labeling with FAIR-UFLARE. *Magnetic Resonance Imaging* **18**, 641–647. ISSN: 0730-725X (1st July 2000).
5. Mariappan, Y. K., Glaser, K. J. & Ehman, R. L. MAGNETIC RESONANCE ELASTOGRAPHY: A REVIEW. *Clinical anatomy (New York, N.Y.)* **23**, 497–511. ISSN: 0897-3806 (July 2010).
6. Yuan, J., Mei, C.-S., Panych, L. P., McDannold, N. J. & Madore, B. Towards Fast and Accurate Temperature Mapping with Proton Resonance Frequency-Based MR Thermometry. *Quantitative Imaging in Medicine and Surgery* **2**, 212–232. ISSN: 2223-4306, 2223-4292 (Mar. 2012).
7. Lote, C. J. *Principles of Renal Physiology* 255 pp. ISBN: 978-94-011-4086-7. Google Books: at6LBQAAQBAJ (Springer Science & Business Media, 6th Dec. 2012).
8. Hall, J. E. *Guyton and Hall Textbook of Medical Physiology* 1171 pp. ISBN: 978-1-4557-7005-2. Google Books: 3sWNCgAAQBAJ (Elsevier Health Sciences, 20th May 2015).
9. Stevens, L. A., Coresh, J., Greene, T. & Levey, A. S. Assessing Kidney Function — Measured and Estimated Glomerular Filtration Rate. *New England Journal of Medicine* **354**, 2473–2483. ISSN: 0028-4793 (8th June 2006).
10. Farrugia, A. Albumin Usage in Clinical Medicine: Tradition or Therapeutic? *Transfusion Medicine Reviews* **24**, 58–63. ISSN: 0887-7963, 1532-9496 (1st Jan. 2010).
11. Pruijm, M., Milani, B. & Burnier, M. Blood Oxygenation Level-Dependent MRI to Assess Renal Oxygenation in Renal Diseases: Progresses and Challenges. *Frontiers in Physiology* **7**. ISSN: 1664-042X. pmid: 28105019 (5th Jan. 2017).
12. Coresh, J., Astor, B. C., Greene, T., Eknayan, G. & Levey, A. S. Prevalence of Chronic Kidney Disease and Decreased Kidney Function in the Adult US Population: Third National Health and Nutrition Examination Survey. *American Journal of Kidney Dis-*

1.4. References

- eases: *The Official Journal of the National Kidney Foundation* **41**, 1–12. issn: 1523-6838 (Jan. 2003).
13. De Lusignan, S. *et al.* Identifying Patients with Chronic Kidney Disease from General Practice Computer Records. *Family Practice* **22**, 234–241. issn: 0263-2136 (1st June 2005).
 14. Drey, N., Roderick, P., Mullee, M. & Rogerson, M. A Population-Based Study of the Incidence and Outcomes of Diagnosed Chronic Kidney Disease. *American Journal of Kidney Diseases* **42**, 677–684. issn: 0272-6386 (1st Oct. 2003).
 15. Amato, D. *et al.* Prevalence of Chronic Kidney Disease in an Urban Mexican Population. *Kidney International* **68**, S11–S17. issn: 0085-2538 (1st Aug. 2005).
 16. Chadban, S. J. *et al.* Prevalence of Kidney Damage in Australian Adults: The Aus-Diab Kidney Study. *Journal of the American Society of Nephrology* **14**, S131–S138. issn: 1046-6673, 1533-8450 (suppl 2 7th Jan. 2003).
 17. Jungers, P. *et al.* Late Referral to Maintenance Dialysis: Detrimental Consequences. *Nephrology Dialysis Transplantation* **8**, 1089–1093. issn: 0931-0509 (1st Jan. 1993).
 18. Sesso, R. & Belasco, A. G. Late Diagnosis of Chronic Renal Failure and Mortality on Maintenance Dialysis. *Nephrology Dialysis Transplantation* **11**, 2417–2420. issn: 0931-0509 (1st Dec. 1996).
 19. Klebe, B. *et al.* The Cost of Implementing UK Guidelines for the Management of Chronic Kidney Disease. *Nephrology Dialysis Transplantation* **22**, 2504–2512. issn: 0931-0509 (1st Sept. 2007).
 20. Precious, K. *NHS England » Programme Budgeting* <https://www.england.nhs.uk/resources/resources-for-ccgs/prog-budgeting/> (2017).
 21. Hansen, K. L., Nielsen, M. B. & Ewertsen, C. Ultrasonography of the Kidney: A Pictorial Review. *Diagnostics* **6**. issn: 2075-4418. pmid: 26838799 (23rd Dec. 2015).
 22. Cox, E. F. *et al.* Multiparametric Renal Magnetic Resonance Imaging: Validation, Interventions, and Alterations in Chronic Kidney Disease. *Frontiers in Physiology* **8**. issn: 1664-042X (2017).
 23. Buchanan, C. E. *et al.* Quantitative Assessment of Renal Structural and Functional Changes in Chronic Kidney Disease Using Multi-Parametric Magnetic Resonance Imaging. *Nephrology Dialysis Transplantation* (29th June 2019).
 24. Dekkers, I. A. *et al.* Consensus-Based Technical Recommendations for Clinical Translation of Renal T1 and T2 Mapping MRI. *Magnetic Resonance Materials in Physics, Biology and Medicine*. issn: 1352-8661 (22nd Nov. 2019).

1.4. References

25. Wolf, M. *et al.* Magnetic Resonance Imaging T1- and T2-Mapping to Assess Renal Structure and Function: A Systematic Review and Statement Paper. *Nephrology Dialysis Transplantation* **33**, ii41–ii50. ISSN: 0981-0509 (suppl_2 1st Sept. 2018).
26. Jain, V., Langham, M. C. & Wehrli, F. W. MRI Estimation of Global Brain Oxygen Consumption Rate. *Journal of Cerebral Blood Flow & Metabolism* **30**, 1598–1607. ISSN: 0271-678X (1st Sept. 2010).
27. Lu, H. & Ge, Y. Quantitative Evaluation of Oxygenation in Venous Vessels Using T2-Relaxation-Under-Spin-Tagging MRI. *Magnetic Resonance in Medicine* **60**, 357–363. ISSN: 1522-2594 (1st Aug. 2008).

Chapter 2

Principles of Nuclear Magnetic Resonance Imaging

Abstract

This chapter outlines the theoretical framework behind Nuclear Magnetic Resonance (NMR) and Magnetic Resonance Imaging (MRI). Beginning with an overview of nuclear spin and resonance, the origin of the signal measured in Nuclear Magnetic Resonance (NMR) is explained. The processes responsible for variations within signals such as relaxation mechanisms is then outlined in addition to techniques used to measure these different signals. Finally an overview of the process by which the signals can be used to form images is given, covering concepts such as spacial localisation, image acquisition schemes and acceleration methods.

2.1 Source of the NMR Signal

2.1.1 Nuclear Spin

The NMR signal arises from the interaction between the atomic nucleus and an external magnetic field. These atomic nuclei possess intrinsic properties, mass (m), charge (q) and spin (I). Spin is a quantum mechanical property and as such, can only take values of half integers or integers. Nuclear spin is dictated by the sum of the constituent particles of the nucleus, protons and neutrons, each of which possesses their own spin of either $1/2$ or $-1/2$ respectively. The additive nature of nuclear spin means that pairs of nucleons can cancel out leaving the nucleus with zero net spin, this happens when the nucleus contains an even number of protons and neutrons. If the nucleus contains an odd number of both protons and neutrons, it will have a positive integer nuclear spin whereas if the nucleus has an odd number of protons or neutrons, it will have a half integer spin.

The spin angular momentum, \mathbf{J} of a nucleus of spin I is given by

$$|\mathbf{J}| = \hbar\sqrt{I(I+1)} \quad (2.1)$$

where \hbar is the reduced Plank's constant, $h/2\pi$. As the nucleus is charged and rotating, it gives rise to a current and therefore a magnetic moment μ ,

$$\mu = \gamma \mathbf{J} \quad (2.2)$$

where γ is the gyromagnetic ratio for the nucleus, a constant which depends on the charge and mass of the nucleus. Table 2.1 shows the gyromagnetic ratio (γ) and nuclear spin (I) of common NMR sensitive isotopes [1–3]. Due to its high gyromagnetic ratio, compared to other nuclei used for NMR, and relative abundance in the body, ^1H , a single proton, is most commonly used for Magnetic Resonance Imaging (MRI).

2.1. Source of the NMR Signal

Isotope	Spin	γ (MHzT $^{-1}$)	Sensitivity Relative to ^1H
^1H	$1/2$	42.58	1
^2H	1	6.54	0.0097
^{13}C	$1/2$	10.71	0.016
^{19}F	$1/2$	40.05	0.83
^{23}Na	$3/2$	11.27	0.093
^{31}P	$1/2$	17.25	0.066

Table 2.1: Common NMR isotopes, their nuclear spin, gyromagnetic ratio and sensitivity, relative to ^1H .

2.1.2 Application of an External Magnetic Field

If we consider the hydrogen nuclei in a sample of tissue, the number of possible eigenstates for a nucleus of nuclear spin I is $(2I + 1)$. This means that for the ^1H nuclei in our sample, where $I = 1/2$, we can observe two possible eigenstates, $|+1/2\rangle$ and $|{-1/2}\rangle$ often written as $|\uparrow\rangle$ and $|\downarrow\rangle$. In the absence of an external magnetic field, these states are degenerate as they have the same energy, however, if we move our sample into a static external magnetic field along the z -axis, B_0 , the energy levels separate.

The z -component of the magnetic moment is defined by,

$$\mu_z = \gamma \hbar m_I \quad (2.3)$$

where m_I are the possible spin quantum numbers of the nucleus. For our proton system with spin $1/2$, μ_z is given by

$$\mu_z = \pm \frac{1}{2} \gamma \hbar. \quad (2.4)$$

The spins can either be aligned parallel to the external magnetic field in the lower energy of the two eigenstates, also known as spin up; or anti-parallel to the magnetic field in the higher energy eigenstate, spin down. The energy difference between these two eigenstates is given by,

$$\Delta E = \gamma \hbar B_0. \quad (2.5)$$

For an ensemble of spins in an external magnetic field, there will be an imbalance between the populations of each state with more spins occupying the lower of the two energy states. The net magnetisation of the sample is simply the sum of the constituent

2.1. Source of the NMR Signal

spins and as such, the application of an external magnetic field leads to the sample gaining a net magnetisation vector aligned with B_0 . This effect is very small, the magnitude of the imbalance between eigenstates can be derived from Boltzmann statistics and is given by,

$$\frac{N_\uparrow}{N_\downarrow} = \exp\left(\frac{\Delta E}{k_B T}\right), \quad (2.6)$$

where N_\downarrow and N_\uparrow are the the number of spins aligned with and against B_0 respectively, k_B is Boltzmann's constant and T is the temperature of the system. This means that for a sample of biological tissue at body temperature in a 3T magnetic field, the population difference is very small at approximately three parts per million. Although this measurable proportion is very small, it can be detected due to the high density of protons in the tissue. The signal can also be increased by the application of a stronger B_0 .

2.1.3 Precession

Classically, if a magnetic moment, \mathbf{M} , is placed into an external magnetic field, \mathbf{B} , it will experience a torque, τ , proportional to change in angular momentum and thus induce a rotation.

$$\mathbf{M} \times \mathbf{B} = \frac{d\mathbf{J}}{dt} = \tau \quad (2.7)$$

From (2.2) the quantum equivalent of (2.7) is the standard form of the Bloch equation [4],

$$\frac{d\mu}{dt} = \gamma \mu \times \mathbf{B} \quad (2.8)$$

This equation states that if the magnetic moment, μ is not aligned with the external magnetic field, \mathbf{B} , it will precess about \mathbf{B} . The frequency of this precession, ω_0 is known as the Larmor frequency and is given by substituting Bohr's frequency condition of the Planck relation ($\Delta E = \hbar\omega$) into (2.5),

$$\omega_0 = \gamma B_0, \quad (2.9)$$

Nuclei with a positive gyromagnetic ratio precess clockwise, whereas nuclei (and the electron) with a negative gyromagnetic ratio precess anti-clockwise. For a proton in a 3T magnetic field, the Larmor frequency is 128 MHz.

2.1.4 Resonance

Resonance is the process of energy transfer into a system by the application of energy at the natural frequency of the system. In the case of NMR this is the application of an Radio Frequency (RF) pulse, also known as B_1 field, near the Larmor frequency. Before the RF pulse is applied, the spins are at equilibrium, aligned with B_0 . Upon the application of a B_1 field close to the Larmor frequency of the target nucleus and perpendicular to B_0 , the spins aligned with B_0 will be displaced from equilibrium and thus precession is induced. The longer the B_1 field is applied, the more the net magnetisation vector is displaced, or tipped, away from B_0 , this allows arbitrary flip angles, α , to be achieved, (2.10).

$$\alpha = \int_0^T \gamma B_1(t) dt \quad (2.10)$$

In addition to displacing the spins, the B_1 field also induces phase coherence within the ensemble making up the net magnetisation vector. When considering the effects of RF pulses, it can often be simpler to imagine the system from a reference frame rotating about the z -axis at the Larmor frequency. This has the effect of making B_1 stationary along the x -axis. Figure 2.1 shows the evolution of a spin in both the laboratory and rotating frame after the application of a 90° RF pulse. In both figures the spin is tipped into the transverse plane, M_{xy} .

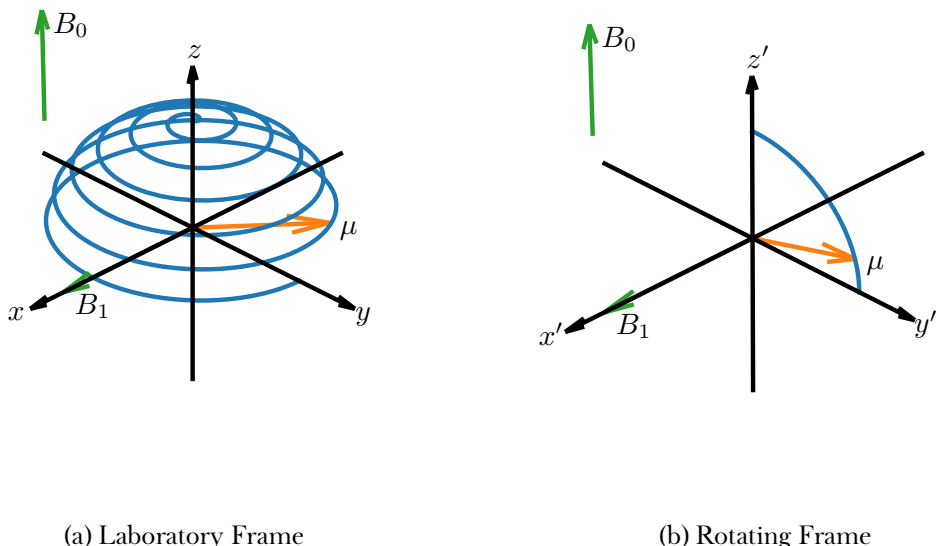


Figure 2.1: The laboratory frame of reference shows the procession of the spin about B_0 while in the rotating frame, the spin simply rotates about the x' -axis

2.2 Relaxation and Contrast Mechanisms

If disturbed from equilibrium by an RF pulse, the net magnetisation vector will not remain in this new state ad infinitum, instead, once the RF pulse has finished, it will transition back to its equilibrium state in a process known as relaxation. The time constants characterising the relaxation process vary depending on the environment the spins are in and as such, can vary between different biological tissues. These relaxation constants are the principle source of contrast in MRI. Mathematically, this relaxation is described by the full form of the Bloch equation, (2.11).

$$\frac{d\mathbf{M}}{dt} = \gamma (\mathbf{M} \times \mathbf{B}) - \frac{(M_z - M_0)}{T_1} \hat{\mathbf{z}} - \frac{M_x \hat{\mathbf{x}} + M_y \hat{\mathbf{y}}}{T_2} \quad (2.11)$$

2.2.1 Longitudinal Relaxation (T_1)

Upon excitation, energy is exchanged between the spin system and the surrounding environment. The result of this energy exchange is that the energy of the spin system decreases and the longitudinal magnetisation exponentially decays to its equilibrium position. The time constant of this exponential decay returning to equilibrium, M_0 , is known as the longitudinal relaxation time or T_1 and is dictated by the efficiency of energy transfer between the spin system and the surrounding lattice, hence its historical name, spin-lattice relaxation.

The efficiency of this energy transfer is primarily dictated by the motion of the surrounding lattice. As nearby molecules undergo rotation they cause variations in the local magnetic field. If these fluctuations are at a similar frequency to the Larmor frequency then energy transfer via dipole-dipole interactions will be relatively efficient. The rate of energy transfer can also be increased if the molecules are more closely coupled for example, tissues with a lower molecular mobility tend to have a shorter T_1 than those with a high molecular mobility.

Measuring T_1

The longitudinal component of the Bloch equation, (2.11), is given by (2.12).

$$\frac{d\mathbf{M}_z}{dt} = -\frac{(M_z - M_0)}{T_1} \quad (2.12)$$

Solving this equation for M_z gives,

$$M_z = M_0 \left[1 - \exp \left(-\frac{t}{T_1} \right) \right] + M_z(0) \exp \left(-\frac{t}{T_1} \right) \quad (2.13)$$

The gold standard method for quantification of T_1 is the inversion recovery pulse sequence in which a 180° pulse is used to fully invert the magnetisation, such that $M_z(0) = -M_0$ and as such (2.13) reduces to,

$$M_z = M_0 \left[1 - 2 \exp \left(-\frac{t}{T_1} \right) \right]. \quad (2.14)$$

To measure T_1 , the experiment is repeated multiple times, with measurements of M_z taken at different times after the 180° inversion pulse, Inversion Time (TI). The magnetisation must have fully recovered to M_0 between each inversion pulse, as such the minimum time between inversions, Repetition Time (TR) is five times T_1 . Curve fitting can then be used to estimate M_0 and T_1 , Figure 2.2. This method is expanded upon when it is used in Chapter 6.

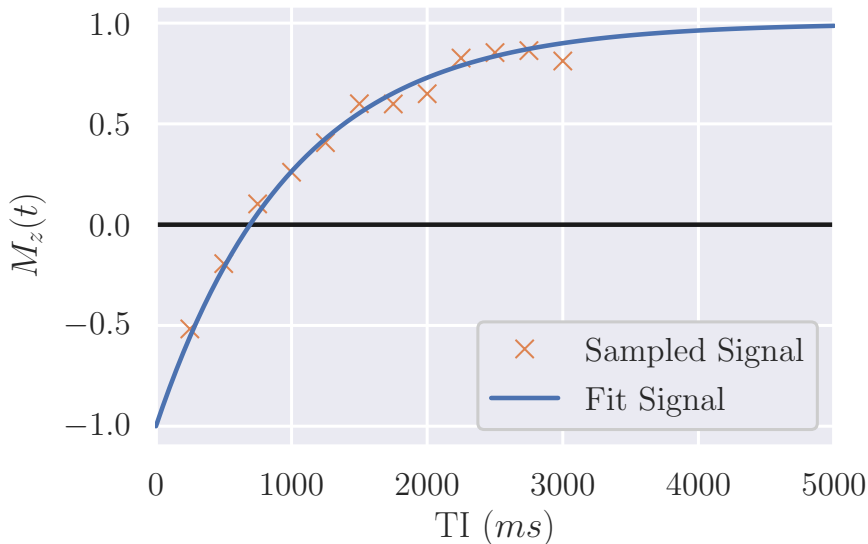


Figure 2.2: The longitudinal magnetisation for a sample of $T_1 = 1000$ ms in an inversion recovery experiment. The experiment was repeated with inversion times from 250 ms to 3000 ms in 250 ms steps.

2.2.2 Transverse Relaxation (T_2 and T_2^*)

Upon the application of a 90° RF pulse, the net magnetisation vector has tipped in the y' direction resulting in phase coherence and creating transverse magnetisation, $M_{x'y'}$. The spins then precess about the z -axis at their Larmor frequency, dictated by the magnetic field they are in. This magnetic field is not perfectly homogenous over the whole ensemble though, random dipole-dipole interaction with neighbouring spins produce short-lived fluctuations in the local magnetic field and thus the Larmor frequency of each spin varies. As the spins process at different frequencies, they de-phase, resulting in the transverse magnetisation decaying to zero as phase coherence is lost. This mechanism is driven by energy transfer between the spins within the system so is sometimes termed, spin-spin relaxation. The rate at which this loss of phase coherence due to spin-spin interactions occurs is characterised by the time constant T_2 .

The local magnetic field is not just influenced by spin-spin interactions. Local inhomogeneities in the static B_0 field can be caused by susceptibility differences within the sample and hardware imperfections. These B_0 inhomogeneities result in additional perturbation to the local magnetic field and therefore results in additional de-phasing of the system. The rate at which this de-phasing due to static B_0 inhomogeneities occurs is characterised by the time constant T'_2 . The measured decay in transverse magnetisation is therefore dictated by T_2^* , which is related to T_2 and T'_2 by

$$\frac{1}{T_2^*} = \frac{1}{T_2} + \frac{1}{T'_2}. \quad (2.15)$$

Measuring T_2 and T_2^*

The transverse component of the Bloch equation, (2.11), is given by (2.16).

$$\frac{dM_{xy}}{dt} = -\frac{M_{xy}}{T_2} \quad (2.16)$$

Solving the differential equation for M_{xy} with respect to t gives,

$$M_{xy}(t) = M_{xy}(0) \exp\left(-\frac{t}{T_2}\right), \quad (2.17)$$

It should be noted that (2.17) is an idealised equation and thus does not include static field inhomogeneities that contribute to T_2' and thus the magnetisation of a real signal will decay with T_2^* .

After a 90° RF pulse the envelope of the signal will decay with T_2^* , known as an Free Induction Decay (FID). As such, by measuring the amplitude of the signal at different time points, t , the decay can be sampled and fit to estimate T_2^* .

Spin Echoes

To measure T_2 , rather than T_2^* , the effects of static B_0 inhomogeneities that lead to T_2' must be negated. Because the processes driving the de-phasing that lead to T_2' are constant over time, the refocussing effects of a Spin Echo (SE) sequence, outlined in Figure 2.3, can be utilised to reform this de-phasing component. In a SE sequence, an initial 90° excitation pulse shifts M into the transverse plane and induces phase coherence, Figure 2.4a. T_2^* effects will then cause some spins to precess quickly and others more slowly and thus de-phase with T_2^* , Figure 2.4b. At time, Echo Time (TE)/2, later a 180° pulse is used to flip the spin ensemble, reversing the phase shift meaning those spins that had accrued the largest positive phase shift will now have the largest negative phase shift and vice versa, Figure 2.4c. Because the B_0 inhomogeneities that lead to T_2' are static, they will still be acting to the same degree on each spin. This leads to an echo forming at $t = \text{TE}$ as those spins with the highest Larmor frequency, and largest negative phase shift, refocus or “catch up” with those spins with a lower Larmor frequency, Figure 2.4d. The processes leading to T_2 are not constant over time and as such are not refocussed by the 180° pulse, hence the echo in Figure 2.4d is not perfectly refocussed and the signal will be attenuated at a rate dictated by T_2 .

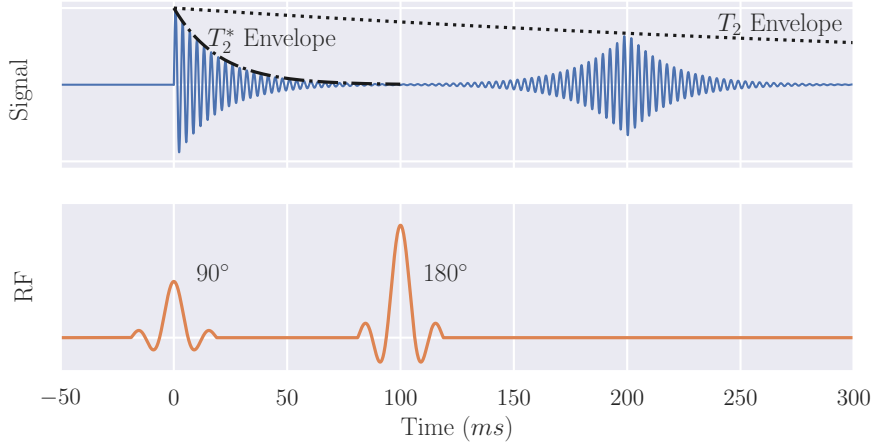


Figure 2.3: The signal produced in a spin-echo sequence used to measure T_2 . This sequence has a TE of 200 ms.

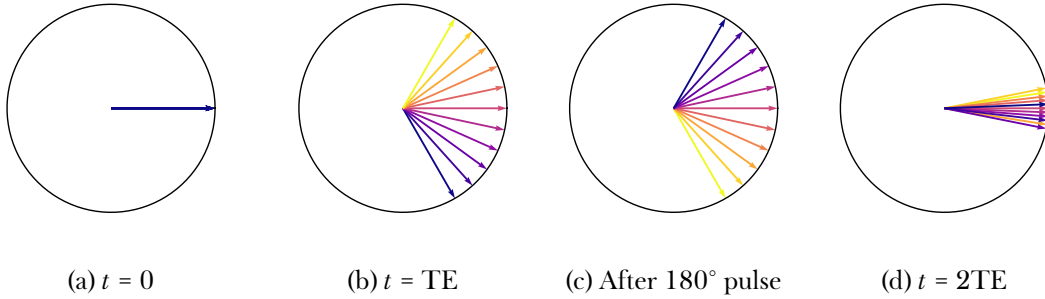


Figure 2.4: Spins evolving in a spin echo sequence showing the de-phasing, (b), refocusing pulse, (c), and subsequent refocusing, (d).

By repeating this sequence over a range of TE the T_2 curve can be samples and fit to (2.17) to estimate T_2 and M_{xy0} . The SE sequence is the most basic form of T_2 mapping, more methods are explored and compared in Chapter 3.

Gradient Echoes

Echoes can be generated via another mechanism, the Gradient Echo (GE). In addition to the homogenous B_0 field and RF fields encountered thus far, MRI scanners can produce additional fields known as gradients. These switchable fields can induce linearly varying spatially dependent magnetic fields to perturb B_0 . They are used for image formation, explained in Section 2.3 but can also be used to form an echo. The GE pulse sequence uses a single 90° RF excitation pulse to tip the net magnetisation vector into the transverse plane.

2.2. Relaxation and Contrast Mechanisms

A gradient is then applied to the sample causing areas of higher field to de-phase quickly whereas areas with a relatively lower field will de-phase slower. At time $TE/2$ the polarity of the gradient is reversed thus causing the spins to refocus and an echo to be formed at time TE . An overview of the sequence is shown in Figure 2.5.

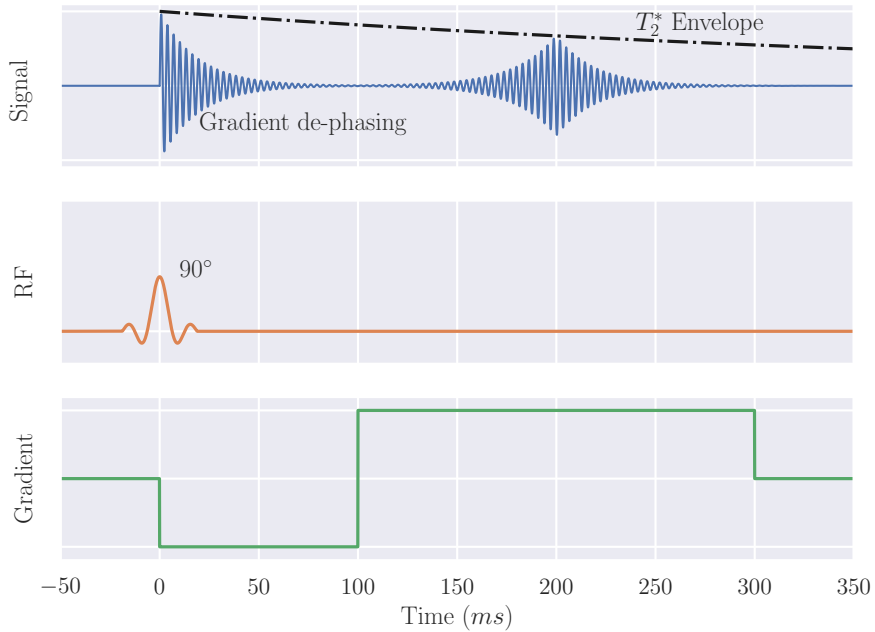


Figure 2.5: A schematic of a basic Gradient Echo (GE) sequence with $TE = 200 \text{ ms}$.

In reality, the gradients cannot switch polarity instantaneously due to the inductance of the gradient coils and characteristics of the amplifiers used to generate the gradients. This phenomenon leads to the gradient waveform being trapezoidal, however, to aid clarity in schematics within this chapter, an idealised gradient waveform has been shown. This characteristic of gradients is known as slew rate and is defined as the peak gradient amplitude upon the rise time, Figure 2.6, and for modern MRI scanners is of the order of 200 T/m/s .

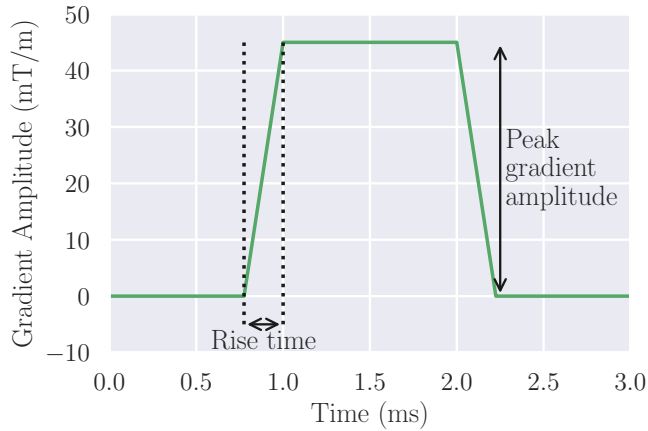


Figure 2.6: A gradient waveform with typical peak gradient amplitude, rise time and slew rate.

2.2.3 Dipole-Dipole Interactions

As outlined in 2.2.1 and 2.2.2, dipole-dipole interactions are a primary contributing factor to T_1 and T_2 times. The factors that dictate the strength of these interactions are the types of spin involved, the distance between them, the angle between them and their motion.

The strength of the interaction depends on the gyromagnetic ratio of the spins involved. The magnitude of an electrons gyromagnetic ratio is much greater than that of a proton ($-28025 \text{ MHz T}^{-1}$ and 43 MHz T^{-1} respectively [5]) and as such proton-electron interactions are much stronger than proton-proton interactions.

The strength of the interaction is inversely proportional to the sixth power of distance (seen in Equations (2.19) and (2.20)) and thus means that dipole-dipole interactions are only effective over a very short range. As such, the majority of interactions are intramolecular rather than intermolecular.

The z component of a magnetic field produced by a dipole, μ is given by Equation 2.18,

$$B_{\mu z} \propto \frac{\mu}{r^3} (3 \cos^2 \theta - 1) \quad (2.18)$$

producing the field shown in Figure 2.7. Here it can be seen that at certain angles, the magnetic field is zero, this occurs when $(3 \cos^2 \theta - 1) = 0$ and equates to angles at approx-

imately 54.7° . These angles are known as magic angles. If the dipoles are orientated at approximately the magic angle to the B_0 field, their T_2 will be increased.

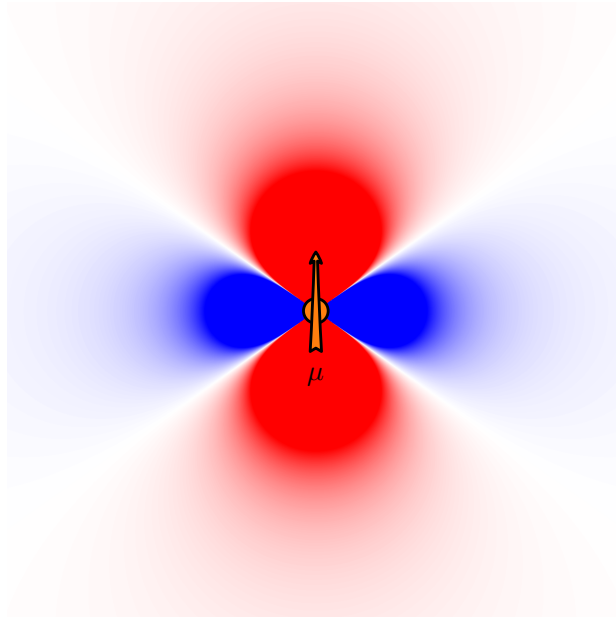


Figure 2.7: The z component of the magnetic field produced by dipole, μ .

Molecules can move in three different ways, translation, vibration and rotation. Translation has little effect on NMR signals as it is usually omnidirectional. Vibrational oscillations are at a much higher frequency than NMR phenomenon and as such do not affect the MRI signal. Rotations can be at similar frequencies to MRI and as such, influence T_1 and T_2 due to dipole-dipole interactions.

Each molecule in a sample will have a characteristic correlation time, τ_c , the time it takes the molecule to rotate by one radian. The correlation time is effected by how tightly bound the molecules are and their mass, light freely bound molecules like water in liquid form will have a short correlation time while heavy tightly bound molecules such as those found in bone, will have a longer correlation time. If a molecule is tumbling at a rate similar to the Larmor frequency, it will cause energy transfer to be more efficient, thus reducing T_1 . As the tumbling rate slows, the properties of the dipole become more similar to those of a static field, this means that nearby dipoles will experience magnetic fields perpetuated about B_0 and as such T_2 will decrease.

The mathematical framework of this phenomenon is given by the Solomon-Bloembergen equations [6] (Equations (2.19) and (2.20)). These equations predict T_1 and T_2 dependence

on correlation time, Figure 2.8, where it can be observed that T_1 is lowest when the frequency of the molecular tumbling is similar to the Larmor frequency (labelled as τ_0 where $\tau_0 = 1/\omega_0$) and that T_2 decreases as correlation time increases. Tissues with a range of tumbling rates are highlighted in Figure 2.8; the molecules in Cerebrospinal Fluid (CSF) are weakly bound as they are in the liquid phase whereas solid tissues such as bone are tightly bound.

$$\frac{1}{T_1} = \frac{6}{20} \frac{\hbar^2 \gamma^4}{r^6} \left[\frac{\tau_c}{1 + \omega^2 \tau_c^2} + \frac{4\tau_c}{1 + 4\omega^2 \tau_c^2} \right] \quad (2.19)$$

$$\frac{1}{T_2} = \frac{3}{20} \frac{\hbar^2 \gamma^4}{r^6} \left[3\tau_c + \frac{5\tau_c}{1 + \omega^2 \tau_c^2} + \frac{2\tau_c}{1 + 4\omega^2 \tau_c^2} \right] \quad (2.20)$$

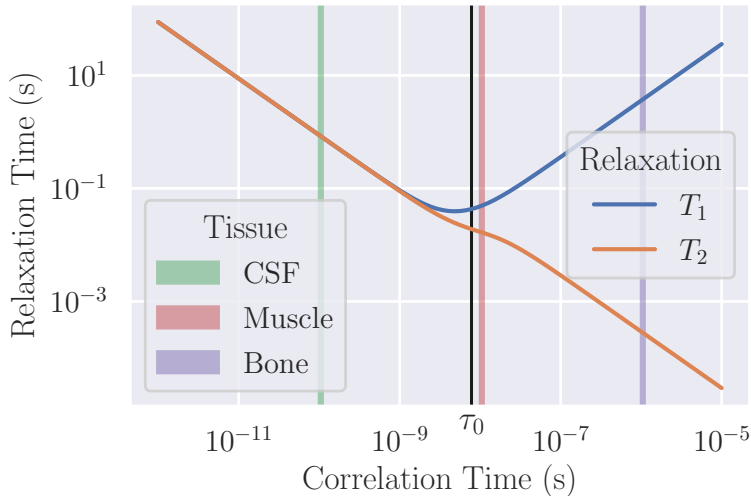


Figure 2.8: T_1 and T_2 dependence on molecular correlation time as predicted by the Solomon-Bloembergen equations. Tissues with a range of correlation times are highlighted.

2.2.4 Diffusion Imaging

Spins have been considered stationary until now, however, in biological tissues, they are often undergoing Brownian motion leading to diffusion. The signal from a sample can be made sensitive to the degree of diffusion taking place using diffusion gradients applied between excitation and echo. If a spin undergoes a translation while the gradient is being applied, it will be in a different magnetic field and thus at a different Larmor frequency

2.2. Relaxation and Contrast Mechanisms

while rephasing, resulting in additional signal attenuation. The degree of signal attenuation is proportional to the rate at which diffusion is occurring i.e. how far the spin has moved while the diffusion gradient was being applied. These diffusion gradients can either be bipolar, as seen in Figure 2.5 or monopolar if a SE sequence is used.

Not all diffusion is isotropic (occurs to the same degree in all directions), often the motion of the spins is restricted e.g. within tissue fibres. The amount of restriction is known as the fractional anisotropy where 0 represents isotropic diffusion e.g. a large vial of water, and 1 represents diffusion being constrained to a single dimension. By applying the diffusion gradients in different directions (and strengths) the preferred direction of diffusion and fractional anisotropy can be calculated. These techniques are used in Chapter 6.

2.2.5 Optimisation of Tissue Contrast

Quantitative mapping of T_1 , T_2 and T_2^* can often be a slow process due to the number of acquisitions required at different time points to sample relaxation curves. Often it is more desirable to acquire a volume at a single time with the intensity difference between tissues of interest maximised. Although the voxel intensities do not directly represent any quantitative underlying physical properties of the tissue, the contrast between tissues is sufficient for diagnosis or further analysis.

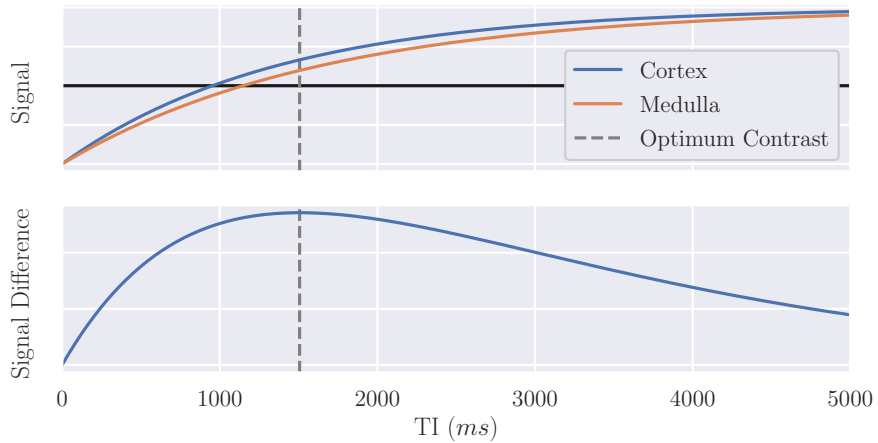


Figure 2.9: The signal generated from renal cortical and medullary tissues [7] and difference between signals. This shows that the contrast between the two tissues is optimal if the Inversion Time (TI) is 1500 ms.

2.3 Forming an Image

2.3.1 Signal Localisation

So far, NMR has been applied to measure signals from the entire sample, gaining no information about the spatial variation within it. MRI applies the techniques of NMR to spatially resolve the location of the signal.

The key concepts of MRI were developed by multiple groups in the 1970s. Lauterbur used magnetic field gradients and a back-projection reconstruction technique to generate 2D images in 1973 [8]. Simultaneously Mansfield was working on “NMR diffraction” introducing the mathematical framework of reciprocal k -space [9] and later slice selective excitation [10]. The final key insight was provided by Ernst who published the first Fourier imaging method [11], this used non-selective excitations and linear gradients to generate 2D Fourier encoded images. These techniques are still the basis of MRI today.

The concepts of signal localisation will be introduced through the example of an axial acquisition, Figure 2.10

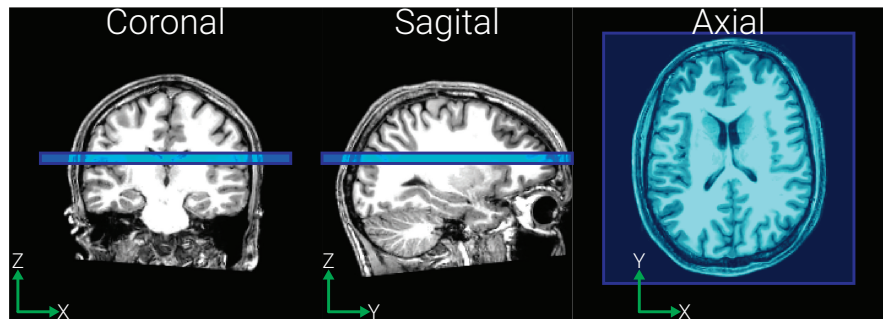


Figure 2.10: Planning used in the signal localisation example.

Gradient Fields

Signal localisation makes use of gradient fields. These produce small linear perturbations in B_0 and are applied in a combination of the x , y and z direction to enable arbitrary gradient directions and result in B_0 varying with position, \mathbf{r} ,

$$B_z(r) = (B_0 + \mathbf{G} \cdot \mathbf{r}) \hat{k}. \quad (2.21)$$

2.3. Forming an Image

As such, the resonant frequency of the spins can also be described as a function of position and, because the gradients are not static, time,

$$\omega(x, y, z, t) = \gamma(B_0 + G_x(t)x + G_y(t)y + G_z(t)z) \quad (2.22)$$

Slice Selection

The initial step in localisation is to measure the signal from a single, spatially defined, slice. If a gradient is applied along the z direction, G_z , the magnetic field experienced by the spins at position z will be

$$B(z) = B_0 + G_z z. \quad (2.23)$$

As such, from the simplification of (2.22), the Larmor frequency becomes

$$\omega(z) = \gamma(B_0 + G_z z). \quad (2.24)$$

If a frequency selective RF pulse is applied to the sample, it will only excite spins within the corresponding bandwidth and thus only a slice of desired thickness. This slice-selective thickness, Δz , can be changed by either adjusting G_z or the bandwidth of the excitation pulse, $\Delta\omega$.

$$\Delta z = \frac{\Delta\omega}{\gamma G_z} \quad (2.25)$$

The excitation profile achieved by a slice selective pulse can be approximated by a Fourier transform. Generally, a rectangular slice profile is wanted and as such, the RF pulse takes the form of a sinc function. To achieve a perfect rectangular pulse, the sinc would have to be infinite in length. Given the lack of infinite time available during an MRI examination, a truncated sinc pulse is used, generally including three or five lobes and a Gaussian filter.

The gradient applied will result in de-phasing of the spins as in a GE sequence, therefore a gradient of the opposite polarity and half the magnitude is applied after the RF pulse to re-phase the spins, Figure 2.11a.

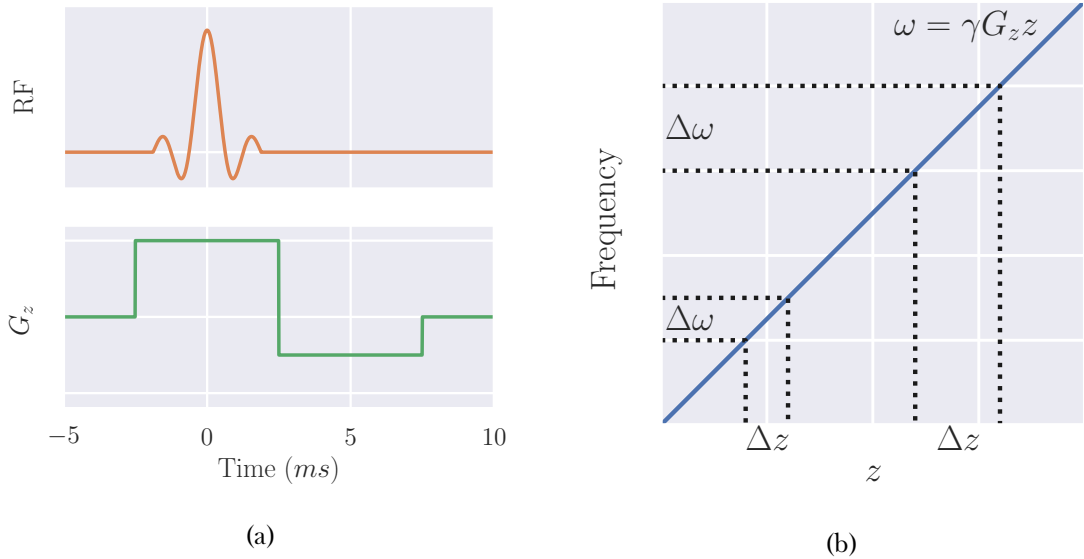


Figure 2.11: (a) A truncated sinc pulse of bandwidth $\Delta\omega$ being applied over a slice selective gradient followed by the negative re-phasing gradient lobe. Note that the area under the re-phasing gradient is half of that of the slice selective gradient. (b) Example slices of thickness Δz being excited by RF pulses of bandwidth $\Delta\omega$ showing that excitation pulses of larger bandwidth result in thicker slice profiles.

Phase Encoding

The signal has been localised from a full 3D volume to a defined 2D volumetric slice. To localise the signal in the next dimension, phase encoding is used. This technique uses a gradient in the y direction applied for time T . For the duration of G_y the spins precess with a frequency according to their position in the y direction

$$\omega(y) = \gamma(B_0 + G_y y), \quad (2.26)$$

and as such accrue a phase shift relative to if no gradient was applied, given by

$$\phi(y) = \gamma y \int_0^T G_y(t) dt. \quad (2.27)$$

Acquisitions must be repeated with different amplitudes/durations of G_y to fully sample in the y direction, Figure 2.13.

Phase aliasing occurs because the whole sample produces signal, whether it is in the Field

2.3. Forming an Image

Of View (FOV) or not. As there is a finite range of phase values (0 to 2π) tissue outside the FOV can have the same value as tissue within the FOV this results in the two signals becoming indistinguishable and therefore combined in a process known as wrapping. This artefact is illustrated in Figure 2.12.

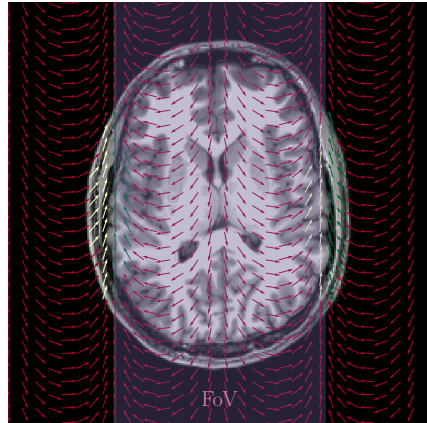


Figure 2.12: Spins outside the FOV have the same phase value as those within the FOV and thus wrapping occurs.

Frequency Encoding

Finally, the signal needs to be localised in the x direction. This is achieved using frequency encoding. Here the gradient, G_x is applied during the acquisition section of the sequence i.e. when the signal is being sampled. As the gradient is being applied during readout, those spins in the centre of the gradient (at field B_0) will be precessing at the Larmor frequency while those in a stronger or weaker field will be precessing faster or slower respectively. By sampling the signal generated and applying a Fourier transform to separate components of the signal at each frequency, the signal is spatially resolved in all three dimensions. An overview of a basic signal localisation scheme is shown in Figure 2.13.

2.3. Forming an Image

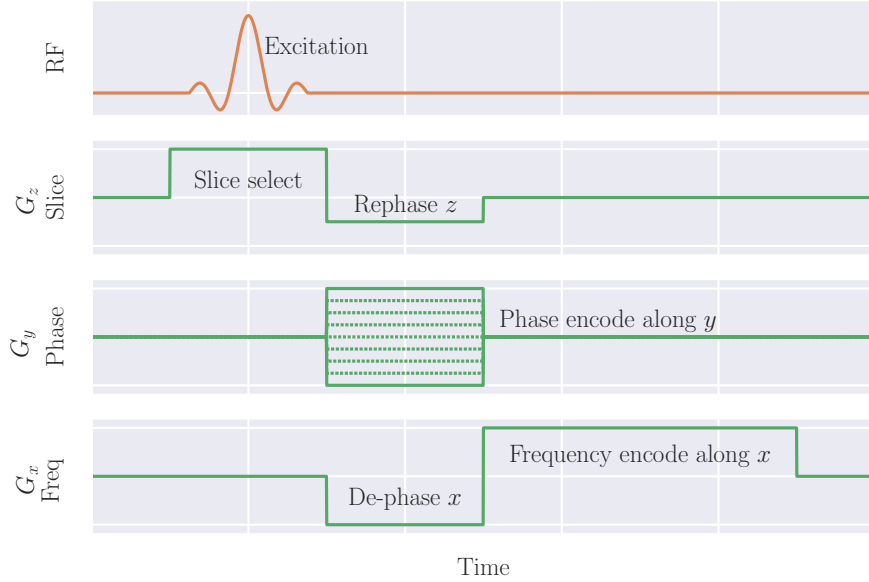


Figure 2.13: A basic spacial localisation pulse sequence showing how gradients applied along the z , y and x directions can be used to localise the signal in the corresponding dimensions.

k -space

k -space, sometimes known as Fourier space, is a useful concept for interpreting MRI pulse sequences and represents the spatial frequencies of the image. Immediately after an excitation pulse and rewind gradient, the signal being sampled is at the origin of k -space, corresponding to low spatial frequencies, or the low resolution aspects of the image e.g. which voxels are inside or outside the body. As gradients are applied to the sample, sampling moves out from the centre of k -space to higher spatial frequencies corresponding to finer detail within the image. For a 2D acquisition, as above, the location in k -space is defined by (2.28) and (2.29) where G_x and G_y are the gradients in the frequency encode and phase encode directions respectively and t_x and t_y are the duration the gradient is applied for.

$$k_x = \gamma G_x t_x \quad (2.28)$$

$$k_y = \gamma G_y t_y \quad (2.29)$$

When recording MRI data, the continuous signal must be discretised. The higher the sampling frequency i.e. the closer together in k -space the samples are, Δk , the wider the FOV and the further out from the origin of k -space is samples, the higher resolution the

2.3. Forming an Image

image will be. Examples of k -space sampling patterns and their corresponding image are shown in Figure 2.14.

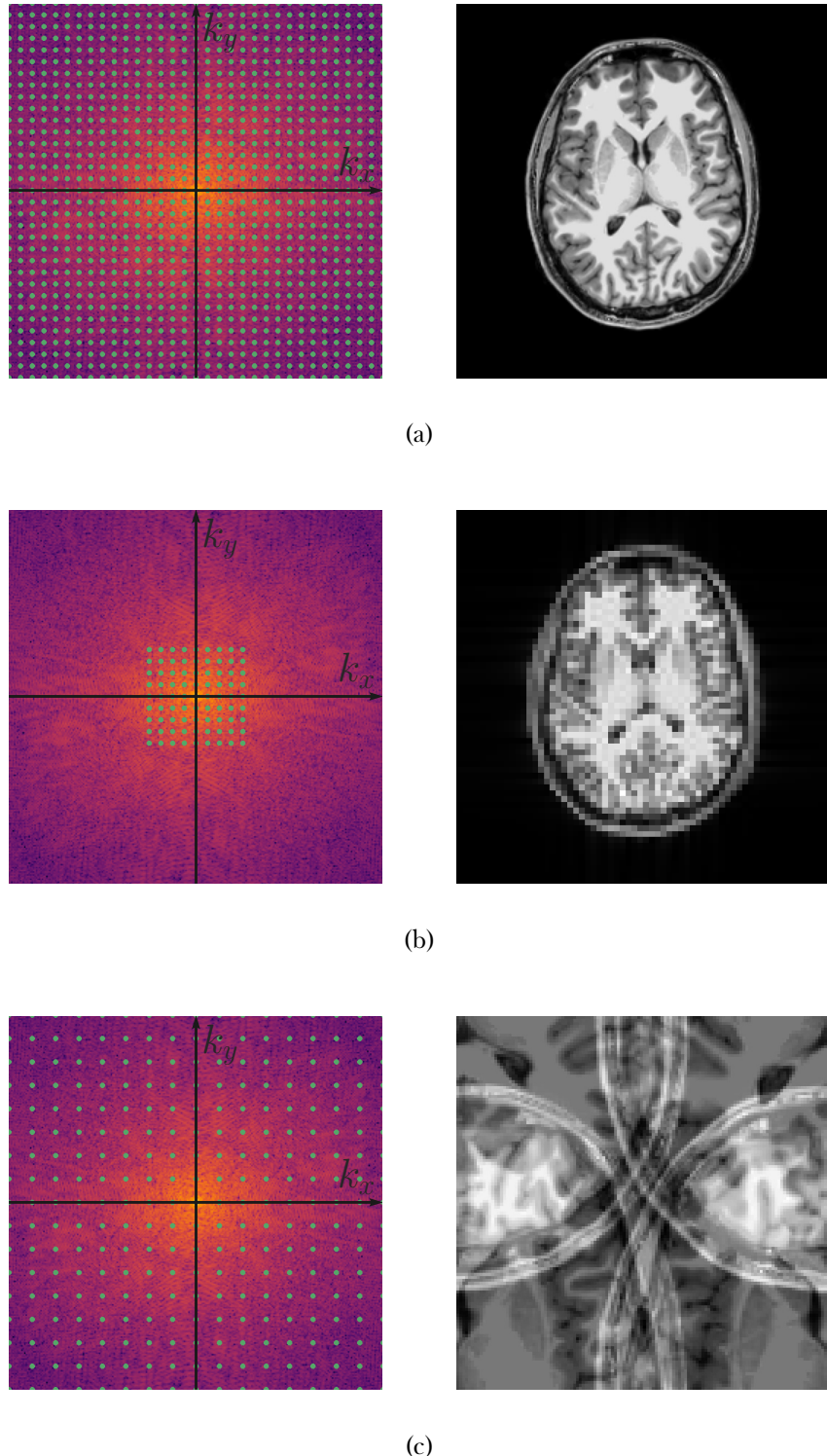


Figure 2.14: (a) Fully samples k -space and the corresponding image. (b) Centre sampling of k -space produces a lower resolution image. (c) Sampling with a larger Δk resulting in a decreased FOV and aliasing.

From k -space to Image Space

The raw data sampled in k -space can be reconstructed to an image via a Fourier transform. When the quadrature data undergoes a 2D Fourier transform, it produces a complex image composed of a real and imaginary part. These constituent parts of the image can be converted into magnitude and phase images with the magnitude representing the spin density.

Coordinate Systems

The above example was chosen so that only one gradient is used at once however if the planning of the acquisition is more complicated, the nomenclature can become more confusing, as such, for clarity multiple coordinate systems are often used.

Scanner Space This coordinate system has its origin at isocentre of the scanner and is defined in terms of x , y and z .

Imaging Space The coordinates of this system are defined by the directions used in signal localisation, M for the frequency encode direction (also called magnitude), P for the phase encode direction and S for the slice select direction.

Anatomical Space Defined in terms of the subjects orientation in the scanner, this coordinate system has the axis, Right-Left (R-L), Anterior-Posterior (A-P) and Superior-Inferior (S-I).

2.3.2 Image Acquisition Acceleration

One of the recurring limiting factors in MRI is the acquisition time. For neuroimaging applications the relatively slow acquisition of MRI limits subject throughput or the number of different measures that can be performed. In abdominal imaging, acquisition times can be even more of a hindrance given many scans are performed while the subject is holding their breath on expiration. As such, image acquisition acceleration techniques have been

2.3. Forming an Image

developed. These techniques sacrifice a small amount of Signal to Noise Ratio (SNR) for a decrease in acquisition time.

Partial Fourier

Fully sampled k -space contains inherent redundancy as it contains its own complex conjugate; the real components of the signal are symmetric while the imaginary components are anti-symmetric. This means that no contrast information is lost if a reduced area of k -space is sampled e.g. only sample 66% of k -space. This technique does impact phase information though so should not be used in acquisitions where downstream processing requires accurate phase. Known as partial Fourier or half-scan, this technique results in a decreased SNR and can introduce image artefacts as the partial Fourier factor approaches 50%, however, the acquisition time reduces by approximately the percentage of k -space sampled e.g. an acquisition that would take three minutes fully sampled will take two minutes if a partial Fourier factor of 66% is used. An example of reconstructions of 100%, 75% and 51% of k -space are shown in Figure 2.15

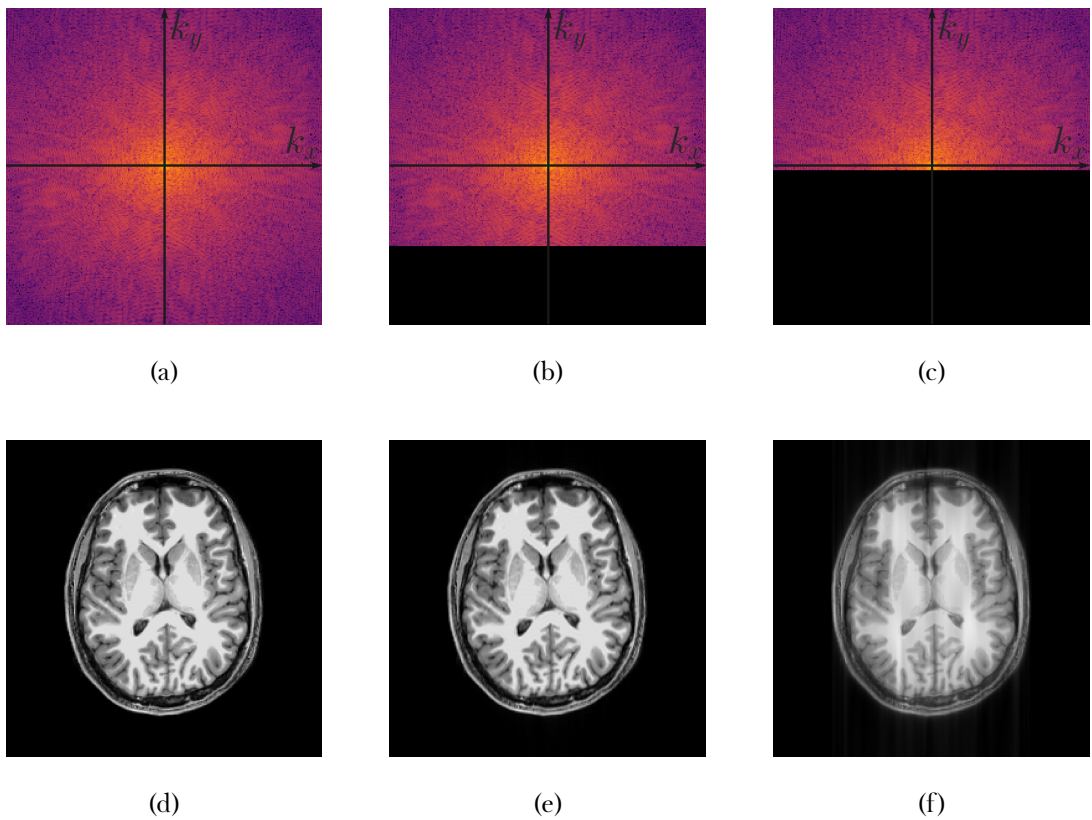


Figure 2.15: Full, (a), 75%, (b), and 51%, (c), k -space sampling and their corresponding reconstructions in image space, (d), (e) and (f) respectively.

Sensitivity Encoding (SENSE)

Most modern scanners use different coils for RF transmission, and signal receiving. The transmission coil is usually built into the bore of the magnet while the receive coil is placed as close to the source of the signal as possible. These receive coils are usually composed of multiple smaller coils to make an array, each with its own signal sampling hardware. This means that it is possible to record signal from multiple coils simultaneously with different coils supplying data for each line of k -space e.g if the array has two coils, one coil will record the odd lines of k -space and the other, the even lines, thus resulting in an increase in acquisition speed [12]. This parallel sampling technique reduces the lines of k -space sampled per coil and results in wrapping as seen in Figure 2.14c, albeit only in the phase direction. To combat this, the spatial sensitivity profile of each element within the array i.e. the area it can measure signal from, is measured. Using this prior knowledge of signal locations, each coil elements data can be unwrapped before the data from all elements is combined into a single volume.

The Sensitivity Encoding (SENSE) factor is the degree to which k -space is undersampled and is limited to the number of elements in the receive array. Applying higher SENSE factors increases acquisition speeds, however, reduces SNR.

2.3.3 Image Acquisition Schemes

Many different acquisition schemes have been developed for sampling k -space. Outlined below are some of the key sequences that form the basis of much of MRI.

Spin Warp Imaging

The simplest uniformly sampled k -space trajectory is spin warp imaging. This technique is based on the GE scheme and samples one line of k -space per excitation, or shot, a schematic is shown in Figure 2.16. Each shot applies a different phase encode gradient to move a different amount in the k_y direction. The signal is then sampled while a gradient is applied in the frequency direction, also known as the readout gradient. The acquisition time for this sequence is very long because it only collects one line of k -space per shot and as such this technique is sensitive to subject motion.

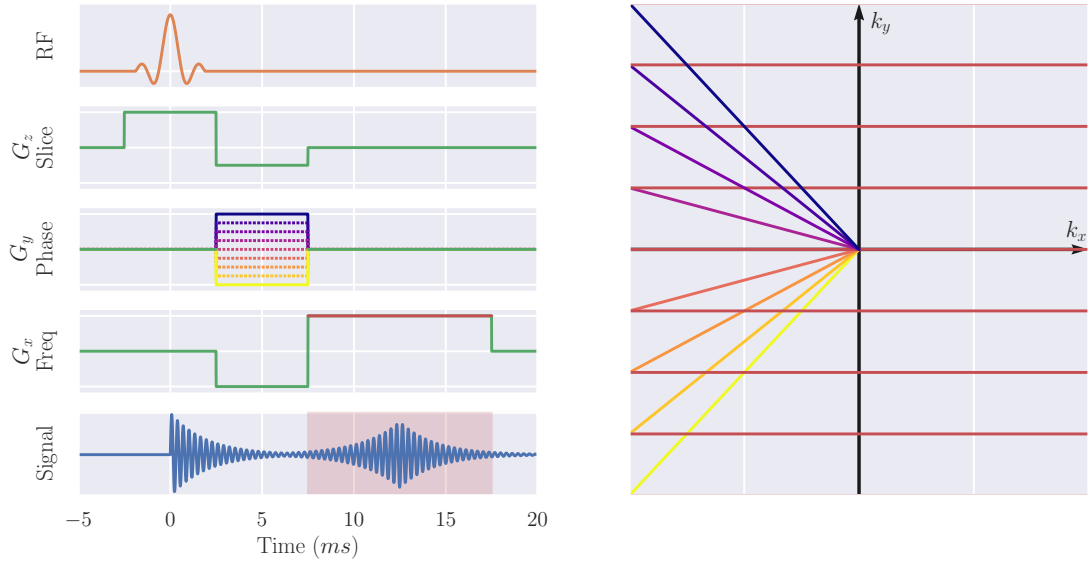


Figure 2.16: A schematic of the spin warp image sequence. The Pulse Sequence Diagram (PSD) shows the different phase encoding gradients, G_y , in colours from yellow to purple and the readout gradient, G_x , in red. These colours correlate with the colours in the k -space trajectory. The signal recorded is highlighted in red.

Echo Planar Imaging (EPI)

A much faster technique than spin warp imaging is Echo Planar Imaging (EPI) [9]. This technique samples all lines of k -space in a single excitation shot with an acquisition time typically less than 100 ms. The Pulse Sequence Diagram (PSD) and k -space trajectory for this sequence are shown in Figure 2.17. The sequence begins very similarly to the spin warp sequence with a slice selective excitation and an acquisition of the bottom line of k -space, however, instead of a spoiler followed by another excitation as in spin warp imaging, in EPI a small positive phase encode gradient ‘blip’ is applied to move up a line in k -space, followed by an inversion of the readout gradient polarity. This blip followed by reversed readout is repeated, zig-zagging up k -space until the desired k -space is sampled.

2.3. Forming an Image

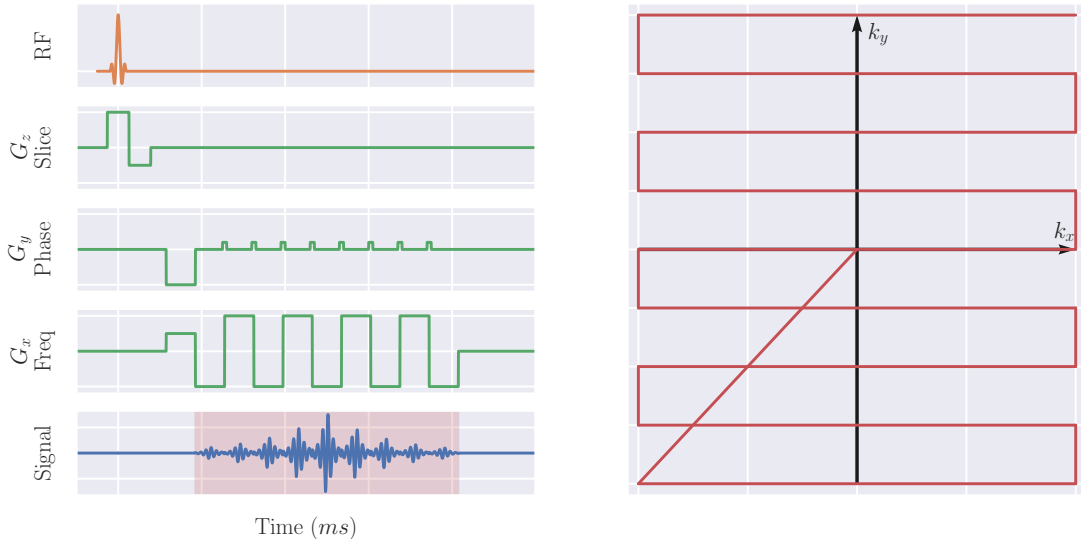


Figure 2.17: A schematic of the EPI pulse sequence and k -space trajectory. Note this diagram is not to scale.

While this sequence has a very quick acquisition time, it does have drawbacks. The long train of echoes makes EPI more sensitive to inhomogeneities in the B_0 field caused by different tissue susceptibilities or poor shimming. Eddy currents and imperfections in gradient coils cause small differences in lines collected in the positive and negative direction, leading to a Nyquist ghost artefact. Eddy currents induced by the phase encode blips also cause geometric distortions in the image, Figure 2.18, however, these can be corrected via post processing if an image with phase encode blips of opposite polarity is collected i.e. collect images sampling k -space from both bottom to top and top to bottom.

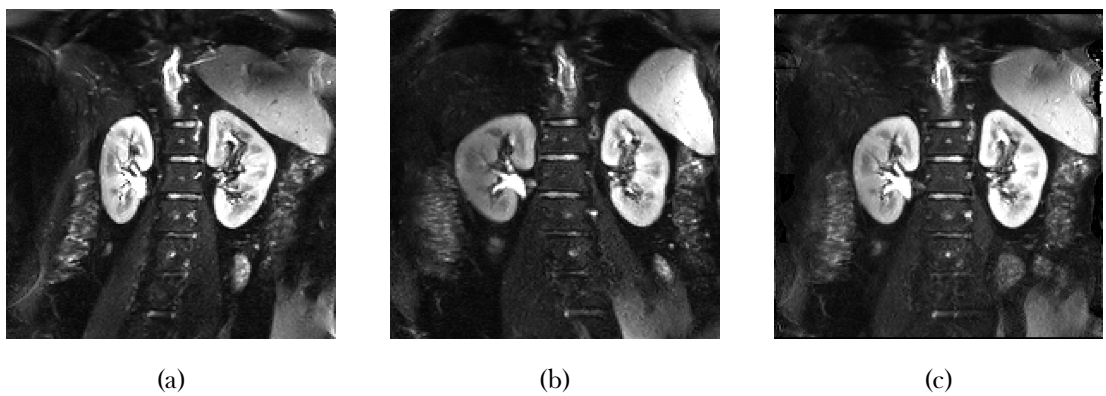


Figure 2.18: Geometric distortions in EPI when phase encode blips are (a) positive, (b) negative and (c) corrected via post processing.

2.3. Forming an Image

Turbo Spin Echo (TSE)

The Turbo Spin Echo (TSE) sequence, also known as Fast Spin Echo (FSE) or Rapid Acquisition with Relaxation Enhancement (RARE), is an expansion on the conventional SE sequence applying evenly spaced 180° RF refocusing pulses to generate multiple echo from a single excitation, these echoes are used to record multiple lines of k -space. The number of echoes is known as the Echo Train Length (ETL), or ‘turbo factor’ and is the factor by which the scan time is reduced compared to a conventional spin echo sequence and is usually between 2 and 30 per TR; the time between echoes is known as the echo spacing and is typically 15 - 25 ms.

Each line of k -space is acquired at a different time after excitation, as such, they will have different T_2 weightings, it is therefore important to ensure the centre of k -space is acquired at the desired TE as this echo will dominate the image contrast. The time between excitation and the centre of k -space is known as the Effective Echo Time (eTE).

The decrease in acquisition time comes at the expense of RF exposure, the large number of 180° pulses leads to lots of energy in the form of heat being deposited in the tissue being imaged, this is known as Specific Absorption Rate (SAR). SAR limits are imposed when scanning to avoid damaging any tissue and as such TSE with its high RF power can easily exceed these limits. Modern TSE sequences can reduce the angle of the refocusing pulse, however this can come at the expense of quantitative accuracy.

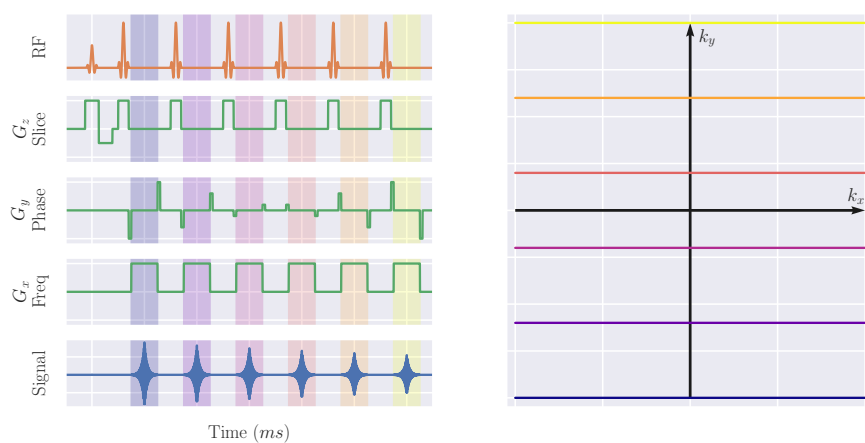


Figure 2.19: A schematic of the TSE pulse sequence and k -space trajectory. The coloured bands on the PSD correspond to the colours of the k -space trajectories. Note this diagram is not to scale.

Half-Fourier Single-shot Turbo spin Echo (HASTE)

The Half-Fourier Single-shot Turbo spin Echo (HASTE) sequence uses a combination of the techniques above. A single excitation is followed by a very long echo train with short echo spacing. This allows a large proportion of k -space to be sampled within a single TR and thus a whole slice is acquired. To minimise the number of lines of k -space acquired and thus the ETL, partial Fourier techniques are utilised. The relatively long TE required for a HASTE sequence means images are normally T_2 weighted.

The advantage of HASTE is its rapid acquisition. It can be used to minimise the effects of motion when scanning uncooperative patients, fetuses or structures the subject has no control over such as the bowel. Alternatively it can be used to capture a large FOV in a single breath hold, thus minimising the effects of inconsistent expiration level, as in Chapter 5. The very long ETL can cause significant blurring of the image, thus reducing its clinical readability.

Turbo Field Echo (TFE)

Turbo Field Echo (TFE), also known as ulatrafast GE, is designed to speed up acquisition of GE images by reducing the TR between excitations. Typical basic GE sequences have relatively long TR to allow the recovery of longitudinal magnetisation. The flip angle used in the TFE sequence is much smaller than the examples explored so far, usually approximately 10° thus leaving a large component of the magnetisation in the longitudinal direction while tipping enough magnetisation into the transverse plane to record a signal at an acceptable SNR. Between each excitation, the transverse magnetisation is spoiled to ensure the images are only T_1 weighted.

After a train of equally spaced RF pulses of Flip Angle (FA), α , and period, TR, the longitudinal magnetisation reaches a steady state, S_{TFE} , after a sufficient number of pulses. This steady state signal depends on the T_1 of the tissue and the FA and TR of the sequence. Assuming perfect transverse magnetisation spoiling between each RF pulse, this equilibrium signal is given by,

$$S_{TFE} = M_0 \frac{\sin(\alpha) [1 - \exp(-TR/T_1)]}{1 - \cos(\alpha) \exp(-TR/T_1)} \exp\left(-\frac{TE}{T_2^*}\right). \quad (2.30)$$

2.4. Conclusion

The angle that produces the maximum signal, known as the Ernst angle, α_E , is given by,

$$\alpha_E = \arccos \left[\exp \left(-\frac{TR}{T_1} \right) \right]. \quad (2.31)$$

Figure 2.20 shows the ratio of the steady state signal to the fully recovered, 90° excitation signal of renal cortex (T_1 of 1376 ms) for a range of flip angles and TR. Additionally the Ernst angle is shown.

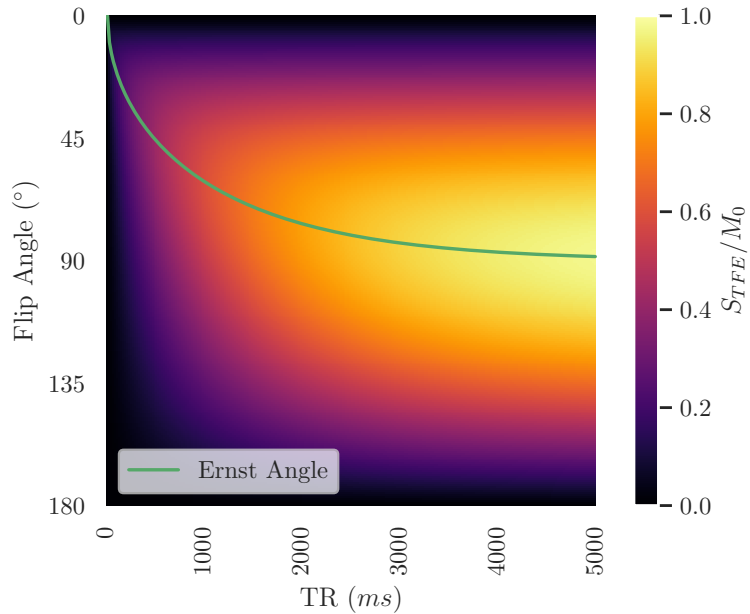


Figure 2.20: The expected steady state signal of a TFE pulse sequence and Ernst angle when imaging renal cortex.

2.4 Conclusion

This chapter has introduced the basic concepts of NMR and MRI required for interpreting this thesis. These techniques are built upon in the experimental chapters for quantification of renal properties, both in-vivo and ex-vivo.

2.5 References

1. Harris, R. K. N.m.r. and the Periodic Table. *Chemical Society Reviews* **5**, 1–22. issn: 1460-4744 (1st Jan. 1976).
2. Bernstein, M. A., King, K. F. & Zhou, X. J. *Handbook of MRI Pulse Sequences* 1041 pp. isbn: 978-0-08-053312-4. Google Books: d6PLHcyejEIC (Elsevier, 21st Sept. 2004).
3. Westbrook, C. *MRI at a Glance* 138 pp. isbn: 978-1-119-05854-5. Google Books: WeRbCwAAQBAJ (John Wiley & Sons, 18th Nov. 2015).
4. Bloch, F. Nuclear Induction. *Physical Review* **70**, 460–474 (1st Oct. 1946).
5. Mohr, P. J., Newell, D. B. & Taylor, B. N. CODATA Recommended Values of the Fundamental Physical Constants: 2014. *Reviews of Modern Physics* **88**, 035009 (26th Sept. 2016).
6. Solomon, I. Relaxation Processes in a System of Two Spins. *Physical Review* **99**, 559–565 (15th July 1955).
7. Cox, E. F. *et al.* Multiparametric Renal Magnetic Resonance Imaging: Validation, Interventions, and Alterations in Chronic Kidney Disease. *Frontiers in Physiology* **8**. issn: 1664-042X (2017).
8. Lauterbur, P. C. Image Formation by Induced Local Interactions: Examples Employing Nuclear Magnetic Resonance. *Nature* **242**, 190–191. issn: 1476-4687 (5394 Mar. 1973).
9. Mansfield, P. & Grannell, P. K. NMR "Diffraction" in Solids? *Journal of Physics C: Solid State Physics* **6**, L422–L426. issn: 0022-3719 (Nov. 1973).
10. Garboway, A. N., Grannell, P. K. & Mansfield, P. Image Formation in NMR by a Selective Irradiative Process. *Journal of Physics C: Solid State Physics* **7**, L457–L462. issn: 0022-3719 (Dec. 1974).
11. Kumar, A., Welti, D. & Ernst, R. R. NMR Fourier Zeugmatography. *Journal of Magnetic Resonance (1969)* **18**, 69–83. issn: 0022-2364 (1st Apr. 1975).
12. Pruessmann, K. P., Weiger, M., Scheidegger, M. B. & Boesiger, P. SENSE: Sensitivity Encoding for Fast MRI. *Magnetic Resonance in Medicine* **42**, 952–962. issn: 1522-2594 (1999).

Chapter 3

Assessment of Renal T_2 Mapping Methods

Abstract

This work was presented as an aural presentation at the International Society of Magnetic Resonance in Medicine (ISMRM) 28th Annual Meeting (2020) [1].

Lorem ipsum dolor sit amet, consectetuer adipiscing elit. Ut purus elit, vestibulum ut, placerat ac, adipiscing vitae, felis. Curabitur dictum gravida mauris. Nam arcu libero, nonummy eget, consectetuer id, vulputate a, magna. Donec vehicula augue eu neque. Pellentesque habitant morbi tristique senectus et netus et malesuada fames ac turpis egestas. Mauris ut leo. Cras viverra metus rhoncus sem. Nulla et lectus vestibulum urna fringilla ultrices. Phasellus eu tellus sit amet tortor gravida placerat. Integer sapien est, iaculis in, pretium quis, viverra ac, nunc. Praesent eget sem vel leo ultrices bibendum. Aenean faucibus. Morbi dolor nulla, malesuada eu, pulvinar at, mollis ac, nulla. Curabitur auctor semper nulla. Donec varius orci eget risus. Duis nibh mi, congue eu, accumsan eleifend, sagittis quis, diam. Duis eget orci sit amet orci dignissim rutrum.

3.1 Introduction

Quantitative Magnetic Resonance Imaging (MRI) is the process of taking measurements where the voxel values have numerical significance rather than simply representing signal intensity in arbitrary units [2]. These numerically significant values can take the form of macroscale properties such as rate of oxygen consumption and blood vessel flow rates or microscale properties such as tissue T_1 and susceptibility. When interpreted these values can be used improve diagnostic and treatment of patients.

The kidneys are structurally and functionally complex organs and as such lend themselves to the wide variety of MRI protocols designed to probe different aspects of the tissue and processes carried out within. While high resolution images of the kidneys morphology and basic measures such as Total Kidney Volume (TKV) can be very useful in diagnosing and monitoring disease progression [3–5], these do not fully leverage the quantitative nature of MRI. Measurements of T_1 have been shown to correlate well with fibrosis in the myocardium [6, 7], liver [8, 9] and kidneys [10] and more generally an increase in T_1 is associated with Chronic Kidney Disease (CKD) [3, 11, 12]. Arterial Spin Labelling (ASL) techniques can be used to quantify renal perfusion in physiological units (mL/100g/min) and has been shown to be correlated with allograft function post renal transplant in addition to cold ischemia time and the recipients Estimated Glomerular Filtration Rate (eGFR) [13–16]. Additionally ASL has been used to measure a decrease in perfusion in CKD subjects [11, 17, 18]. These techniques have proved useful when used individually however they can be combined and used in the same scanning session to greater effect as a multi-parametric protocol [3, 12, 19–21].

T_2 mapping has found wide use in cardiac MRI for assessment of myocardial edema [22–24] and iron overload [25, 26]. It has also effectively been used in the brain to study multiple sclerosis [27], epilepsy [28], dementia [29] and Parkinson’s disease [30]. Despite these developments elsewhere in the body, T_2 mapping has had limited uptake in the renal community.

Renal T_2 mapping has seen most research focusing on repeatability measures [31–34] with clinical uses in the field of assessment of allograft function in mice [21] and humans [35, 36], and has shown potential for early diagnosis of Autosomal Dominant Polycystic Kidney Disease (ADPKD) [37] and assessment of clear cell renal cell carcinoma [38].

3.2. Methods

In the existing literature, there is a substantial variation in quoted T_2 values for the kidneys of healthy volunteers, this is thought to be, in part, due to the differences in T_2 mapping methodologies. There are currently four main methods, a basic spin echo method, a multi echo-spin echo method, a gradient spin echo method and a Carr-Purcell-Meiboom-Gill (CPMG) T_2 prep method. Here we aim to compare each of these methods in the context of renal T_2 mapping to ascertain which is most suitable. This involves evaluating each methods quantitative accuracy, image quality, susceptibility to flow and suitability for use in-vivo.

3.1.1 Theory

3.2 Methods

3.2.1 Acquisition Schemes

There are multiple methods for acquiring T_2 maps in the kidneys, Spin Echo (SE)-Echo Planar Imaging (EPI), Multi-Echo Turbo Spin Echo (ME-TSE), Gradient Spin Echo (GraSE) and T_2 preparation. We wish to compare each of these methods in-vivo and verify their accuracy using a calibrated phantom. A QalibreMD System Standard Model 130 [39] is used for verification. All data is collected on a Philips 3T Ingenia system.

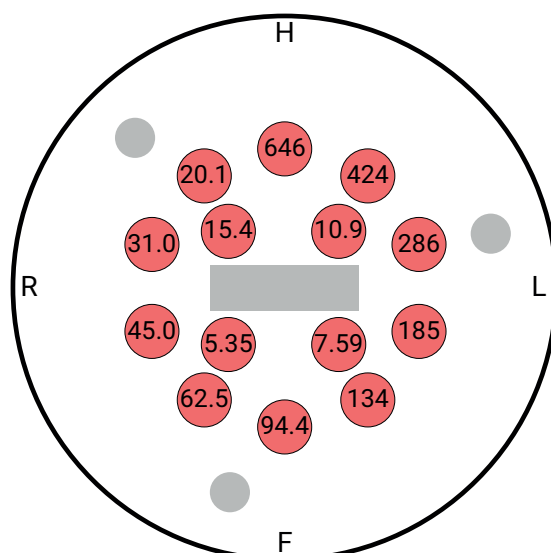


Figure 3.1: A schematic of the T_2 spheres in the QalibreMD phantom.

3.2. Methods

Spin Echo-Echo Planar Imaging

A series of volumes are collected at a range of echo times using a multi-slice spin echo acquisition with EPI readout. Acquisition parameters are Field Of View (FOV) = $288 \times 288 \times 25$ mm, voxel size = $3 \times 3 \times 5$ mm 3 , Repetition Time (TR) = 5000 ms, Flip Angle (FA) = 90°, Sensitivity Encoding (SENSE) = 2.55, halfscan = 0.844 and the sequence is respiratory triggered for in-vivo use and has an acquisition time of approximately 9 minutes depending on breathing rate. Volumes are acquired at Echo Time (TE) between 20 ms and 70 ms in 5 ms steps with four volumes being acquired at each echo time.

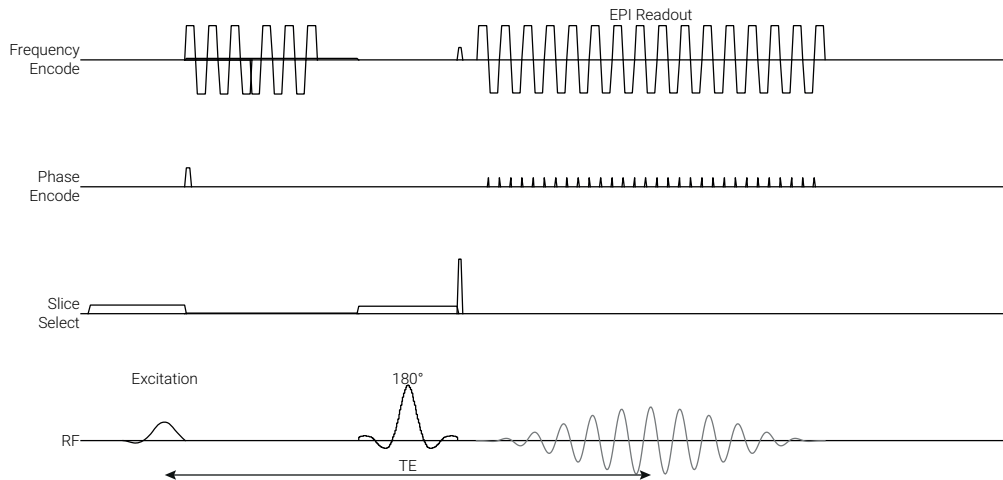


Figure 3.2: A pulse sequence diagram of the SE-EPI scheme.

Multi-Echo Turbo Spin Echo

This method also uses a multi-slice spin echo acquisition however unlike the simple spin echo method, uses a multishot Turbo Spin Echo (TSE) readout. Acquisition parameters for in-vivo scanning are FOV = $288 \times 288 \times 25$ mm, voxel size = $3 \times 3 \times 5$ mm 3 , TR = 3000 ms, FA = 90°, SENSE = 2.55 and TSE factor = 10; the sequence is respiratory triggered and has an acquisition time of approximately 4 minutes depending on breathing rate. For phantom scanning, the following parameters are modified FOV = $250 \times 250 \times 6$ mm, voxel size = $0.9 \times 0.9 \times 6$ mm 3 and respiratory triggering is removed. Volumes are

3.2. Methods

collected with TE between 18 ms and 130 ms in 13 ms steps.

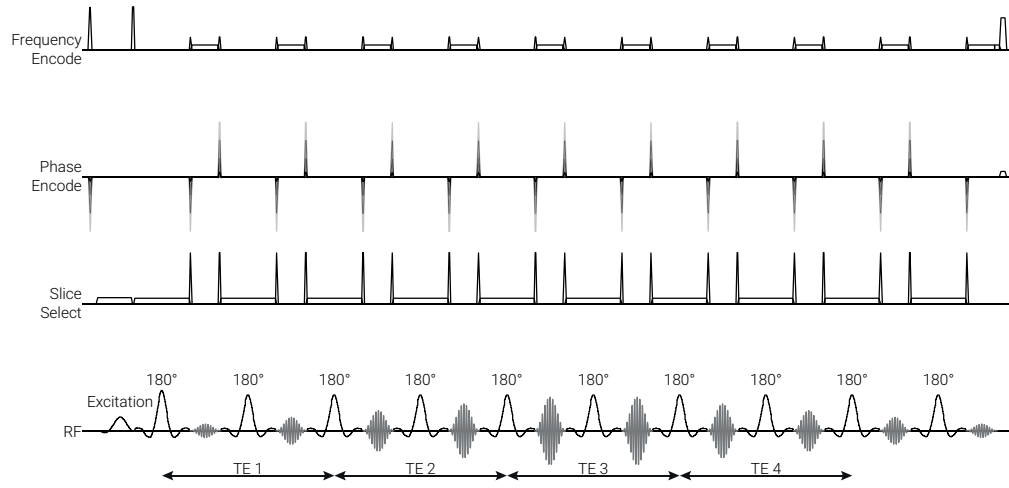


Figure 3.3: A pulse sequence diagram of the ME-TSE scheme.

Gradient Spin Echo

This method also uses a multi-slice spin echo acquisition but with a GraSE readout. Acquisition parameters for in-vivo scanning are $\text{FOV} = 288 \times 288 \times 25 \text{ mm}$, voxel size = $3 \times 3 \times 5 \text{ mm}^3$, $\text{TR} = 3000 \text{ ms}$, $\text{FA} = 90^\circ$, $\text{SENSE} = 2.55$ and TSE factor = 30, startup echoes = 1; the sequence is respiratory triggered and has an acquisition time of approximately 5 minutes depending on breathing rate. For phantom scanning, the following parameters are modified $\text{FOV} = 250 \times 250 \times 6 \text{ mm}$, voxel size = $0.9 \times 0.9 \times 6 \text{ mm}^3$ and respiratory triggering is removed. Volumes are collected with TE between 11.2 ms and 173.3 ms in 5.6 ms steps.

3.2. Methods

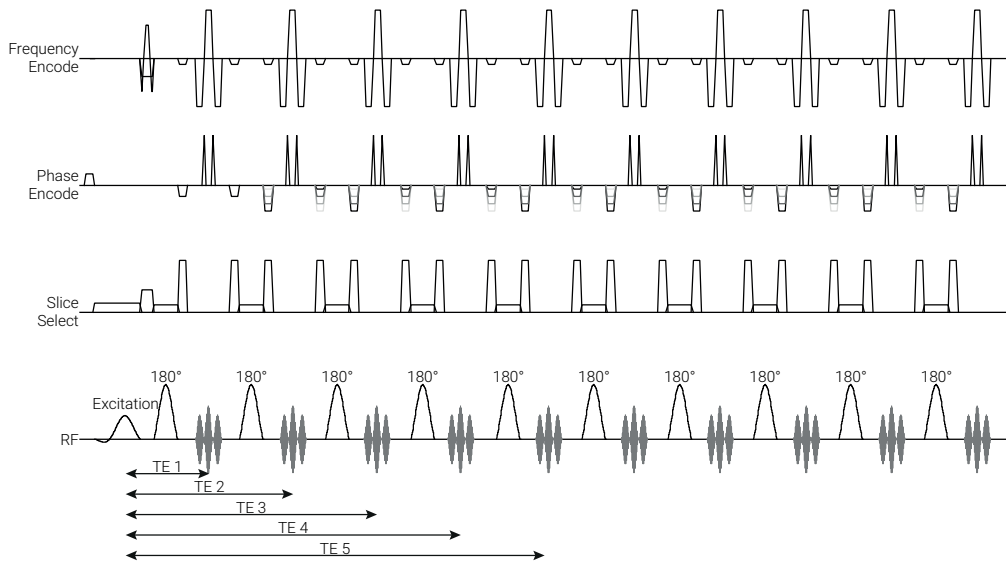


Figure 3.4: A pulse sequence diagram of the GraSE scheme.

T_2 Preparation

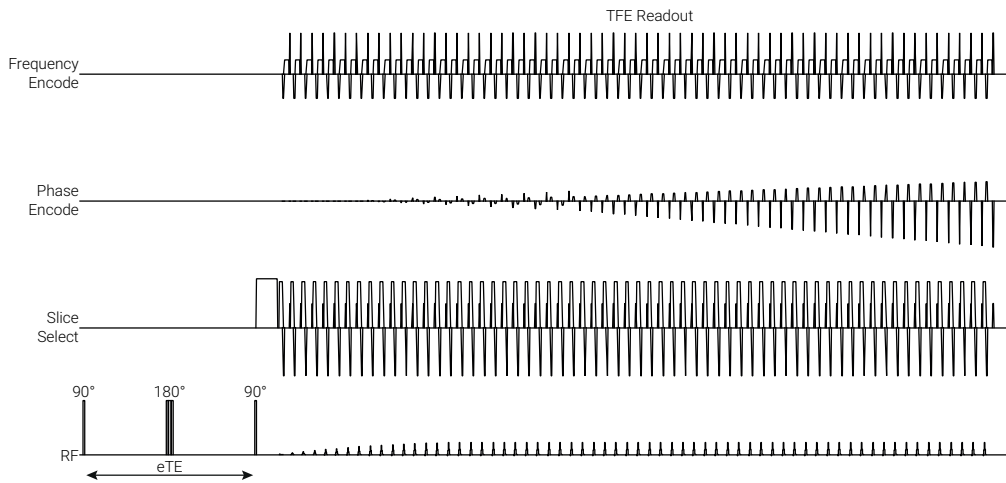


Figure 3.5: A pulse sequence diagram of the basic T_2 preparation scheme.

Basic T_2 Preparation

3.2. Methods

CPMG T_2 Preparation This technique uses a multi-slice Fast Field Echo (FFE) acquisition with a Turbo Field Echo Planar Imaging (TFEPI) readout. Varying degrees of T_2 weighting are applied as a series of 180° preparation pulses for a variable Effective Echo Time (eTE), this is similar to the sequence used in Section 4.2.2. Acquisition parameters for in-vivo scanning are $\text{FOV} = 288 \times 288 \times 25 \text{ mm}$, voxel size = $3 \times 5.65 \times 5 \text{ mm}^3$ (voxel size is limited by the EPI factor), $\text{TR} = 3000 \text{ ms}$, $\text{TE} = 5.3$, $\text{FA} = 90^\circ$, EPI factor = 17, SENSE = 3 and halfscan = 0.733; the sequence is respiratory triggered and has an acquisition time of approximately 6 minutes depending on breathing rate. As the voxel size is already at its minimum, the only modifications made for scanning the phantom are to decrease the FOV to $250 \times 250 \times 6 \text{ mm}$ and remove respiratory triggering. eTEs of 0, 40, 80 and 160 ms are used with three volumes acquired at each eTE

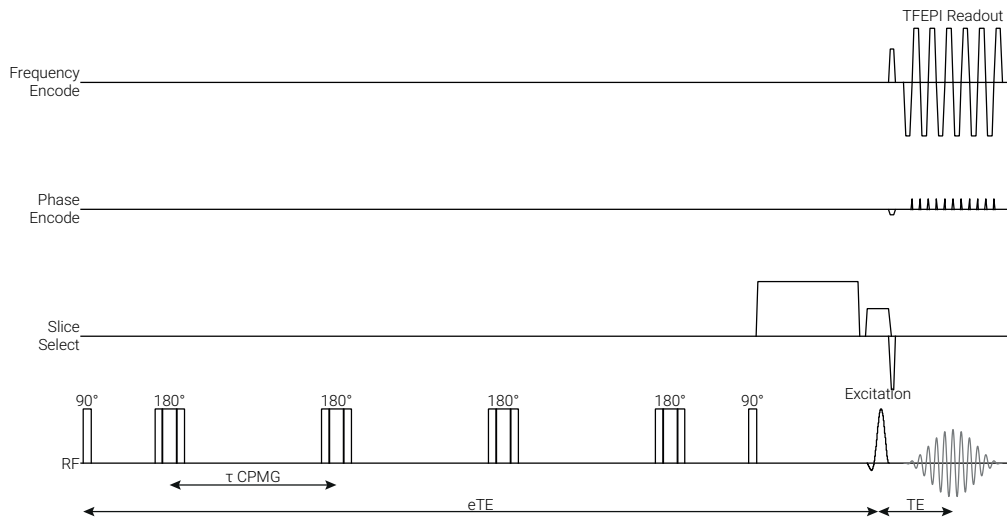


Figure 3.6: A pulse sequence diagram of the CPMG T_2 preperation scheme.

3.2.2 Post Processing

Generating T_2 Maps

The data is fit on a voxel by voxel basis using a least squares trust region reflective method to fit the data to Equation (3.1) to estimate T_2 and S_0 with an uncertainty in the fit [40]. For methods where multiple volumes are acquired at an TE, individual volumes

3.2. Methods

are used for the fit e.g. four points at each TE for the SE-EPI method rather than taking mean of the volumes for each TE, this makes potential data the discarding easier. This post-processing is performed by an in-house Python package. Once the T_2 maps have been generated, Region Of Interest (ROI) can be defined for different tissue types or phantom components.

$$S(t) = S_0 \cdot e^{-t/T_2} \quad (3.1)$$

Quantifying T_2 Accuracy

To access the accuracy of each method, the sequences were performed on the calibrated phantom with spheres of known T_2 . By calculating the mean T_2 for each sphere and comparing to the known T_2 it is possible to quantify the accuracy across a range of T_2 and summarise the overall accuracy by Pearson's correlation coefficient, (3.2).

$$r = \frac{\sum_{i=1}^n (x_i - \bar{x})(y_i - \bar{y})}{\sqrt{\sum_{i=1}^n (x_i - \bar{x})^2} \sqrt{\sum_{i=1}^n (y_i - \bar{y})^2}} \quad (3.2)$$

Quantifying Image Quality

Unfortunately MRI doesn't produce perfect images, every signal is subject to a degree of blurring or spreading out into surrounding voxels. The amount of this blurring is different for each sequence and can dramatically effect the readability of an image and ultimately its clinical utility. In MRI the amount and characteristics of the blur are usually spatially invariant, that is to say, if a voxel in the centre of an image is blurred over its five neighbouring voxels in the phase encode direction in the centre of the image, a voxel at the edge of the image would have the same five voxel blur applied to it. We wish to quantify the amount of blurring produced by each of the sequences outlined in 3.2.1.

The observed image, h , can be modeled as the ideal, unblurred signal, f distorted by a filter, g , figure 3.7. This distorting filter is known as the Point Spread Function (PSF) and is the theoretical signal produced by an infinitely small point source object or, in practice, the blurring observed in the imaging system produced when an object much smaller than

3.3. Results

the systems resolving power is imaged. In a spatially invariant system such as MRI the recorded signal is simply a convolution of the true signal and the PSF i.e. $f * g = h$. By fitting a gaussian to the PSF we can quantify the degree of blurring in the image.

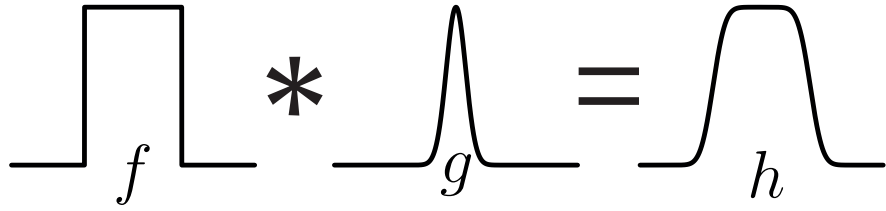


Figure 3.7: The convolution of the ideal signal, f , and the PSF, g , produces the measured signal, h .

To estimate the PSF we acquire an image of the National Institute of Standards and Technology (NIST) phantom at a much higher resolution than the standard T_2 mapping sequence to approximate the ideal signal. The phantom contains lots of clearly defined structures with high contrast edges, therefore, for the $3 \times 3 \text{ mm}^2$ in plane resolution of the sequences, the edges of the structures inside the phantom are smaller than the resolving power of the sequence

Assessment of In-Vivo Feasibility

3.3 Results

3.3.1 Sequence Accuracy

We began by comparing the quantitative accuracy of each of the proposed T_2 mapping methods (spin echo EPI, multi-echo TSE, GraSE and T_2 preparation). The QalibreMD System Standard Model 130 phantom used has fourteen spheres with T_2 between 5.35 ms and 645.8 ms spanning the range of T_2 expected in the kidneys, Figure 3.8. This phantom was scanned using each of the methods outlined in 3.2 and a ROI defined for each sphere.

3.3. Results

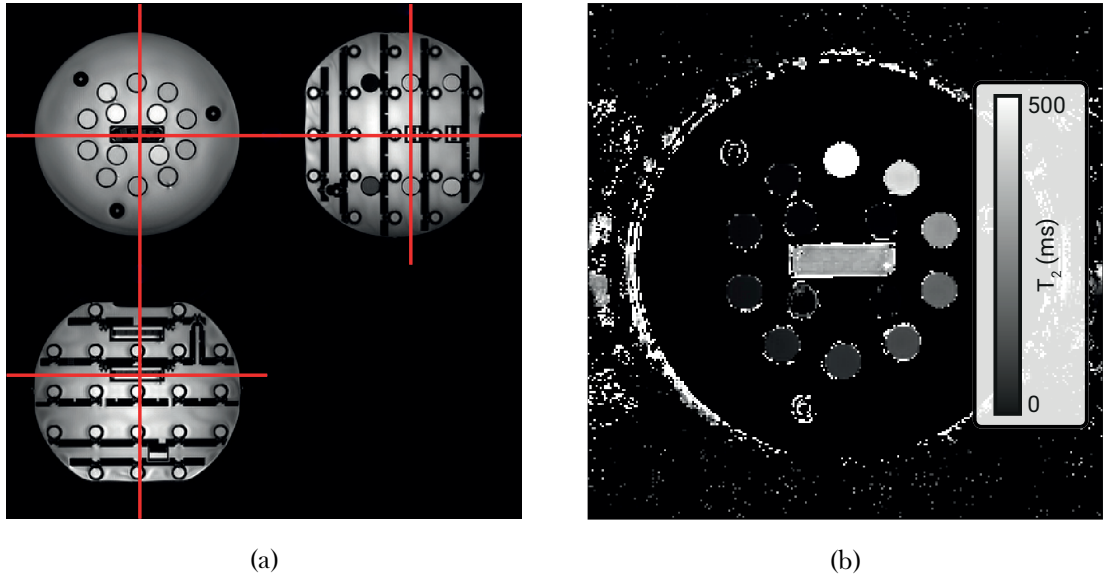


Figure 3.8: (a) The T_2 spheres inside the phantom. (b) An example T_2 map, in this case generated using the GraSE method.

The spin echo method produced vastly over-estimated readings for the spheres of T_2 less than 20 ms (Figures 3.9b) due to the longer minimum TE compared to the other methods. This can be seen in Figure 3.9a where the signal from the shortest T_2 spheres has already mostly decayed. This method did however deliver accurate measurements for the remaining spheres.

More accurate results were generated for shorter T_2 spheres using the ME-TSE method. The raw data (Figure 3.9c) is more noisy, with a sawtooth pattern visible, this additional noise manifests itself as inaccuracies in the longer T_2 measurements where the dynamic range over the TE sampled is smaller.

The GraSE method produced the most accurate measurements although still struggled to measure the sphere with a T_2 of 5.35 ms, Figure 3.9f. The large range of TE and number of volumes collected means this method produced the most accurate results. It also has the benefit of being able to be performed at high resolutions with voxel sizes of 0.9 x 0.9 mm unlike the SE-EPI and T_2 prep methods; this makes it well suited to both in-vivo and ex-vivo measurements.

The data collected using the T_2 prep method (Figures 3.9g and 3.9h) did not fit well due to its small number of data points and large degradation in image quality.

3.3. Results

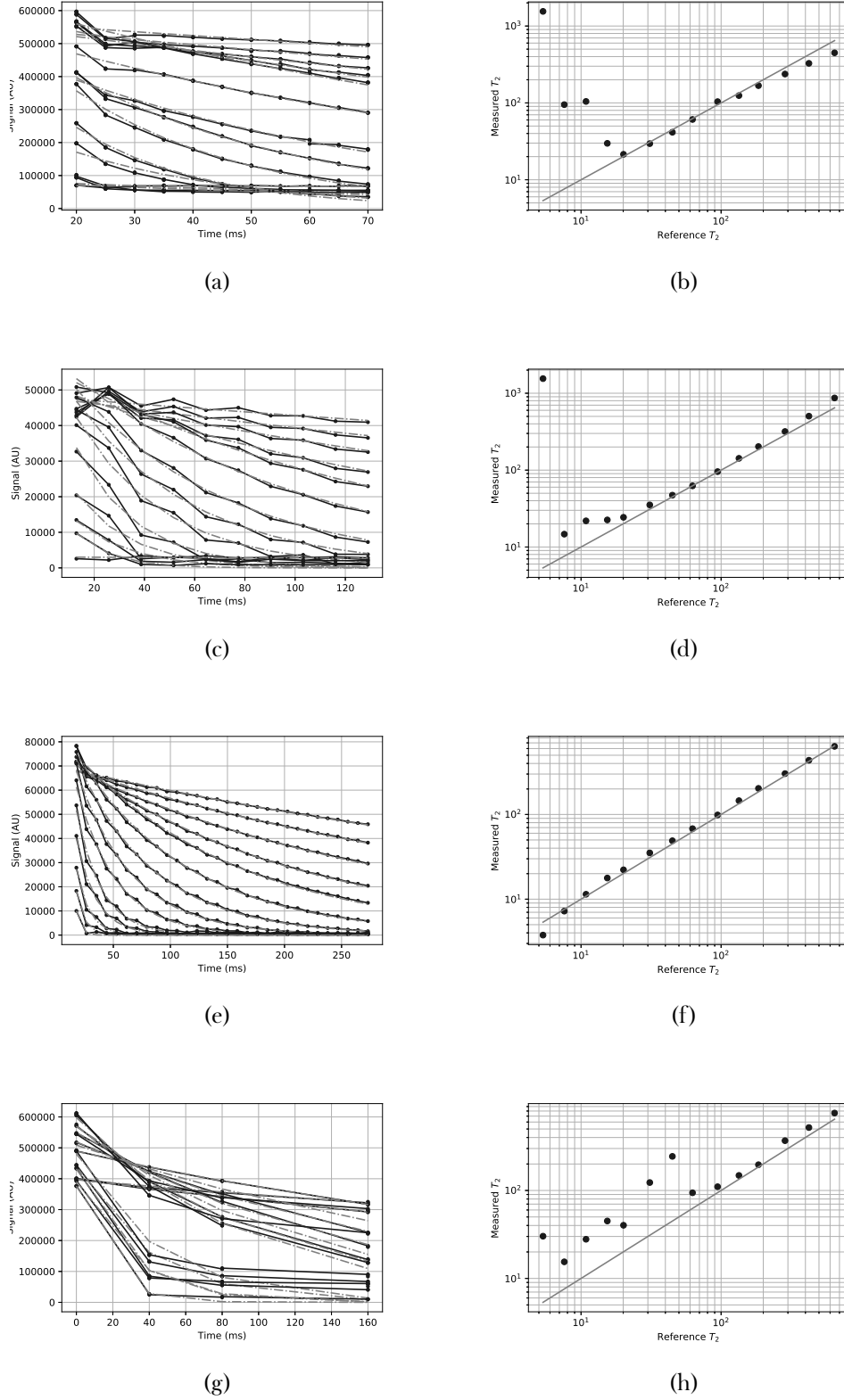


Figure 3.9: Figures (a), (c), (e) and (g) show the raw signal decay for each of the fourteen spheres and the fit decay. Figures (b), (d), (f) and (h) show how the fit T_2 compares to the literature value. Figures (a) and (b) show the results from the SE-EPI method, (c) and (d) show the results form the ME-TSE method, (e) and (f) show the results form the GraSE method and (g) and (h) show the results from the T_2 prep method.

3.3. Results

3.3.2 Image Quality

3.3.3 In-Vivo

T_2 maps using all four methods were collected on the same subject in the same scanning session to allow for a direct comparison of the in-vivo data.

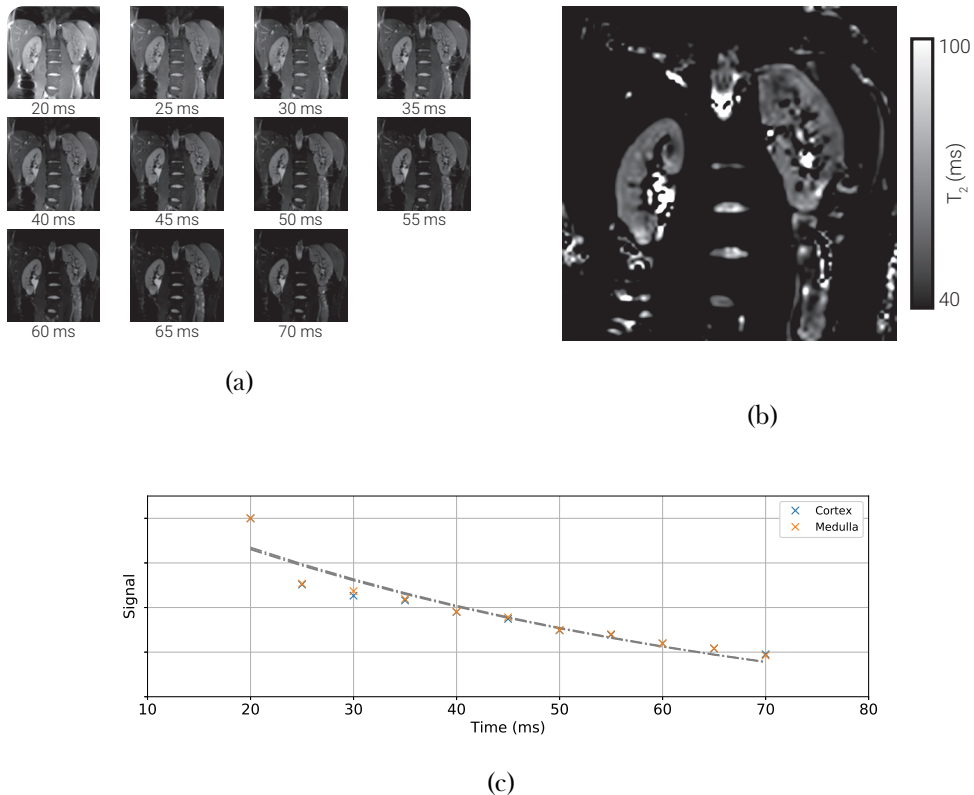


Figure 3.10: (a) The raw data used to generate the SE-EPI T_2 map. (b) An example slice from the SE-EPI T_2 map. (c) The signal decay for the renal cortex and medulla.

The SE-EPI method (Figure 3.10) generated maps with little blurring however there is also a lack of differentiation in T_2 between the renal cortex and medulla. The data collected at TE of 20 ms appears to be artificially high and leads to a reduction in fit T_2 . This sequence is the most susceptible of the methods to patient motion due to the acquisition method of a series per TE, this increase in motion is clear when scrolling through TE.

3.3. Results

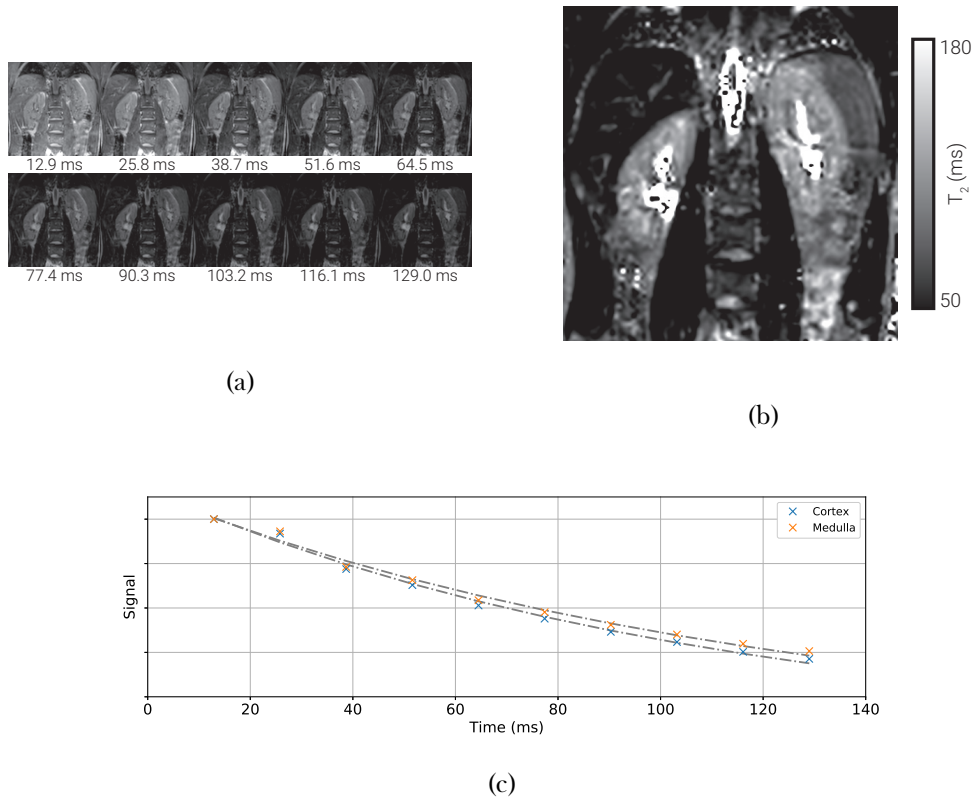


Figure 3.11: (a) The raw data used to generate the ME-TSE T_2 map. (b) An example slice from the ME-TSE T_2 map. (c) The signal decay for the renal cortex and medulla.

The map generated by the ME-TSE method (Figure 3.11) suffers from a large amount of blurring due to the relatively long echo train length. The number of echoes acquired is limited to the TSE factor therefore to acquire ten echoes, a TSE factor of ten needs to be used. This blurring leads to structures being obscured in the map and only a very small differentiation between cortex and medulla.

3.3. Results

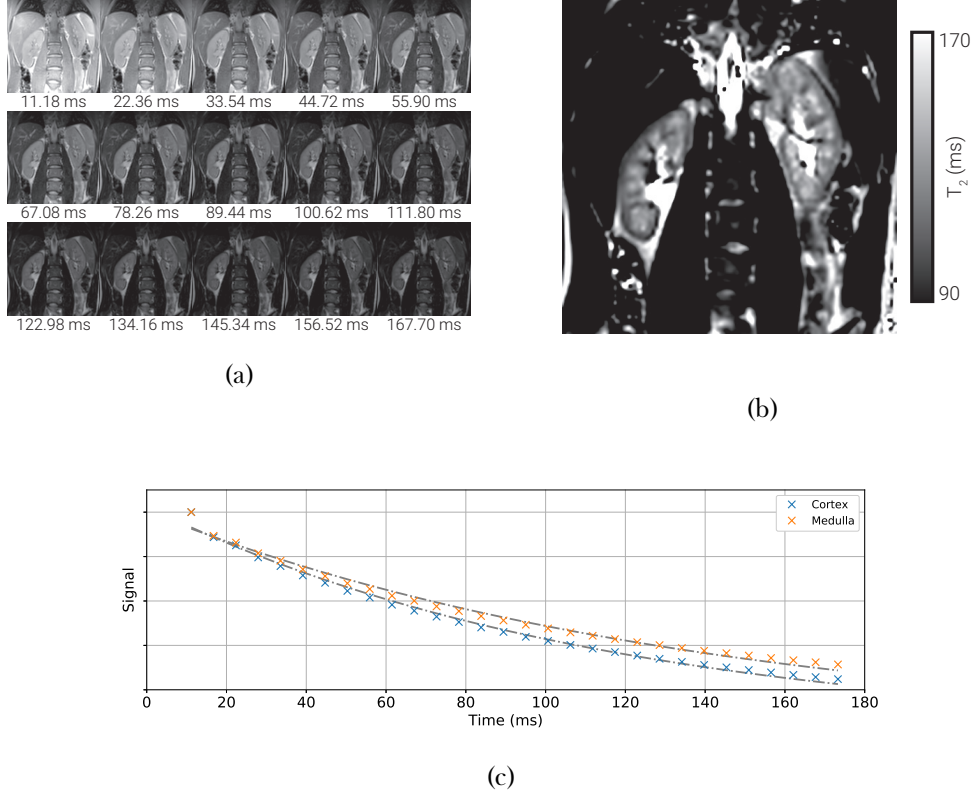


Figure 3.12: (a) The raw data used to generate the GraSE T_2 map. (b) An example slice from the GraSE T_2 map. (c) The signal decay for the renal cortex and medulla.

Using the GraSE method the data in Figure 3.12 was collected. There is a clear difference between cortical and medullary T_2 and the data fits well to a T_2 decay (Figure 3.12c). The signal from the first echo in Figure 3.12c is too intense, this effect was even more pronounced when no startup echoes were used. For tissues with a longer T_2 using two startup echoes would be preferable however this makes measurements of tissues with a short T_2 more inaccurate, as such a compromise of a single startup echo was used. The short echo-spacing made possible by GraSE means more TE can be sampled and therefore leads to a more accurate fit.

3.3. Results

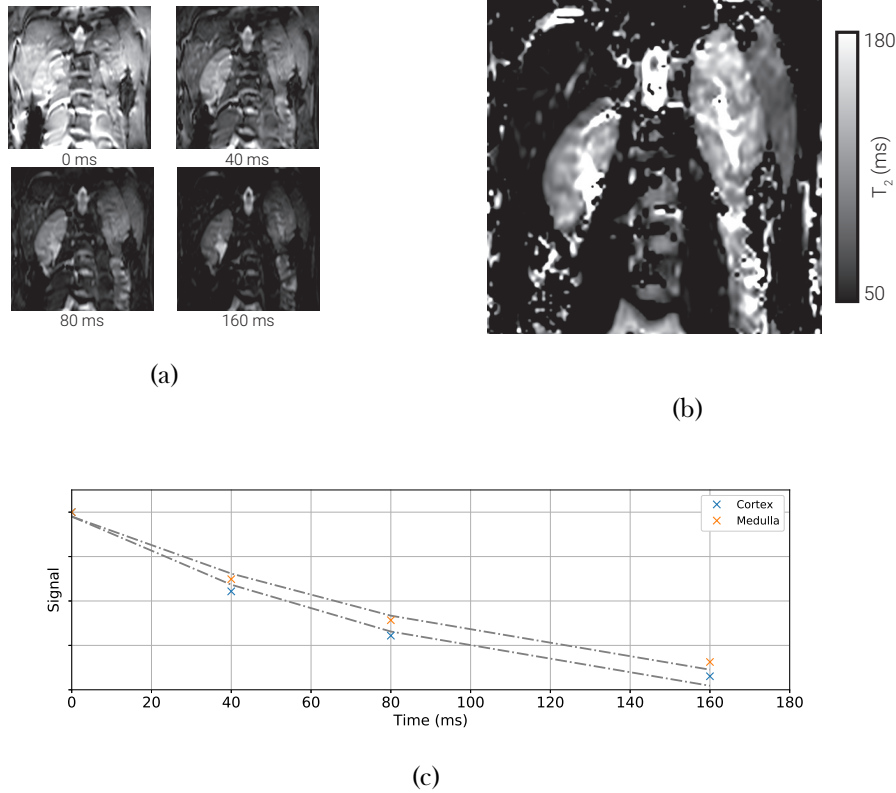


Figure 3.13: (a) The mean data at each eTE used to generate the T_2 preparation T_2 map. (b) An example slice from the T_2 preparation T_2 map. (c) The signal decay for the renal cortex and medulla.

The map made using the T_2 preparation method (Figure 3.13) suffers from noise in the raw data, this is despite there being three acquisitions at each eTE. When comparing Figure 3.13b to Figure 3.12b it's possible to see that some of the areas of greater T_2 do match with the medulla, however the degree of noise in 3.13b means it is un-useable on its own. The small number of eTE collected means the uncertainty in the fit T_2 is higher for this method.

The two methods that have delivered the highest image quality, SE-EPI and GraSE, produce substantially different values of T_2 in-vivo. Even when the data from the 20 ms volume is omitted from the SE-EPI fit, the T_2 is far lower. This is surprising given that when deployed on the phantom, this protocol delivered accurate results over the range of T_2 we see in the kidneys. This disparity is due to the additional confounding factors of diffusion and flow that are present in the body. These factors do not affect the GraSE sequence to the same degree as the SE-EPI sequence.

3.4 Discussion

Of the methods explored, the GraSE sequence produced the most accurate results on the phantom and superior image quality in-vivo, we will use this sequence in T_2 mapping going forward.

3.5 Conclusion

3.6 Acknowledgements

We are grateful for access to the University of Nottingham's Augusta high performance computing service.

3.7 References

1. Daniel, A., Cox, E., Buchanan, C. & Francis, S. *A Comparison of T2 Mapping Methods in the Kidneys* in *Proc. Intl. Soc. Mag. Reson. Med.* 28 International Society of Magnetic Resonance in Medicine Annual Meeting (Online, Aug. 2020).
2. Tofts, P. *Quantitative MRI of the Brain: Measuring Changes Caused by Disease* 688 pp. ISBN: 978-0-470-84721-3. Google Books: RbFrAAAAMAAJ (Wiley, 2003).
3. Buchanan, C. E. *et al.* Quantitative Assessment of Renal Structural and Functional Changes in Chronic Kidney Disease Using Multi-Parametric Magnetic Resonance Imaging. *Nephrology Dialysis Transplantation* (29th June 2019).
4. Chapman, A. B. *et al.* Kidney Volume and Functional Outcomes in Autosomal Dominant Polycystic Kidney Disease. *Clinical Journal of the American Society of Nephrology* **7**, 479–486. ISSN: 1555-9041, 1555-905X (1st Mar. 2012).
5. Gong, I. H. *et al.* Relationship Among Total Kidney Volume, Renal Function and Age. *The Journal of Urology* **187**, 344–349. ISSN: 0022-5347 (Jan. 2012).
6. Bull, S. *et al.* Human Non-Contrast T1 Values and Correlation with Histology in Diffuse Fibrosis. *Heart* **99**, 982–987. ISSN: 1355-6037, 1468-201X (1st July 2013).
7. Ferreira, V. M. *et al.* T1 Mapping for the Diagnosis of Acute Myocarditis Using CMR: Comparison to T2-Weighted and Late Gadolinium Enhanced Imaging. *JACC: Cardiovascular Imaging* **6**, 1048–1058. ISSN: 1936-878X (1st Oct. 2013).
8. Hoad, C. L. *et al.* A Study of T1 Relaxation Time as a Measure of Liver Fibrosis and the Influence of Confounding Histological Factors. *NMR in Biomedicine* **28**, 706–714. ISSN: 1099-1492 (2015).
9. Luetkens, J. A. *et al.* Quantification of Liver Fibrosis at T1 and T2 Mapping with Extracellular Volume Fraction MRI: Preclinical Results. *Radiology* **288**, 748–754. ISSN: 0033-8419 (26th June 2018).
10. Friedli, I. *et al.* New Magnetic Resonance Imaging Index for Renal Fibrosis Assessment: A Comparison between Diffusion-Weighted Imaging and T1 Mapping with Histological Validation. *Scientific Reports* **6**. ISSN: 2045-2322. pmid: 27439482 (21st July 2016).
11. Gillis, K. A. *et al.* Non-Contrast Renal Magnetic Resonance Imaging to Assess Perfusion and Corticomedullary Differentiation in Health and Chronic Kidney Disease. *Nephron* **133**, 183–192. ISSN: 1660-8151, 2235-3186 (2016).

3.7. References

12. Cox, E. F. *et al.* Multiparametric Renal Magnetic Resonance Imaging: Validation, Interventions, and Alterations in Chronic Kidney Disease. *Frontiers in Physiology* **8**. ISSN: 1664-042X (2017).
13. Hueper, K. *et al.* Functional MRI Detects Perfusion Impairment in Renal Allografts with Delayed Graft Function. *American Journal of Physiology-Renal Physiology* **308**, F1444–F1451. ISSN: 1931-857X (29th Apr. 2015).
14. Artz, N. S. *et al.* Arterial Spin Labeling MRI for Assessment of Perfusion in Native and Transplanted Kidneys. *Magnetic Resonance Imaging* **29**, 74–82. ISSN: 0730-725X (1st Jan. 2011).
15. Ren, T. *et al.* Evaluation of Renal Allografts Function Early after Transplantation Using Intravoxel Incoherent Motion and Arterial Spin Labeling MRI. *Magnetic Resonance Imaging* **34**, 908–914. ISSN: 0730-725X (1st Sept. 2016).
16. Niles, D. J. *et al.* Longitudinal Assessment of Renal Perfusion and Oxygenation in Transplant Donor-Recipient Pairs Using ASL and BOLD MRI. *Investigative radiology* **51**, 118–120. ISSN: 0020-9996 (Feb. 2016).
17. Rossi, C. *et al.* Histogram Analysis of Renal Arterial Spin Labeling Perfusion Data Reveals Differences Between Volunteers and Patients With Mild Chronic Kidney Disease. *Investigative Radiology* **47**, 490–496. ISSN: 0020-9996 (Aug. 2012).
18. Tan, H., Koktzoglou, I. & Prasad, P. V. Renal Perfusion Imaging with Two-Dimensional Navigator Gated Arterial Spin Labeling. *Magnetic Resonance in Medicine* **71**, 570–579. ISSN: 1522-2594 (2014).
19. Eckerbom, P. *et al.* Multiparametric Assessment of Renal Physiology in Healthy Volunteers Using Noninvasive Magnetic Resonance Imaging. *American Journal of Physiology-Renal Physiology* **316**, F693–F702. ISSN: 1931-857X (16th Jan. 2019).
20. Schley, G. *et al.* Multiparametric Magnetic Resonance Imaging of Experimental Chronic Kidney Disease: A Quantitative Correlation Study with Histology. *PLOS ONE* **13**, e0200259. ISSN: 1932-6203 (16th July 2018).
21. Hueper, K. *et al.* Kidney Transplantation: Multiparametric Functional Magnetic Resonance Imaging for Assessment of Renal Allograft Pathophysiology in Mice. *Investigative Radiology* **51**, 58–65. ISSN: 0020-9996 (Jan. 2016).
22. Gouya, H. *et al.* Rapidly Reversible Myocardial Edema in Patients with Acromegaly: Assessment with Ultrafast T2 Mapping in a Single-Breath-Hold MRI Sequence. *American Journal of Roentgenology* **190**, 1576–1582. ISSN: 0361-803X (1st June 2008).

3.7. References

23. Giri, S. *et al.* T2 Quantification for Improved Detection of Myocardial Edema. *Journal of Cardiovascular Magnetic Resonance* **11**, 56. ISSN: 1532-429X (30th Dec. 2009).
24. Naßenstein, K. *et al.* Cardiac MRI: T2-Mapping Versus T2-Weighted Dark-Blood TSE Imaging for Myocardial Edema Visualization in Acute Myocardial Infarction. *RöFo - Fortschritte auf dem Gebiet der Röntgenstrahlen und der bildgebenden Verfahren* **186**, 166–172. ISSN: 1438-9029, 1438-9010 (Feb. 2014).
25. Guo, H. *et al.* Myocardial T2 Quantitation in Patients with Iron Overload at 3 Tesla. *Journal of Magnetic Resonance Imaging* **30**, 394–400. ISSN: 1522-2586 (2009).
26. Krittayaphong, R. *et al.* Detection of Cardiac Iron Overload with Native Magnetic Resonance T1 and T2 Mapping in Patients with Thalassemia. *International Journal of Cardiology* **248**, 421–426. ISSN: 0167-5273 (1st Dec. 2017).
27. Neema, M. *et al.* T1- and T2-Based MRI Measures of Diffuse Gray Matter and White Matter Damage in Patients with Multiple Sclerosis. *Journal of Neuroimaging* **17**, 16S–21S. ISSN: 1552-6569 (2007).
28. Rugg-Gunn, F. J., Boulby, P. A., Symms, M. R., Barker, G. J. & Duncan, J. S. Whole-Brain T2 Mapping Demonstrates Occult Abnormalities in Focal Epilepsy. *Neurology* **64**, 318–325. ISSN: 1526-632X (25th Jan. 2005).
29. Knight, M. J. *et al.* Quantitative T2 Mapping of White Matter: Applications for Aging and Cognitive Decline. *Physics in Medicine and Biology* **61**, 5587–5605. ISSN: 0031-9155 (July 2016).
30. Vymazal, J. *et al.* T1 and T2 in the Brain of Healthy Subjects, Patients with Parkinson Disease, and Patients with Multiple System Atrophy: Relation to Iron Content. *Radiology* **211**, 489–495. ISSN: 0033-8419 (1st May 1999).
31. De Bazeilair, C. M. J., Duhamel, G. D., Rofsky, N. M. & Alsop, D. C. MR Imaging Relaxation Times of Abdominal and Pelvic Tissues Measured in Vivo at 3.0 T: Preliminary Results. *Radiology* **230**, 652–659. ISSN: 0033-8419 (1st Mar. 2004).
32. Zhang, J. L. *et al.* Reproducibility of $R2^*$ and $R2$ Measurements in Human Kidneys in Proc. Intl. Soc. Mag. Reson. Med. 19 ISMRM. **19** (2011), 2954.
33. Li, X., Bolan, P. J., Ugurbil, K. & Metzger, G. J. Measuring Renal Tissue Relaxation Times at 7 T. *NMR in Biomedicine* **28**, 63–69. ISSN: 1099-1492 (2015).
34. De Boer, A. *et al.* Multiparametric Renal MRI: An Intrasubject Test–Retest Repeatability Study. *Journal of Magnetic Resonance Imaging* **n/a**. ISSN: 1522-2586 (16th Apr. 2020).

3.7. References

35. Mathys, C. *et al.* T2' Imaging of Native Kidneys and Renal Allografts – a Feasibility Study. *RöFo - Fortschritte auf dem Gebiet der Röntgenstrahlen und der bildgebenden Verfahren* **183**, 112–119. ISSN: 1438-9029, 1438-9010 (Feb. 2011).
36. Adams, L. C. *et al.* Multiparametric Assessment of Changes in Renal Tissue after Kidney Transplantation with Quantitative MR Relaxometry and Diffusion-Tensor Imaging at 3 T. *Journal of Clinical Medicine* **9**, 1551 (5 May 2020).
37. Franke, M. *et al.* Magnetic Resonance T2 Mapping and Diffusion-Weighted Imaging for Early Detection of Cystogenesis and Response to Therapy in a Mouse Model of Polycystic Kidney Disease. *Kidney International* **92**, 1544–1554. ISSN: 0085-2538 (1st Dec. 2017).
38. Adams, L. C. *et al.* Use of Quantitative T2 Mapping for the Assessment of Renal Cell Carcinomas: First Results. *Cancer Imaging* **19**, 35. ISSN: 1470-7330 (7th June 2019).
39. System Phantom for Diagnostic Quantitative MRI QalibreMD. <https://www.qalibre-md.com/system-phantom/> (2019).
40. Branch, M., Coleman, T. & Li, Y. A Subspace, Interior, and Conjugate Gradient Method for Large-Scale Bound-Constrained Minimization Problems. *SIAM Journal on Scientific Computing* **21**, 1–23. ISSN: 1064-8275 (1st Jan. 1999).

Chapter 4

Quantitative Methods to Measure Renal Oxygenation

Abstract

Measurements of oxygenation of blood entering and leaving the kidneys would be a highly desirable quantitative biomarker allowing the calculation of renal metabolic rate of oxygen. Two methods of measuring blood oxygen saturation using MRI have been developed for use in the brain, Susceptibility Based Oximetry (SBO) and T_2 Relaxation Under Spin Tagging (TRUST).

Here both methods are tailored for use in the abdomen, these modified sequences are compared to their unmodified counterparts in the controlled environment of the brain, verifying that the modifications do not affect the quantitative accuracy. The methods are then applied to measure oxygenation in the renal vein. The geometry of the renal vessels leads to a high degree of uncertainty when applying SBO however TRUST produced results concordant with literature.

To verify the TRUST was able to measure a change in renal oxygenation, a hyperoxia challenge was undertaken. Measurements of oxygen saturation in the renal vein were collected using TRUST and BOLD T_2^* maps, the current standard for assessing renal oxygenation, were collected while the subject was breathing room air, then pure oxygen. A $16 \pm 3\%$ increase in oxygenation was measured using TRUST whereas no significant difference in T_2^* was measured.

This work was presented as an aural presentation at the International Society of Magnetic Resonance in Medicine (ISMRM) 26th Annual Meeting (2018) [1].

4.1 Introduction

As part of a multi-parametric quantitative Magnetic Resonance Imaging (MRI) protocol, Section 1.2, properties such as haemodynamics, oxygenation, and microstructure are assessed in a single 45 minute scanning session [2, 3]. Currently oxygenation is assessed using Blood Oxygen Level Dependent (BOLD) T_2^* maps to measure oxygenation of different tissues within the kidney, predominately the separation in mean T_2^* between the renal cortex and medulla, an example of which is shown in Figure 4.1. These BOLD T_2^* maps are, however, affected by other factors such as susceptibility effects, shimming and baseline blood flow and thus may be limited in their ability to draw quantitative conclusions despite their widespread use [4, 5].



Figure 4.1: An example T_2^* map. A clear difference can be seen between the renal medulla and cortex.

A welcome addition to this multi-parametric model would be the assessment of Renal Metabolic Rate of Oxygen (RMRO_2); a measure analogous to the Cerebral Metabolic Rate of Oxygen (CMRO_2) [6]. This measure can be calculated via Equation (4.1),

$$\text{RMRO}_2 = (Y_a - Y_v) \times \text{RBF} \times [\text{Hct}] \quad (4.1)$$

where Y_a and Y_v are arterial and venous oxygen saturation respectively, RBF is renal blood flow (in mL/min) and Hct is the ratio of the volume of erythrocytes to the volume of the rest of the blood, known as haematocrit. RBF can be measured relatively easily using Phase Contrast (PC)-MRI [7] and Hct is usually taken to be 0.41 for healthy adults but can be measured from a simple blood test [8, 9] or using the correlation between T_1 of blood and its haematocrit [10]. This means that only a measurement of blood oxygen saturation via

a non-invasive protocol is required to generate a quantitative value of RMRO₂.

Blood oxygen saturation can be measured precisely via the insertion of catheters into the subject, however this is clearly an invasive process [11]. There are currently two well established methods of measuring blood oxygenation via MRI however, thus far, these techniques have only been used to measure oxygen saturation in the sagittal sinus, a prominent vein in the brain. These methods are T_2 Relaxation Under Spin Tagging (TRUST) [12–15] and Susceptibility Based Oximetry (SBO) [16–19]. TRUST builds on the ideas of an Arterial Spin Labelling (ASL) sequence in the fact that by subtracting control images from labelled images only blood is imaged. However, instead of labelling a slab of tissue in the neck and imaging a superior slice, when implementing TRUST the imaging plane is inferior to the labelled slab. By collecting a series of pairs of labelled and control images with different T_2 weightings it is possible to fit the data from the sagittal sinus to a T_2 relaxation and use a calibration curve to convert the value of T_2 to venous oxygenation [20]. SBO is based upon the differences in magnetic susceptibility between the blood and the surrounding tissue. Using a phase map it is possible to model this difference in susceptibility and using the known difference in susceptibility between fully oxygenated blood and fully deoxygenated blood, venous oxygenation can be calculated.

Here both of the above techniques are applied to study oxygenation in the renal vein in young healthy individuals to assess the technicalities of transferring these protocols from the brain to the body. Given that these techniques have already been used in the brain with a number of studies in the literature, the sequences are first implemented on the brain to assess oxygenation in the superior sagittal sinus, then adapted to work within the more challenging environment of applications within the abdomen. These adapted sequences are compared to the results gained using the established techniques in the brain before testing on the renal vein. An oxygen challenge is carried out to verify that changes in oxygenation can be measured in the renal vein. If proved successful these sequences will be incorporated into the multi-parametric renal MRI protocol.

4.2 Methods

Imaging was performed on a whole body 3 Tesla MRI scanner (Ingenia, Philips Medical Systems, The Netherlands) using a 32 channel head or body coil. Studies were carried out according to the principles of the Declaration of Helsinki and approved by either the Local Ethics Committee or the East Midlands Research Ethics Committee. Written informed consent was obtained from all subjects.

4.2.1 Susceptibility-Based Oximetry

MRI Protocol

The principle behind SBO is based on the fact that there is a difference in magnetic susceptibility between the blood within a vessel and the tissue surrounding it [21]. As outlined by Jain, if a blood vessel is modelled as a long paramagnetic cylinder, it is possible to calculate the oxygenation of the blood by knowing the phase difference between blood in the vessel and the surrounding tissue, the angle of the vessel to the B_0 field, the echo time of the scan and the subject's haematocrit [16]. This relationship is given by,

$$Y_v = \left[1 - \frac{2|\Delta\phi|}{\gamma TE \Delta \chi_{do} B_0 (\cos^2 \theta - 1/3) Hct} \right] \times 100, \quad (4.2)$$

where $\Delta\phi$ is the average phase difference between the blood in the vessel and the surrounding tissue, γ is the gyromagnetic ratio of a proton, TE is the echo time, $\Delta \chi_{do}$ is the susceptibility difference between fully deoxygenated and fully oxygenated blood ($4\pi \times 0.27$ p.p.m) [22, 23], B_0 is the static field strength, θ is the angle of the vessel to the B_0 field and Hct is the subjects haematocrit. Given haematocrit can be assumed or is measured with a blood test or by measuring the T_1 of the blood, this means that from a simple phase map it is possible to calculate Y_v . The optimum phase map for this purpose was produced using a 2D T_1 weighted Fast Field Echo (FFE) sequence with a flip angle of 25° , flow compensation, coil homogeneity correction and flyback. The Field Of View (FOV) was $230 \times 184 \times 29$ mm, matrix size of 400×300 , Repetition Time (TR) of 12 ms, Echo Time (TE) of 7.5 ms and three signal averages. This led to a total acquisition time of 9 seconds and as such could be completed in a single breath hold if required.

Analysis

Once the phase map has been acquired, a Region Of Interest (ROI) containing the superior sagittal sinus was defined. This mask was then dilated with concentric shells to generate the two ROI shown in Figure 4.2, note that the outer ROI has been constrained to within the brain during its dilation. There were no occurrences of phase wrapping in or immediately surrounding the superior sagittal sinus observed due to its small size and the high field homogeneity within the head and of the 3T scanner used. Any occurrences of phase wrapping could easily be corrected using Phase Region Expanding Labeller for Unwrapping Discrete Estimates (PRELUDE), a tool within fMRIIB Software Library (FSL) (fMRIIB, The University of Oxford) [24]. The average values of phase within these two ROI along with the angle of the vessel to the B_0 field, as calculated from the localisation scans can then be used with Equation (4.2) to calculate Y_v .

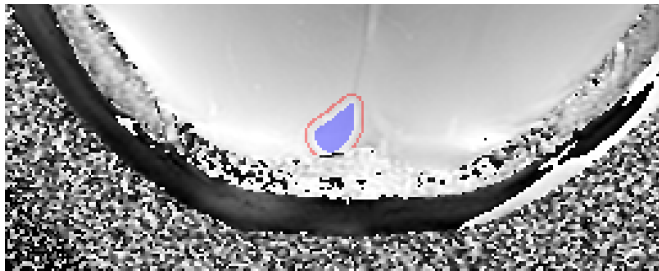


Figure 4.2: The region of interest averaged to find the intra-vascular phase (blue) and the region of interest used to find the phase of the surrounding tissue (red).

4.2.2 T_2 Relaxation Under Spin Tagging

MRI Protocol

The protocol for the TRUST MRI sequence in the brain involves the acquisition of a series of paired images using the pulse sequence shown in Figure 4.3a. A series of presaturation pulses using the Water suppression Enhanced through T_1 effects (WET) scheme are applied to the imaging slice, shown in Figure 4.3b, to reduce the signal from static tissue and reduce contamination of the magnetisation in the imaging slice by an imperfect labelling slab profile [25, 26]. In the first of each image pair, a labelling pulse is applied consisting of two successive slice-selective 90° Radio Frequency (RF) pulses to generate a 180° label. The next image in the sequence has a control pulse applied to it instead of a

4.2. Methods

labelling pulse, in this image the second of the 90° pulses is applied 180° out of phase to give zero net effect. As such any effects of magnetisation transfer related signal in the stationary tissue can be cancelled out because the net RF effect on the macromolecular spin magnetization is identical for both the labelling pulse and control pulse. This method of labelling is known as Transfer Insensitive Labelling Technique (TILT) and is widely used in literature for labelling in TRUST in the brain [27]. A series of non-selective T_2 preparation pulses are then applied to minimise the blood outflow effect and modulate the T_2 weighting of the image as in the Carr-Purcell-Meiboom-Gill (CPMG) sequence in Chapter 3, the time between the application of the labelling pulse and the T_2 preparation is known as the Post Label Delay (PLD). Finally a 90° excitation pulse is applied followed by a standard Echo Planar Imaging (EPI) readout at time TE later [13]. If the control image is subtracted from the labelled image then only the venous blood that flowed from the labelled slab to the imaging slice will be visible, as shown in Figure 4.4.

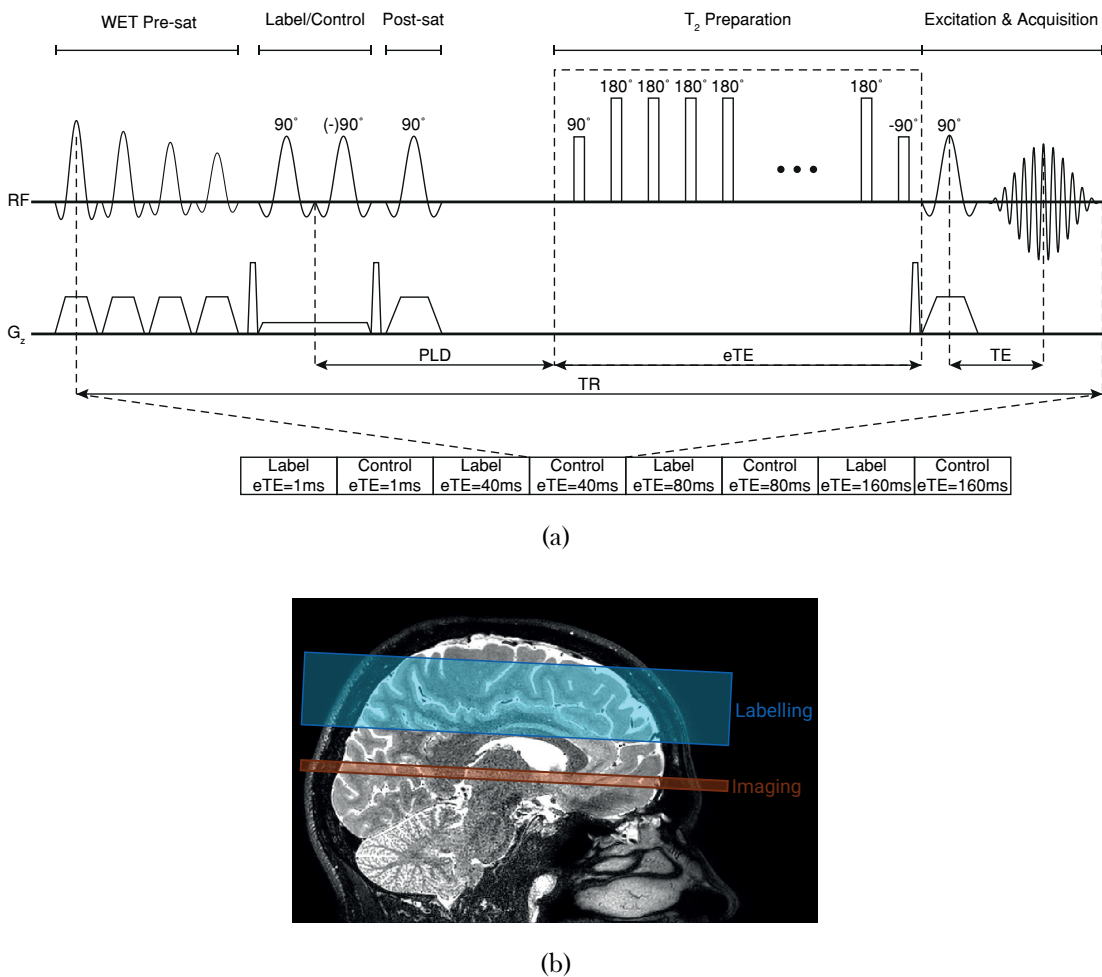


Figure 4.3: (a) The pulse sequence for TRUST MRI using the TILT labelling sequence. (b) The labelling and imaging volumes used for TILT tagging within the brain.

4.2. Methods

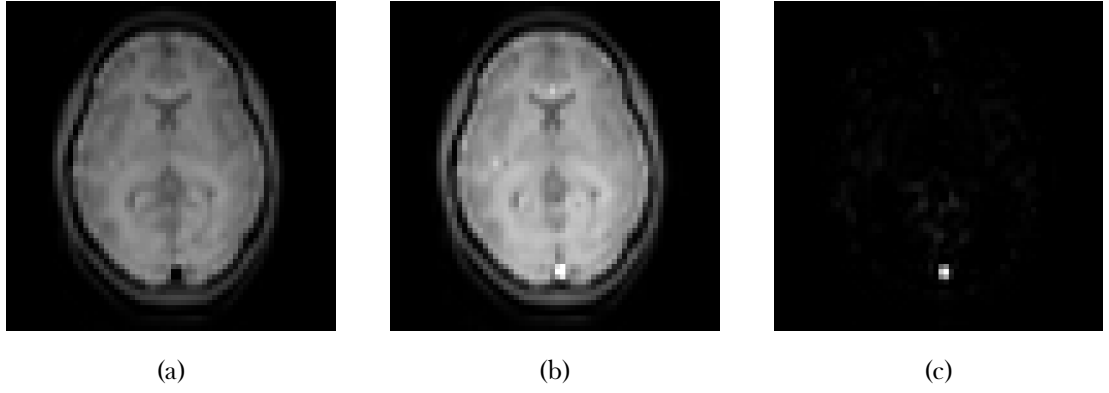


Figure 4.4: The control image, (a), is subtracted from the labelled image, (b), to generate a difference image, (c), of only the tagged blood.

This process is then repeated for another pair of images, however, this time the duration of the T_2 preparation is increased to a larger Effective Echo Time (eTE), this applies a T_2 weighting to the image in addition to the constant weighting caused by the regular TE. Three label/control image pairs were acquired with each eTE of 1 ms, 40 ms, 80 ms and 160 ms.

The resulting signal in the superior sagittal sinus of the difference between the labelled image and control image, ΔS , is defined by Equation (4.8)

$$\begin{aligned}
 \Delta S &= S_{\text{label}} - S_{\text{control}} \\
 &= S_{\text{blood label}} - S_{\text{blood control}} \\
 &= S_0 e^{eTE(1/T_1 - 1/T_2)}
 \end{aligned} \tag{4.8}$$

where $S_0 = 2e^{-T_1/T_1 - T_E/T_2^*}$ and; T_1 , T_2 and T_2^* are the relaxation constants of blood. If it is assumed that T_1 of blood is approximately 1624 ms [28] then it is possible to fit the collected data to a mono-exponential function and find an estimate of T_2 . It is deemed acceptable to use a mean value of T_1 as it will always be much greater than the value of T_2 and thus the possible small changes in T_1 due to blood oxygenation and haematocrit become negligible when fitting the T_2 curve.

The final step in this procedure is to convert the value of T_2 into one of Y_v . The relationship between T_2 and Y_v is relatively well known and as such a simple empirically derived calibration curve can be used for this conversion, Figure 4.5 [9, 29, 30].

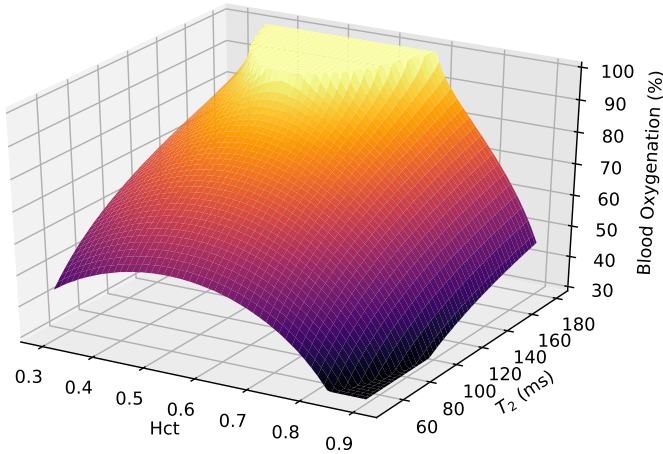


Figure 4.5: The calibration curve used to convert between T_2 and Y_v for a given haematocrit [31].

The parameters used in the brain TILT TRUST sequence were as follows: label slab thickness = 100 mm, imaging slice thickness = 5 mm, distance between centre of imaging slice and centre of labelling slice = 75 mm, FOV = 220×220×5 mm, matrix size = 64×64, voxel size = 3.44×3.44 mm, Sensitivity Encoding (SENSE) = 3, EPI factor = 15, T_1 = 1624 ms, PLD = 1022 ms, the choice of this value will be explored later, TR = 3000 ms, TE = 2.9 ms, eTE = 1 ms, 40 ms, 80 ms and 160 ms with three pairs of images acquired at each. This led to a total scan duration of approximately 84 seconds.

4.2. Methods

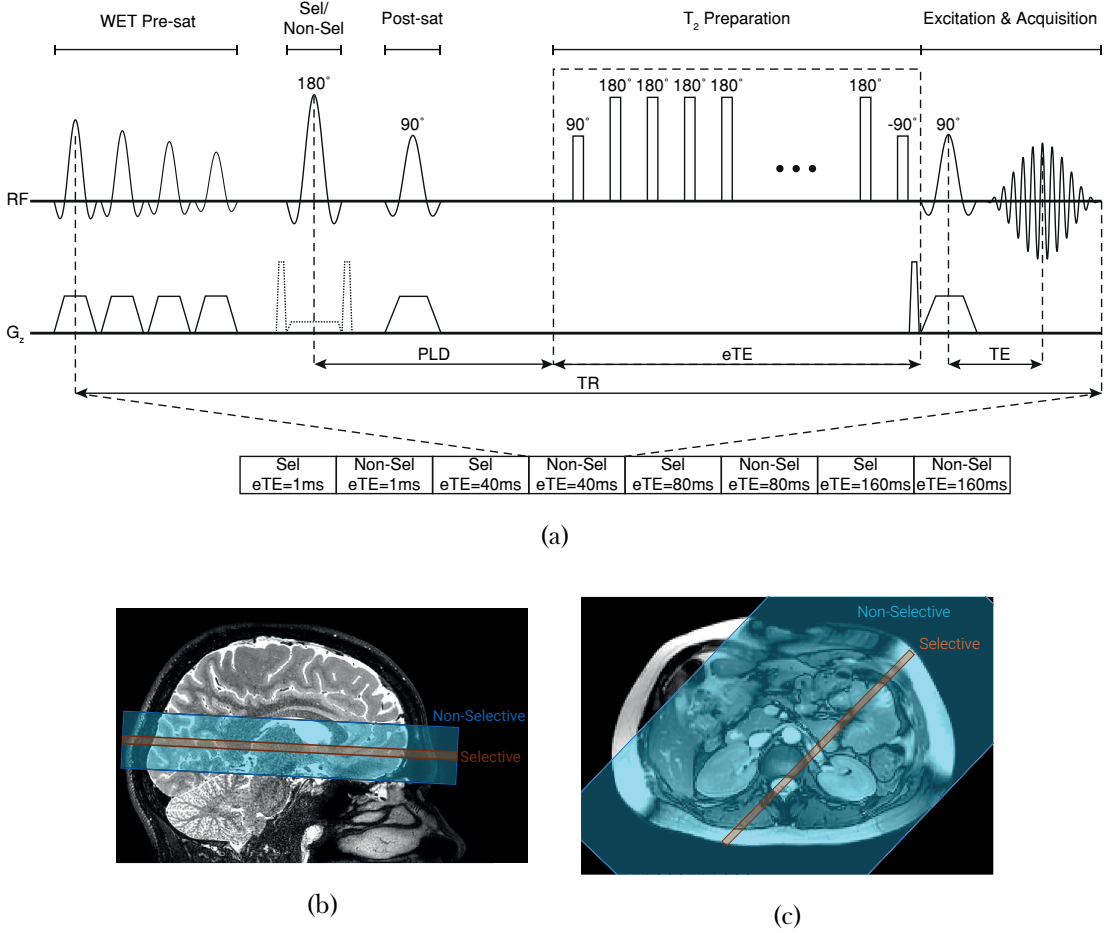


Figure 4.6: (a) The pulse sequence for TRUST MRI using the FAIR labelling sequence. (b) The selective and non-selective volumes used for tagging via FAIR in the brain. (c) The selective and non-selective volumes used for tagging via FAIR in the kidneys.

The main hurdle to be overcome when moving TRUST to the body is the inhomogeneity in the magnetic field caused by the far less homogeneous tissue susceptibilities within the body compared to the brain. These inhomogeneities mean that it is not possible to use TILT as the labelling method, instead the Flow-sensitive Alternating Inversion Recovery (FAIR) labelling scheme will be used [32], a diagram of this pulse sequence is shown in Figure 4.6a. In the FAIR labelling scheme a selective inversion pulse is applied with slice selective gradients turned on followed by T_2 preparation and acquisition to generate the first image in the pair, a non-selective inversion pulse is then applied with a lower slice selective gradient followed by T_2 preparation and then acquisition to generate the second image. An example of the raw images produced is shown in Figure 4.7. A schematic of the selective and non-selective slices in the brain and the renal vein are shown in Figures 4.6b and 4.6c respectively. This sequence also has the advantage of being far easier to plan. In the brain

4.2. Methods

having a separate labelling and imaging slice is relatively trivial however the flow of blood in the body is far less ordered and as such, the use of a selective slab within a non-selective slab yields far better results. Movement is a much greater problem in the body. Given the long acquisition time of TRUST it is impossible to carry out the scan in a breath hold, as such the sequence is respiratory triggered via a respiratory belt applied around the subjects chest. The total scan time is therefore dependent upon respiratory rate. Depending on the subject, a delay can be applied between the respiratory trigger and the labelling pulse to acquire images while the subject has fully exhaled.

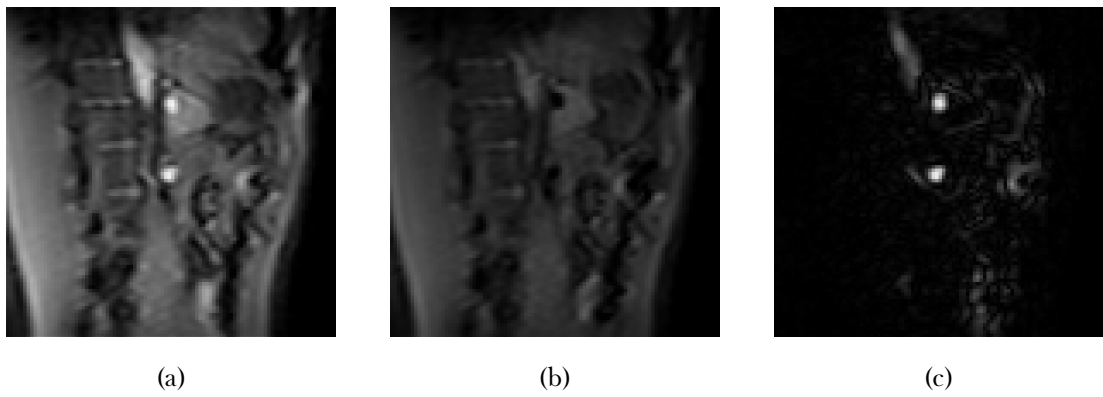


Figure 4.7: The raw images generated when using the FAIR labelling sequence on the kidneys. The non-selective image, (a), is subtracted from the selective image, (b), and generates (c), an image of only the untagged blood. The raw FAIR images from the brain are omitted as they are very similar to those seen in Figure 4.4.

When using the FAIR labelling sequence on the brain the following parameters were used: selective slab thickness = 25 mm, non-selective slab thickness = 400 mm, FOV = $220 \times 220 \times 5$ mm, matrix size = 64×64 , voxel size = $3.44 \times 3.44 \times 5$ mm, SENSE = 3, EPI factor = 15, T_1 = 1624 ms, PLD = 800 ms, TR = 7276 ms, TE = 2.9 ms, eTE = 1 ms, 40 ms, 80 ms and 160 ms with three pairs of images acquired at each. When used on the body, the parameters were as follows: selective slab thickness = 25 mm, non-selective slab thickness = 400 mm, FOV = $244 \times 244 \times 5$ mm, matrix size = 96×96 , voxel size = $3.44 \times 3.44 \times 5$ mm, SENSE = 3, EPI factor = 15, T_1 = 1624 ms, PLD = 1000 ms, the choice of this value will be explored later, TR = 8076 ms, TE = 2.9 ms, eTE = 1 ms, 40 ms, 80 ms and 160 ms with three pairs of images acquired at each.

4.2. Methods

Analysis

The analysis of the data collected using the above protocol was carried out using custom MATLAB (MathWorks, Natick, MA) software based upon code written by Liu and modified to work with data collected using the FAIR labelling method [33]. This software loads the data and carries out the subtraction of each image pair then presents a difference image to the user so the vessel can be drawn around. At this point the voxels with the greatest intensity within the vessel, four voxels when calculating Y_v for the superior sagittal sinus and nine voxels when working on the renal vein, are averaged, as are the intensities of each repeat eTE. These mean signals are then fit to Equation (4.8) to compute a value of T_2 with confidence bounds. The value of Y_v can then be found using the aforementioned calibration curve. Once the software has finished, it saves all outputs and intermediary variables to a file on the computer for later analysis.

4.2.3 Inducing Changes in Oxygenation of Blood in the Renal Vein

In order to assess the ability of these methods to measure a change in renal oxygenation, a method of inducing such a change in the kidneys needed to be devised. Looking at literature that has carried out similar studies, it is suggested that changes in renal oxygenation can be induced by either varying the subjects sodium intake, water intake or inspired oxygen level [34, 35].

Due to the challenges associated with controlling subjects diet for two weeks as was performed in Prijim [36], the use of sodium intake was discounted. From previous work we know that applying a large water load to subjects during the scanning session, as in Tumkur and Prasad [37, 38], can cause undesired effects on the resultant shim, as assessed by B_0 maps, due to the large susceptibility change adding such a large quantity of water to the abdomen can cause, as such, this method was also discounted leaving us to pursue an oxygen challenge.

This method consisted of localisers and anatomical images being collected followed by alternating BOLD T_2^* and TRUST scans while the subject was breathing room air to record a baseline. Pure oxygen was then delivered to the subject at 15 ℓ/min via a gas mask and, after a two minute wash in period, the BOLD T_2^* and TRUST scans were repeated. A visual representation of this protocol can be seen in Figure 4.8. The BOLD T_2^* scans had a slice

4.2. Methods

thickens of 5 mm, 12 echoes with an initial TE of 5 ms and subsequent echo spacing of 3 ms, the flip angle was 30°. The total scan time was approximately 17 seconds and was acquired during a single breath hold. The TRUST scans were conducted as per Section 4.2.2.

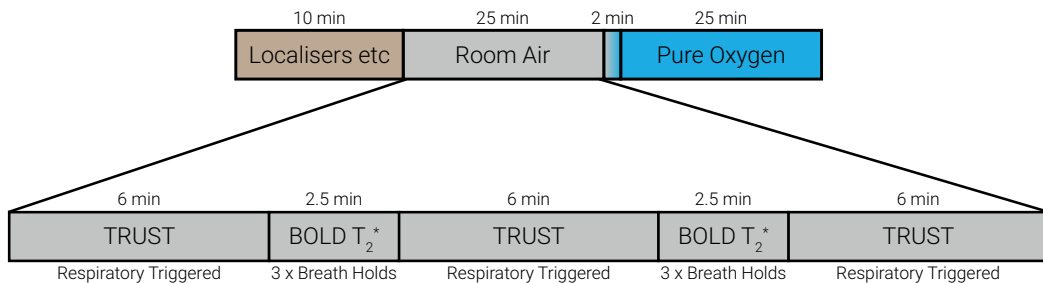


Figure 4.8: The protocol used to induce changes in renal oxygenation.

4.3 Results and Discussion

4.3.1 Susceptibility-Based Oximetry

Susceptibility-Based Oximetry in the Brain

Having collected data using the method outlined in 4.2.1 it was possible to use Equation (4.2) to estimate Y_v in the superior sagittal sinus to be $63 \pm 2.1\%$. This is consistent with the value reported by Liu of $61.1 \pm 1.4\%$ found in a multi centre TRUST trial with 250 participants over a wide range of ages and ethnicity distribution [15].

Susceptibility-Based Oximetry in the Renal Vein

Having calculated an acceptable result in the brain that agreed with literature it was possible to move onto applying techniques to assess oxygenation in the renal vein. A set of three phase maps were collected along with three localisers, one along each plane. If $\Delta\phi$ is plotted against θ for a typical Y_v of 85%, Figure 4.9 is produced. It can be seen that, for an expected Y_v , the phase difference is greatest if the vessel runs parallel to the B_0 field. No part of the renal vein is located parallel to the B_0 field, typically the angle is in the region of 75° (there is a large degree of variability in vasculature geometry between subjects) and as such delivers a very small phase difference. This coupled with the fact that the gradient of this function at these angles is large, meaning that the uncertainty in angle corresponds to a larger uncertainty in Y_v means it will unfortunately not be possible to use SBO to accurately measure Y_v within the renal vein.

4.3. Results and Discussion

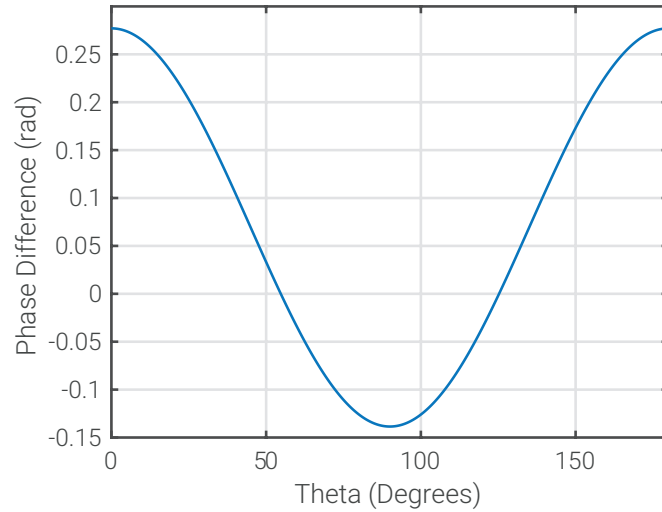


Figure 4.9: For a typical Y_v of 85% the phase difference produced by a vessel at a range of angles to B_0 .

This technique would perhaps be better suited to use in the liver to assess oxygenation in the portal vein. This vessel runs at a much smaller angle to the B_0 field and as such the model will still be valid with reasonable errors, Figure 4.10. This would potentially work much better than TRUST here as the sequence is much quicker and therefore will be less susceptible to errors caused by movement.

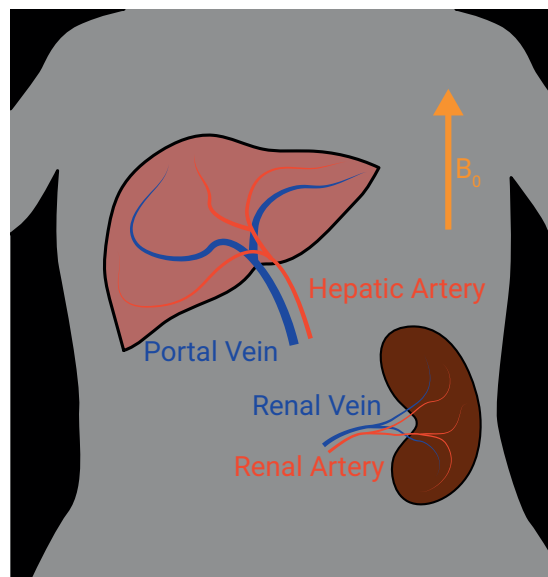


Figure 4.10: A schematic of the portal and renal veins entering the liver and left kidney respectively in relation to the B_0 field.

4.3.2 T_2 Relaxation Under Spin Tagging

TRUST in the Brain

To test if the FAIR labelling sequence delivered the same signal decay as the TILT sequence both labelling schemes were performed sequentially on the superior sagittal sinus with a PLD of 800 ms. The resulting normalised signals are shown in Figure 4.11.

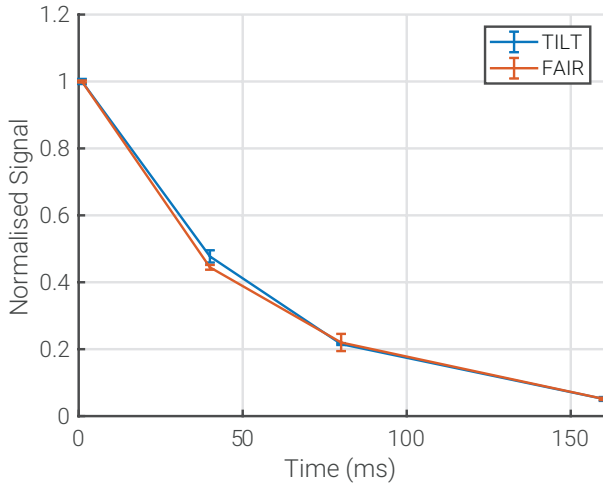


Figure 4.11: The signal decay within the superior sagittal sinus found using TRUST with both TILT and FAIR labelling sequences scaled by their initial signal intensities at eTE = 1 ms.

As can be seen these signals are in excellent agreement with the TILT sequence producing a T_2 of 52 ± 1 ms and the FAIR sequence producing a T_2 of 50 ± 2 ms, therefore in agreement within the bounds of error. This means that FAIR can be directly substituted for TILT in the TRUST sequence to measure Y_v in the superior sagittal sinus and can subsequently be used for the renal TRUST measurements.

To find the dependence PLD has upon the signal measured, scans were carried out at a range of delays from 400 ms to 1400 ms while using the FAIR labelling sequence. The signal from eTE=1 ms was then plot against label delay. Figure 4.12 shows the signal from the difference images. The maximum signal is observed with a PLD of 800 ms. This value is reached due to the balance between T_1 relaxation of the non-selective blood and inflow of unlabelled blood. This maximum in signal agrees with literature using the TILT labelling scheme [12]. By carrying out scans with this PLD the maximum Signal to Noise Ratio (SNR) will be achieved.

4.3. Results and Discussion

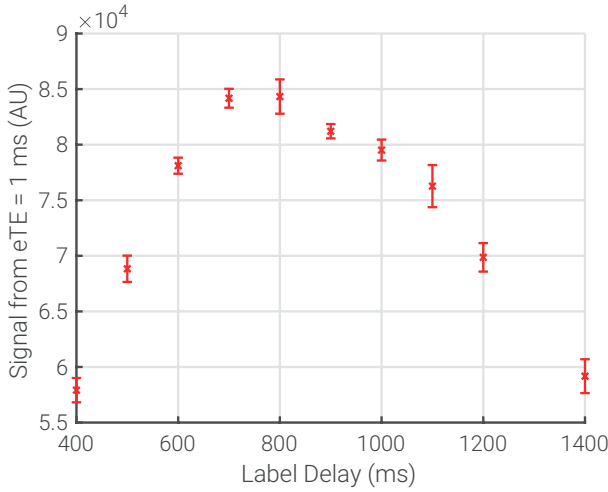


Figure 4.12: The mean signal from the first echo of each difference image over a range of PLD times.

T_2 should have no dependence upon PLD given the signal from the difference image will have the same decay in time, it will just be a lower intensity for non-optimal PLD thus leading to a larger confidence interval. To confirm this the fit values of T_2 were plotted against PLD, Figure 4.13.

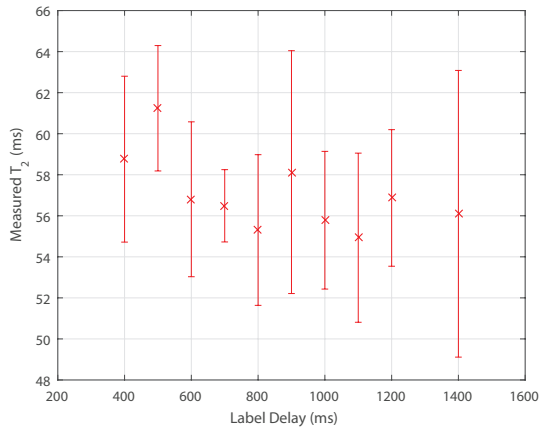


Figure 4.13: The dependence of T_2 upon PLD.

It can be seen that, as predicted, there is no relationship between T_2 and PLD. An increase in error with label delay was not observed, this effect may only show itself at larger values of PLD however for our purposes, simply confirming there is no large increase in error around our chosen PLD is sufficient. This means that if there is a variation in the optimum PLD between subjects due to the larger range in RBF compared to Cerebral Blood Flow (CBF) then this will not have an affect upon the value of T_2 and thus Y_v .

4.3. Results and Discussion

When the analysis is carried out on the images, the four brightest voxels of the difference image are averaged before the fitting occurs. This number of voxels is chosen due to the average size of the superior sagittal sinus however, for some subjects more voxels could be included, potentially yielding better results. To assess the variability in T_2 measurements with the number of voxels averaged, the analysis was run multiple times with one to twelve voxels included in the calculation. Multiple TRUST scans were performed on the same subject and averaged generating Figure 4.14a.

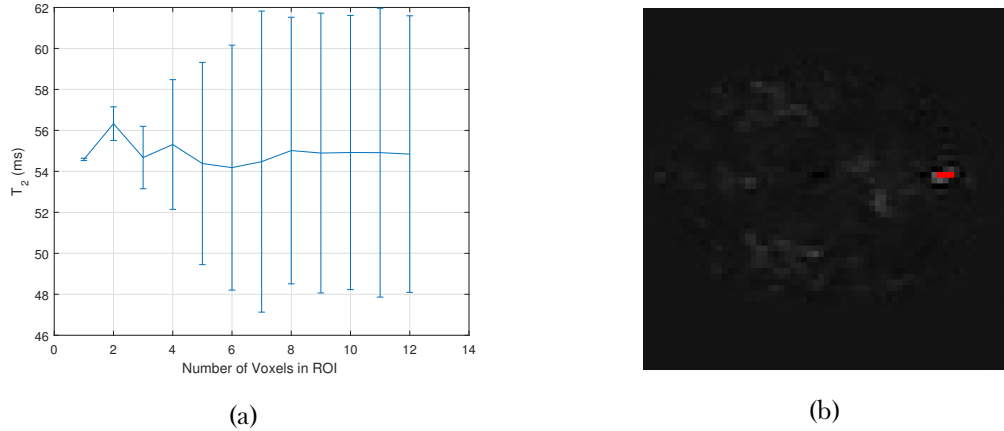


Figure 4.14: (a) The value of T_2 computed for the superior sagittal sinus with different numbers of voxels included in the calculation. (b) The difference image of the superior sagittal sinus with a three voxel ROI shown. This is already covering most of the vessel, hence the noise going up as more voxels are added to the calculation.

Although from Figure 4.14a it would appear that it would be best to only use the brightest voxel in the calculation due to its very small error and that it has the same value of T_2 as the results with far more voxels; this would not be a very robust method. It is fairly easy to conceive a greater than average level of noise being recorded on a single voxel in the relaxation and as such skewing the output of the calculation. The confidence interval is so large above six voxels because by this point the calculations are simply including the noise around the vessel rather than the signal from the blood within the sagittal sinus. Given these results, using four voxels in the calculation seems to be a reasonable balance between uncertainty and robustness.

To assess the repeatability of this measure, the optimised scan was repeated ten times on a single subject during one scanning session. This yielded a Y_v of $69.5 \pm 0.6\%$, a value consistent with literature [11, 15]. Given the success of the modified sequence on the superior

4.3. Results and Discussion

sagittal sinus, it was possible to attempt to measure Y_v in the renal vein.

TRUST in the Body

Ideal vessels to test the TRUST sequence within the body are the portal vein and hepatic artery as these vessels are large, have different oxygen saturations and can easily be imaged at the same time. Using the modified TRUST sequence the T_2 and oxygen saturation of the portal vein was found to be 109 ± 5 ms and 79.9 ± 0.8 % respectively; the T_2 and oxygen saturation of the hepatic artery was found to be 157 ± 10 ms and 100 ± 1 % respectively. This means that, as expected, the oxygen saturation in the hepatic artery is measured as greater than that of the portal vein and therefore the TRUST protocol is working as expected. Although normally the analysis would simply be based upon the mean of the brightest voxels in the difference image as outlined in Section 4.2.2, in Figure 4.15 a voxel by voxel analysis has been carried out for illustrative purposes.

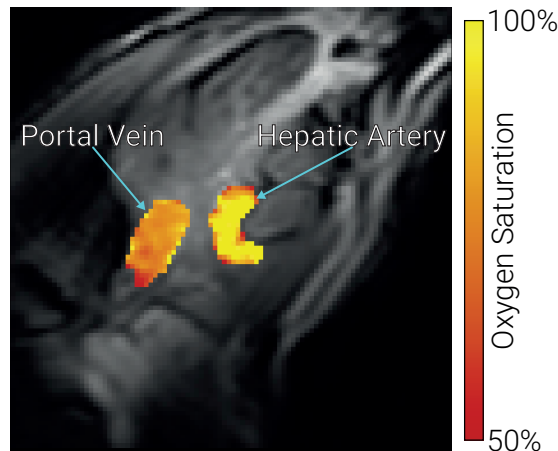


Figure 4.15: The oxygen saturation of the portal vein and hepatic artery measured using TRUST.

To assess if the PLD that generates the greatest signal is the same in the renal vein as in the superior sagittal sinus, a series of scans were collected with PLD ranging from 400 ms to 1400 ms and the signal from $eTE = 1$ ms recorded.

4.3. Results and Discussion

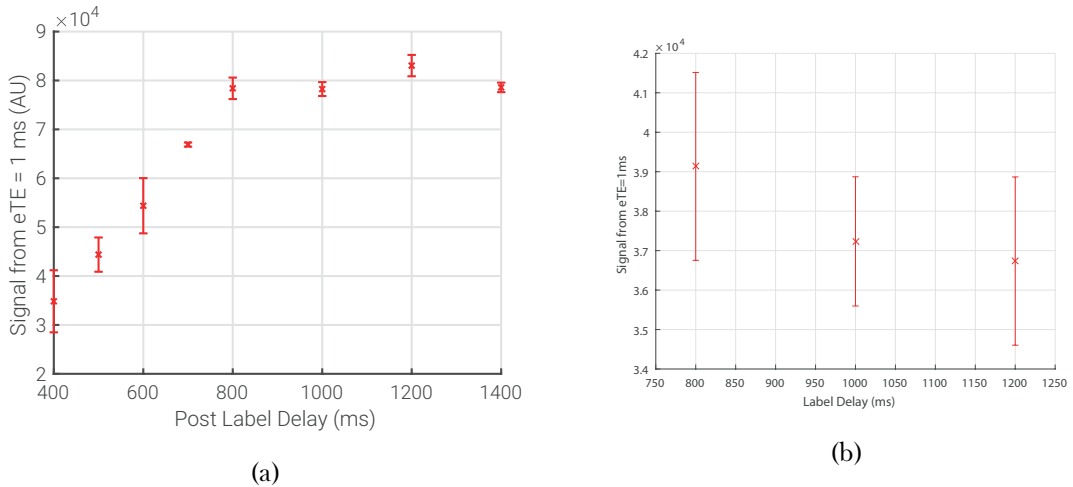


Figure 4.16: (a) The mean signal from the first echo of each difference image of the renal vein over a range of PLD. (b) Mean signal from the first echo versus PLD from a different subject.

As seen in Figure 4.16a the PLD producing the largest signal in the difference image of the renal vein is indeed different to that of the superior sagittal sinus. This is most likely due to differences in blood flow through each of these vessels, 413 ± 136 ml/min in the renal vein [2] and 285 ± 19 ml/min in the superior sagittal sinus [7]. Given the much larger uncertainty in blood flow in the renal vein, a different subject was scanned over a smaller range of PLD to ascertain if the PLD delivering the maximum signal varies much between subjects, Figure 4.16b.

The maximum signal for the first subject was achieved at a PLD of 1200 ms whereas for the second subject the maximum is at a PLD of 800 ms. Given that these subjects had a RBF either side of the mean and that there is little dependence of T_2 upon PLD it seems appropriate to use a PLD of 1000 ms for optimum signal in most subjects.

Given the larger size of the renal vein compared to the superior sagittal sinus, it would be better to include more voxels in the calculations when fitting to find a value of T_2 . Multiple scans were completed on a single subject and the value of T_2 found for each using one to twelve voxels in the fitting process. The results were averaged and plot in Figure 4.17a.

4.3. Results and Discussion

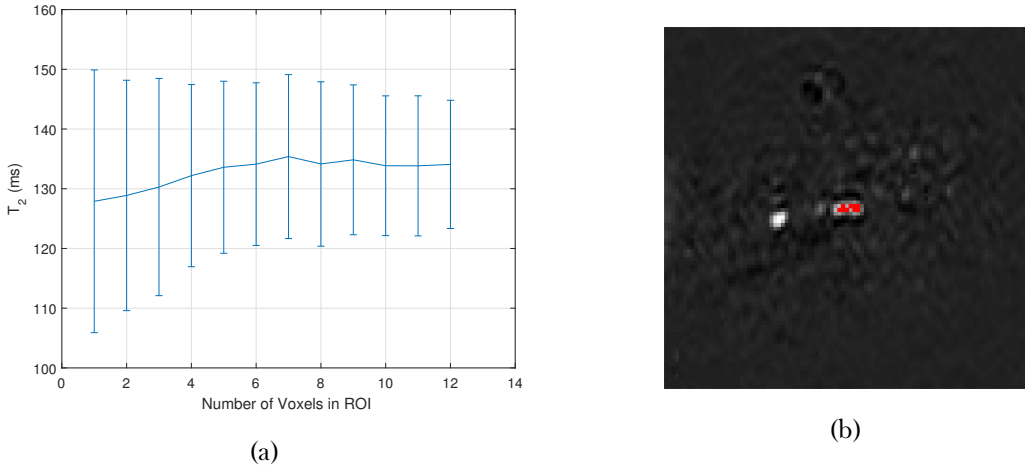


Figure 4.17: (a) The value of T_2 calculated for the renal vein with different numbers of voxels included in the calculation. (b) The difference image of the renal vein with a nine voxel ROI shown.

Unlike the results when this process was carried out on the superior sagittal sinus in Figure 4.14a, here the error decreases as more voxels are added to the calculation. This uncertainty comes from the large variation in T_2 for one voxel rather than a large error on the fit i.e. the error is coming from the differences between scans rather than the robustness of each scans results, this is precisely the concern that was raised with using a single voxel when discussing the superior sagittal sinus. As more voxels are added the error decreases until approximately six voxels are included, at this point the value of T_2 stops increasing and stays approximately constant. Once again, given the large variation in renal veins, it would be advisable to include slightly more than six voxels but not so many that in the cases of small vessels the algorithm is sampling surrounding tissue. Nine voxels seems to be a suitable middle ground as to work effectively with both small and large vessels.

To assess the repeatability of the measurements within the kidney, the same scan was repeated ten times in a single session with the optimised renal parameters. This yielded a T_2 of 135 ± 5 ms corresponding to a Y_v of $89 \pm 2\%$. The variation in measurements of Y_v in the renal vein are relatively substantial and show no dependence upon time so are therefore not likely due to physiological changes. The value of Y_v in the renal vein is much higher than in the sagittal sinus however is within the range found by Nielsen [39].

4.3. Results and Discussion

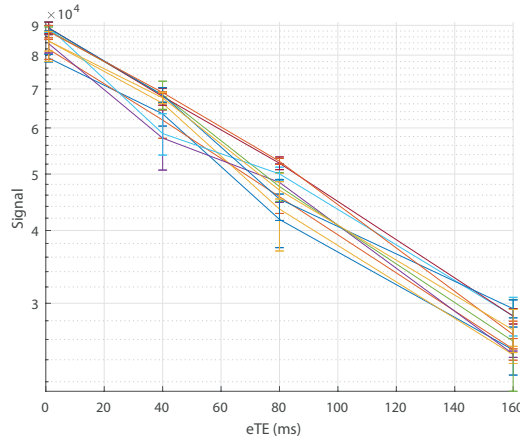


Figure 4.18: The T_2 relaxation curves of ten scans repeated on a single subject.

To compare the abilities of BOLD T_2^* maps and TRUST to measure changes in oxygenation in the kidneys, a hyperoxia challenge was conducted. In Figure 4.19a, no systematic, bulk change in T_2^* can be seen indicating that the change in T_2^* caused by the introduction of pure oxygen is dominated by other confounding factors. This is confirmed when ROI are defined for the renal cortex and renal medulla with the mean change in T_2^* found to be -2 ± 8 ms and -1 ± 6 ms respectively. When TRUST is used to measure the oxygen saturation in the renal vein an increase of 16 ± 3 % is observed, Figure 4.19b. This shows that it is possible to measure changes in renal oxygenation using TRUST that would be undetectable using the current standard, BOLD T_2^* mapping.

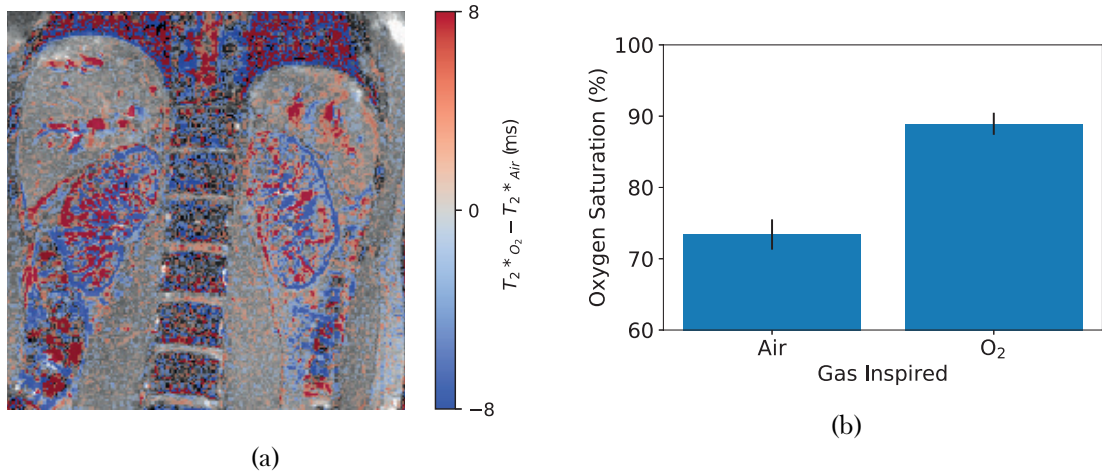


Figure 4.19: (a), The difference in T_2^* measured between baseline and the hyperoxia state. (b) The difference in Y_v measured using TRUST.

4.4 Conclusions and Future Work

This work shows promising results for the use of a modified TRUST sequence to measure oxygenation of blood within the body. The existing TRUST sequence was modified to be respiratory triggered and use the FAIR labelling scheme making it suitable for use in the body. Once these modifications had been carried out, parameters such as PLD and the number of voxels used in the ROI were optimised. The ability of TRUST to measure a change in renal oxygenation was successfully verified via a hyperoxia challenge which was able to measure an increase of $16 \pm 3\%$ where the current standard measurement of renal oxygenation, BOLD T_2^* maps, recorded no significant change.

Looking forward this work could be expanded by carrying out the hyperoxia challenge on more subjects. Although a small number of measurements were gathered on the hepatic vessels, further work could be undertaken to compare the use of SBO and TRUST to measure oxygenation in the portal vein in response to a hyperoxia challenge as conducted for the kidneys here. In the current protocol, haematocrit is assumed to be an average value of 0.41 unless a blood test has recently been undertaken. As stated above, there is a correlation between T_1 of blood and its haematocrit, this means that an estimate of the subjects haematocrit could be taken while they are in the scanner, thus leading to a more accurate measurement of oxygenation with only a small increase in scan time. This would be especially important when using TRUST on patients rather than healthy volunteers as their haematocrit has a larger variance.

4.5 Acknowledgements

We thank Hanzhang Lu for sharing the TRUST methodology.

4.6 References

1. Daniel, A., Cox, E., Buchanan, C., Bradley, C. & Francis, S. *Applying T2 Relaxation Under Spin Tagging (TRUST) to Assess Renal Oxygenation in the Kidney* in *Proc. Intl. Soc. Mag. Reson. Med.* 26 International Society of Magnetic Resonance in Medicine Annual Meeting (Paris, 21st July 2018).
2. Cox, E. F. *et al.* Multiparametric Renal Magnetic Resonance Imaging: Validation, Interventions, and Alterations in Chronic Kidney Disease. *Frontiers in Physiology* **8**. ISSN: 1664-042X (2017).
3. Buchanan, C. E. *et al.* Quantitative Assessment of Renal Structural and Functional Changes in Chronic Kidney Disease Using Multi-Parametric Magnetic Resonance Imaging. *Nephrology Dialysis Transplantation* (29th June 2019).
4. Pruijm, M., Milani, B. & Burnier, M. Blood Oxygenation Level-Dependent MRI to Assess Renal Oxygenation in Renal Diseases: Progresses and Challenges. *Frontiers in Physiology* **7**. ISSN: 1664-042X. pmid: 28105019 (5th Jan. 2017).
5. Niendorf, T. *et al.* How Bold Is Blood Oxygenation Level-Dependent (BOLD) Magnetic Resonance Imaging of the Kidney? Opportunities, Challenges and Future Directions. *Acta Physiologica* **213**, 19–38. ISSN: 1748-1716.
6. Chong, S. P., Merkle, C. W., Leahy, C. & Srinivasan, V. J. Cerebral Metabolic Rate of Oxygen (CMRO2) Assessed by Combined Doppler and Spectroscopic OCT. *Bio-medical Optics Express* **6**, 3941–3951. ISSN: 2156-7085 (11th Sept. 2015).
7. Jordan, J. E., Pelc, N. J. & Enzmann, D. R. Velocity and Flow Quantitation in the Superior Sagittal Sinus with Ungated and Cine (Gated) Phase-Contrast MR Imaging. *Journal of Magnetic Resonance Imaging* **4**, 25–28. ISSN: 1522-2586 (1st Jan. 1994).
8. Miao, G. *et al.* Reference Value of Presenile Human Hematocrit and Geographical Factors. *Journal of Clinical Laboratory Analysis* **16**, 26–29. ISSN: 1098-2825 (1st Jan. 2002).
9. Gardener, A. G., Francis, S. T., Prior, M., Peters, A. & Gowland, P. A. Dependence of Blood R2 Relaxivity on CPMG Echo-Spacing at 2.35 and 7 T. *Magnetic Resonance in Medicine* **64**, 967–974. ISSN: 1522-2594 (1st Oct. 2010).
10. Shimada, K., Nagasaka, T., Shidahara, M., Machida, Y. & Tamura, H. In Vivo Measurement of Longitudinal Relaxation Time of Human Blood by Inversion-Recovery Fast Gradient-Echo MR Imaging at 3T. *Magnetic resonance in medical sciences: MRMS: an official journal of Japan Society of Magnetic Resonance in Medicine* **11**, 265–271. ISSN: 1880-2206 (2012).

4.6. References

11. Nagdyman, N. *et al.* Comparison between Cerebral Tissue Oxygenation Index Measured by Near-Infrared Spectroscopy and Venous Jugular Bulb Saturation in Children. *Intensive Care Medicine* **31**, 846–850. ISSN: 0342-4642, 1432-1238 (1st June 2005).
12. Lu, H. & Ge, Y. Quantitative Evaluation of Oxygenation in Venous Vessels Using T2-Relaxation-Under-Spin-Tagging MRI. *Magnetic Resonance in Medicine* **60**, 357–363. ISSN: 1522-2594 (1st Aug. 2008).
13. Xu, F., Uh, J., Liu, P. & Lu, H. On Improving the Speed and Reliability of T2-Relaxation-Under-Spin-Tagging (TRUST) MRI. *Magnetic Resonance in Medicine* **68**, 198–204. ISSN: 0740-3194 (July 2012).
14. Liu, P., Xu, F. & Lu, H. Test–Retest Reproducibility of a Rapid Method to Measure Brain Oxygen Metabolism. *Magnetic Resonance in Medicine* **69**, 675–681. ISSN: 1522-2594 (1st Mar. 2013).
15. Liu, P. *et al.* Multi-Site Evaluations of a T2-Relaxation-Under-Spin-Tagging (TRUST) MRI Technique to Measure Brain Oxygenation. *Magnetic resonance in medicine* **75**, 680–687. ISSN: 0740-3194 (Feb. 2016).
16. Jain, V., Langham, M. C. & Wehrli, F. W. MRI Estimation of Global Brain Oxygen Consumption Rate. *Journal of Cerebral Blood Flow & Metabolism* **30**, 1598–1607. ISSN: 0271-678X (1st Sept. 2010).
17. Jain, V. *et al.* Cerebral Oxygen Metabolism in Neonates with Congenital Heart Disease Quantified by MRI and Optics. *Journal of Cerebral Blood Flow & Metabolism* **34**, 380–388. ISSN: 0271-678X (1st Mar. 2014).
18. Driver, I. D. *et al.* Global Intravascular and Local Hyperoxia Contrast Phase-Based Blood Oxygenation Measurements. *NeuroImage* **101**, 458–465. ISSN: 1053-8119 (1st Nov. 2014).
19. Lee, H., Langham, M. C., Rodriguez-Soto, A. E. & Wehrli, F. W. Multiplexed MRI Methods for Rapid Estimation of Global Cerebral Metabolic Rate of Oxygen Consumption. *NeuroImage* **149**, 393–403. ISSN: 1053-8119 (1st Apr. 2017).
20. Wright, G. A., Hu, B. S. & Macovski, A. Estimating Oxygen Saturation of Blood in Vivo with MR Imaging at 1.5 T. *Journal of Magnetic Resonance Imaging* **1**, 275–283. ISSN: 1522-2586 (1st May 1991).
21. Haacke, E. M. *et al.* In Vivo Measurement of Blood Oxygen Saturation Using Magnetic Resonance Imaging: A Direct Validation of the Blood Oxygen Level-Dependent Concept in Functional Brain Imaging. *Human Brain Mapping* **5**, 341–346. ISSN: 1097-0193 (1st Jan. 1997).

4.6. References

22. Spees, W. M., Yablonskiy, D. A., Oswood, M. C. & Ackerman, J. J. Water Proton MR Properties of Human Blood at 1.5 Tesla: Magnetic Susceptibility, T1, T2, T*2, and Non-Lorentzian Signal Behavior. *Magnetic Resonance in Medicine* **45**, 533–542. ISSN: 1522-2594 (1st Apr. 2001).
23. Jain, V., Abdulmalik, O., Propert, K. J. & Wehrli, F. W. Investigating the Magnetic Susceptibility Properties of Fresh Human Blood for Noninvasive Oxygen Saturation Quantification. *Magnetic Resonance in Medicine* **68**, 863–867. ISSN: 1522-2594 (1st Sept. 2012).
24. Jenkinson, M. Fast, Automated, N-Dimensional Phase-Unwrapping Algorithm. *Magnetic Resonance in Medicine* **49**, 193–197. ISSN: 1522-2594 (1st Jan. 2003).
25. Hendrikse, J., Lu, H., van der Grond, J., van Zijl, P. C. & Golay, X. Measurements of Cerebral Perfusion and Arterial Hemodynamics during Visual Stimulation Using TURBO-TILT. *Magnetic Resonance in Medicine* **50**, 429–433. ISSN: 1522-2594 (1st Aug. 2003).
26. Golay, X., Petersen, E. T. & Hui, F. Pulsed Star Labeling of Arterial Regions (PULSAR): A Robust Regional Perfusion Technique for High Field Imaging. *Magnetic Resonance in Medicine* **53**, 15–21. ISSN: 1522-2594 (1st Jan. 2005).
27. Golay, X., Stuber, M., Pruessmann, K. P., Meier, D. & Boesiger, P. Transfer Insensitive Labeling Technique (TILT): Application to Multislice Functional Perfusion Imaging. *Journal of Magnetic Resonance Imaging* **9**, 454–461. ISSN: 1522-2586 (1st Mar. 1999).
28. Lu, H., Clingman, C., Golay, X. & van Zijl, P. C. Determining the Longitudinal Relaxation Time (T1) of Blood at 3.0 Tesla. *Magnetic Resonance in Medicine* **52**, 679–682. ISSN: 1522-2594 (1st Sept. 2004).
29. Silvennoinen, M., Clingman, C., Golay, X., Kauppinen, R. & van Zijl, P. Comparison of the Dependence of Blood R2 and R2* on Oxygen Saturation at 1.5 and 4.7 Tesla. *Magnetic Resonance in Medicine* **49**, 47–60. ISSN: 1522-2594 (1st Jan. 2003).
30. Liu, P. *et al.* T1 and T2 Values of Human Neonatal Blood at 3 Tesla: Dependence on Hematocrit, Oxygenation, and Temperature. *Magnetic Resonance in Medicine* **75**, 1730–1735. ISSN: 1522-2594 (Apr. 2016).
31. Lu, H. *et al.* Calibration and Validation of TRUST MRI for the Estimation of Cerebral Blood Oxygenation. *Magnetic Resonance in Medicine* **67**, 42–49. ISSN: 1522-2594 (1st Jan. 2012).

4.6. References

32. Martirosian, P., Klose, U., Mader, I. & Schick, F. FAIR True-FISP Perfusion Imaging of the Kidneys. *Magnetic Resonance in Medicine* **51**, 353–361. issn: 1522-2594 (1st Feb. 2004).
33. Liu, P., Cox, E. & Daniel, A. *Pro TRUST* version V2018.5. 23rd Aug. 2011.
34. O'Connor, J. P. *et al.* Comparison of Normal Tissue R1 and R*2 Modulation by Oxygen and Carbogen. *Magnetic Resonance in Medicine* **61**, 75–83. issn: 1522-2594 (1st Jan. 2009).
35. Donati, O. F., Nanz, D., Serra, A. L. & Boss, A. Quantitative BOLD Response of the Renal Medulla to Hyperoxic Challenge at 1.5 T and 3.0 T. *NMR in Biomedicine* **25**, 1133–1138. issn: 1099-1492 (1st Oct. 2012).
36. Pruijm, M. *et al.* Effect of Sodium Loading/Depletion on Renal Oxygenation in Young Normotensive and Hypertensive Men. *Hypertension* **55**, 1116–1122. issn: 0194-911X, 1524-4563 (1st May 2010).
37. Tumkur, S. M., Vu, A. T., Li, L. P., Pierchala, L. & Prasad, P. V. Evaluation of Intra-Renal Oxygenation during Water Diuresis: A Time-Resolved Study Using BOLD MRI. *Kidney International* **70**, 139–143. issn: 0085-2538 (1st July 2006).
38. Prasad, P. V. & Epstein, F. H. Changes in Renal Medullary pO₂ during Water Diuresis as Evaluated by Blood Oxygenation Level-Dependent Magnetic Resonance Imaging: Effects of Aging and Cyclooxygenase Inhibition. *Kidney International* **55**, 294–298. issn: 0085-2538 (1st Jan. 1999).
39. Nielsen, K., Rehling, M. & Henriksen, J. H. Renal Vein Oxygen Saturation in Renal Artery Stenosis. *Clinical Physiology* **12**, 179–184. issn: 1365-2281 (1st Mar. 1992).

Chapter 5

Automated Segmentation of Kidneys using Machine Learning

Abstract

Total Kidney Volume (TKV) is an important measure in renal disease detection and monitoring. We developed a fully automated method to segment the kidneys from T_2 -weighted Magnetic Resonance Imaging (MRI) to calculate TKV of Healthy Control (HC) and Chronic Kidney Disease (CKD) patients.

This automated method uses machine learning, specifically a 2D Convolutional Neural Network (CNN), to accurately segment the left and right kidneys from T_2 -weighted MRI data. The dataset consisted of 30 HC subjects and 30 CKD patients. The model was trained on 50 manually defined HC and CKD kidney segmentations. The model was subsequently evaluated on 50 test data sets, comprising data from five HCs and five CKD patients each scanned five times in a scan session to enable comparison of the precision of the CNN and manual segmentation of kidneys.

The unseen test data processed by the 2D CNN had a mean Dice score of 0.93 ± 0.01 . The difference between manual and automatically computed TKV was $1.2 \pm 16.2 \text{ ml}$ with a mean surface distance of $0.65 \pm 0.21 \text{ mm}$. The variance in TKV measurements from repeat acquisitions on the same subject was significantly lower using the automated method compared to manual segmentation of the kidneys.

The 2D CNN method provides fully automated segmentation of the left and right kidney and calculation of TKV in under ten seconds on a standard office computer,

allowing high data throughput and is a freely available executable.

This work was presented as an aural presentation at the International Society of Magnetic Resonance in Medicine (ISMRM) 28th Annual Meeting (2020) [1].

5.1 Introduction

Segmentation of the kidneys from Magnetic Resonance Imaging (MRI) is a time consuming aspect of many renal MRI studies [2–4]. Total Kidney Volume (TKV) gives insight into renal function and is therefore used as a measured parameter for a variety of renal pathologies. The use of TKV is an active area of ongoing research for Autosomal Dominant Polycystic Kidney Disease (ADPKD), which is characterised by an increase in TKV due to cyst formation. Disease progression can be monitored by recording TKV, with higher rates of TKV increase being associated with a more rapid decrease in renal function [5–7]. Measurements of TKV in Chronic Kidney Disease (CKD) subjects have shown a significant correlation with glomerular filtration rate [8], the primary measure of CKD severity [9], with more generally a decrease in TKV associated with a decrease in renal function [10]. When studying pathologies which commonly lead to a change in kidney function, total kidney perfusion is often measured, this metric relies on an accurate measurement of renal blood flow and kidney volume of each kidney, and allows investigators to ascertain if the blood flow is preserved as the organ changes in size or if tissue perfusion is impaired. In addition to TKV measurements, renal segmentation is an important first step for many other processing pipelines, be that for automated cortical-medullary segmentations or to carry out multiparametric mapping within only the kidney to reduce computation times.

The gold standards of kidney segmentation are manual Region Of Interest (ROI) boundary tracing [11] or stereology [12] by experienced and skilled experts, with blood vessels in the kidney and the hilum excluded. These manual processes are highly time consuming (taking approximately 15 – 30 minutes per subject [13–15] and can be biased by investigator judgement due to the similar signal intensities between the kidneys and surrounding organs, anatomical differences between subjects, cysts and image artefacts. Consequently, the resulting kidney ROIs produced are subject to intra- and inter-expert variability as a result of the varying expertise levels; experts may segment a specific image differently when performed more than once, or different experts may segment the same image differently. These factors mean that the development of a faster and ideally fully automated method of renal segmentation is highly desirable. However the same factors that make manual segmentation difficult can also limit fully automated methods, for example the signal intensity of the kidneys closely matches that of other abdominal structures such as the spleen.

A number of automated methods have been proposed with varied success [13]. Some simply assume the kidney is an ellipse and calculate the volume from measurements of the pole-to-pole distance [16, 17] or include a correction factor to reduce overestimations [18]. Unfortunately these techniques produce a large confidence interval and still require human intervention to define the pole-to-pole length, a process that can produce inconsistencies between readers and takes a reasonable amount of time (≈ 5 min) [19]. Other semi-automated methods use classical image processing techniques such as thresholding [20], water-shedding [21], level sets [15, 22], and spatial prior probability mapping [23]. These methods can either be inaccurate, over-segmenting the kidneys, or include a number of parameters that need to be manually adjusted and are computationally intensive. Further, the fact that each technique is highly optimised for a specific dataset means that it needs to be re-written to be applied to different pathology, another time consuming and highly skilled process.

Machine learning methods have the potential to automatically detect different patterns from data given to a model which has been trained. Deep learning is a class of machine learning algorithms that can model high-level information in an image using several processing layers of transformations. This uses an architecture of multi-level linear and non-linear operations, described by layers, to learn complex functions that can represent high-level detail to map the input data to the output segmentations directly. As more data becomes available the algorithm can become more accurate and generalised, without a need to rewrite the underlying methods, thus making it a good choice for long term development.

In recent years, deep learning-based methods have been applied to the segmentation of medical images, especially successful has been the U-Net [24]. This modified fully Convolutional Neural Network (CNN) architecture uses a number of convolution, pooling and up-sampling layers to detect features in the input data at multiple resolutions. The convolution layers convolve a learnable kernel with the input data to generate spatial feature maps that are passed to subsequent layers in the network. By adjusting the kernels, the resulting feature maps can be optimised to detect the location of the kidneys. Pooling layers are used to down-sample the data and allow some convolution kernels to become tuned to approximate features, this also reduces the tendency of the network to overfit the training data. When the data has been fully down-sampled, up-sampling layers are used to increase the resolution of the feature maps back to that of the original data while more convolution layers also learn the precise location of the kidneys. Parameters are adjusted

5.1. Introduction

by comparing the output from the network to a known ground truth. CNN methods have been applied to segmentation in other areas of medical imaging [25–28], for example to prostate segmentation of MRI images [29], liver segmentation of x-ray Computed Tomography (CT) images [30] and segmentation of polycystic kidneys [31–33]. However, to date, these methods have not been successfully applied to CKD and healthy kidney segmentation from MR images.

Here a single 2D U-Net model CNN is used for the segmentation of the kidneys in both Healthy Control (HC) participants and CKD patients using T_2 -weighted MR images. Automatically generated kidney masks are compared with manual masks defined by experts and assessed for similarity using multiple voxel and surface based metrics and total segmented volume. A subset of subjects were scanned multiple times to assess the repeatability of the segmentations.

5.2 Neural Networks for Image Segmentation

5.2.1 Artificial Neural Networks

Artificial Neural Networks (ANNs) aim to solve computational problems using a similar methodology to their biological namesake. Input data is passed through a series of connected nodes or neurons, each of which can have multiple input and output connections from and to other neurons mimicking synapses. At each neuron, a weighted sum of the input values is calculated before being passed onto the next hidden layer of neurons. The final layer of neurons is connected to the output layer which will give an estimation of the desired property, be that a number e.g. probability someone will like a television program, an image e.g. the probability that a pixel in an image is a cat, or a sample in an audio signal e.g. voice synthesis. More concisely, an ANN can be used to map a non-linear set of input data to an output dimension.

A very basic example could use the mass and colour of an animal to guess if it is a dog or a cat, Figure 5.1. The connections between neurons are initialised with random weights.

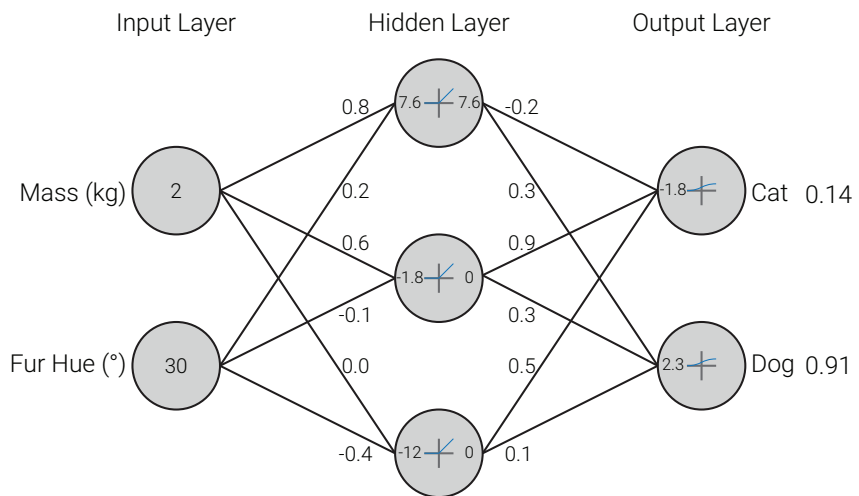


Figure 5.1: The ANN initialised with random numbers trying to predict the species of a small ginger cat.

At each neuron, a weighted sum of its inputs is taken, then an activation function applied, here a Rectified Linear Unit (ReLU), Figure 5.2a, for the hidden neurons and sig-

moid, 5.2b, for the output neurons. These activation functions allow the network to act non-linearly and are modelling the action potential of biological neurons. The ReLU function represents a higher rate of firing for signals above zero; as it is impossible for a biological neuron to reduce its firing rate below zero, the ReLU outputs zero when the input signal is less than zero. The sigmoid function maps all values between zero and one, and therefore means the network outputs a probability at the output nodes.

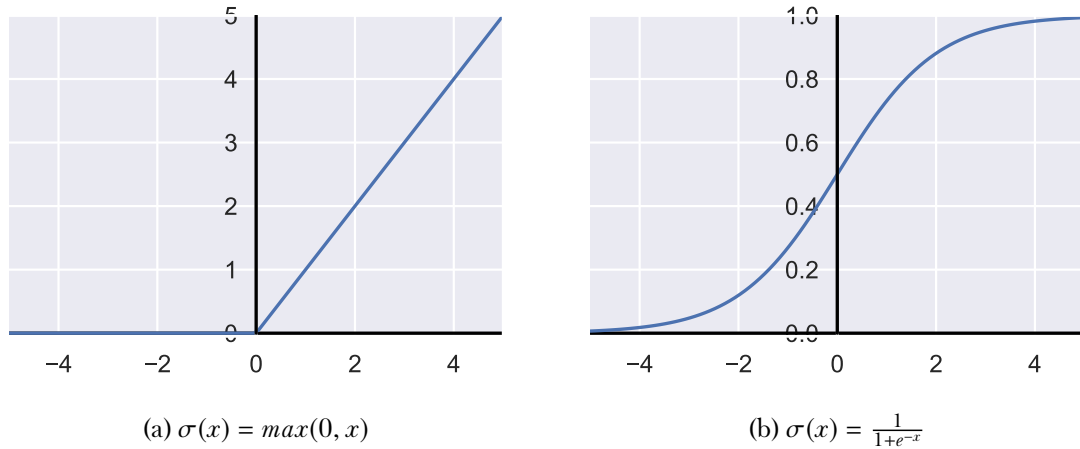


Figure 5.2: Activation functions.

As the weights were randomly initialised, the network has incorrectly predicted that the animal is a dog. By comparing the result output from the network to the known ground truth, the weights of the network can be adjusted in a process known as back propagation, Figure 5.3. Hyper-parameters such as learning rate and momentum control how much each weight is adjusted in response to the input data and subsequent result.

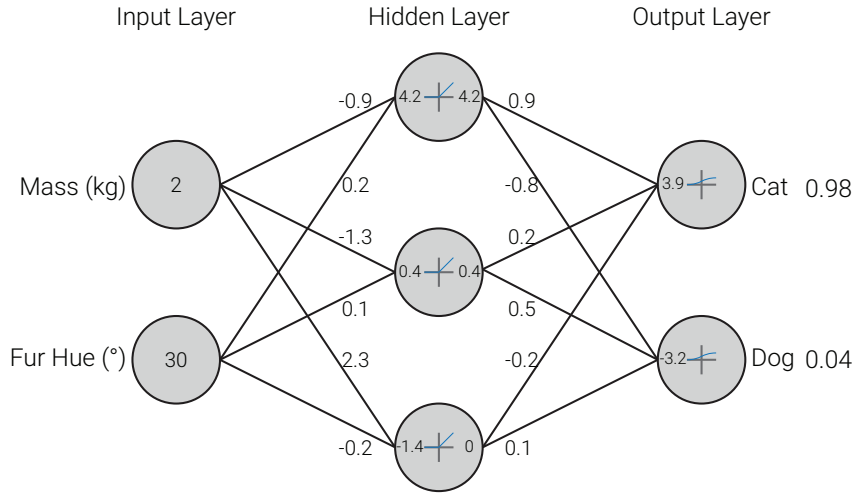


Figure 5.3: The weightings of each connection are adjusted so the output layer produces results closer to the ground truth.

When another animal is input to the network, here a smaller, darker coloured cat, the network now correctly predicts that it is a cat, 5.4. By repeating this procedure many times, comparing the result to ground truths and adjusting the weights, a process known as training, the network becomes more and more accurate. Once trained, the network can be used to infer the species of animals with no ground truth data.

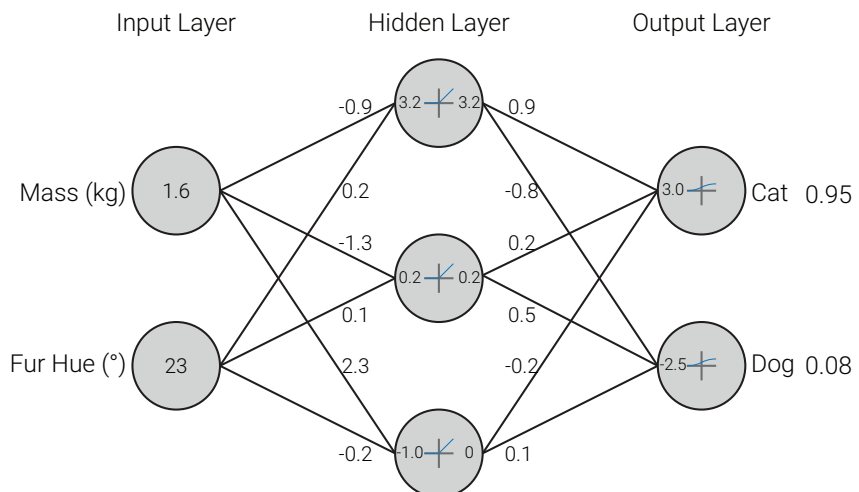


Figure 5.4: New data is presented to the network in the form of a smaller, darker coloured cat and the process of adjusting weights is repeated until more accurate results are produced.

The above example is highly simplified, real ANNs will have many more input nodes and hidden layers. In the case of imaging data, the input layer will simply be a node for each pixel in the image.

5.2.2 Convolutional Neural Networks

It was found that ANN segmentation performance was increased if additional features were input to the network. These features could be colour rather than greyscale date, different MRI contrasts e.g. fat/water images or artificially generated features. In Figure 5.5 a selection of artificially generated features are presented, some of these highlight the kidneys from the surrounding tissue e.g. the intensity range adjustment, 5.5b, and edge detector, 5.5f while others are better at providing contrast between the cyst in the right kidney and the renal tissue e.g. the intensity inversion, 5.5c and sharpening filter, 5.5e.

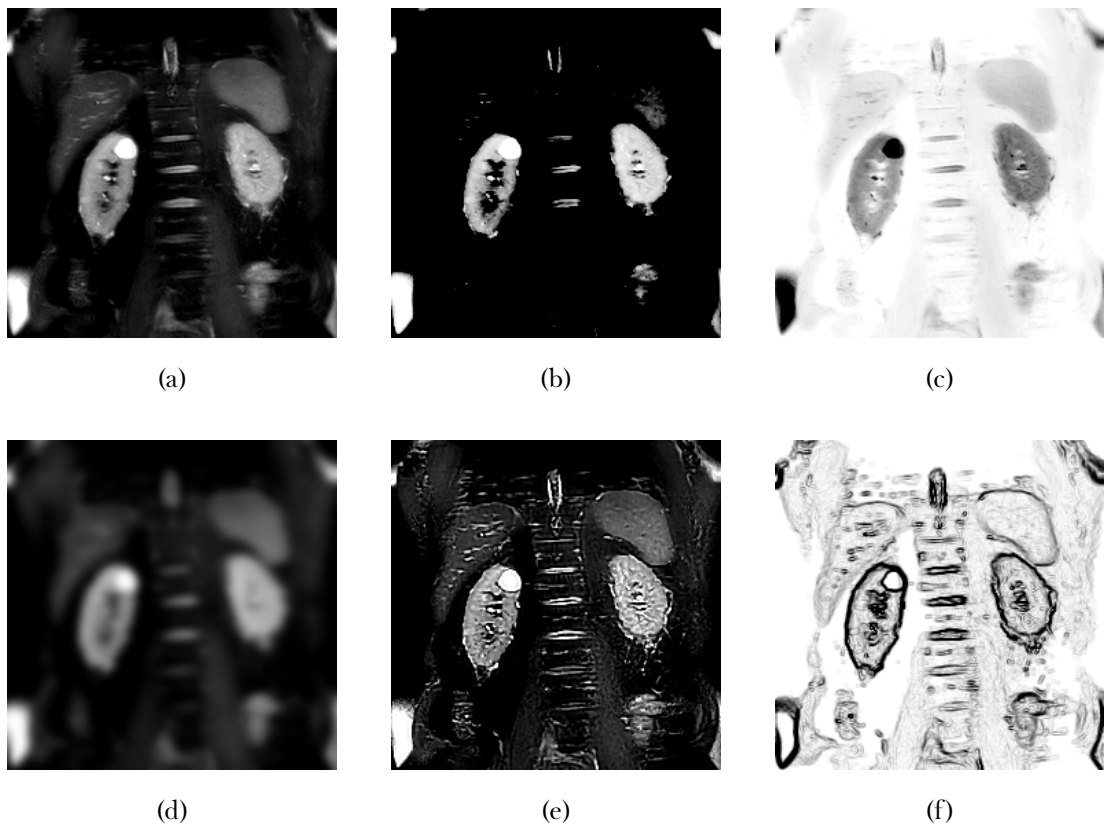


Figure 5.5: An example of the features that can be generated from a raw image (a). Implemented here are intensity range adjustments (b), intensity inversion (c), Gaussian blur (d), sharpening (e) and edge detection (f).

Many of these artificially generated features can be implemented as convolutional op-

erations, these involve convolving a numerical kernel with every pixel in the image. By adjusting the values of each cell in the kernel, different features or filters can be produced. The control of these kernels can be handed over to the same optimisation processes that are used to adjust the weights of the connections between neurons. Over the training period, this enables the network to learn what features are useful for the task at hand and which are less useful rather than the network being given features that the programmer thinks will be helpful. Shallow layers of the network usually resemble features similar to those in 5.5 while deeper layers represent more complex and specific objects such as, using the cat and dog example above, pointy noses to distinguish dogs and triangular ears to distinguish cats. This architecture is known as a Convolutional Neural Network [34, 35].

To aid with feature extraction, the raw image is often downsampled by max-pooling layers, this enables different kernels to act on different scales of the image can help keep the network generalisable and avoid overfitting. The U-Net architecture [24] combines an arm with downsampling and feature extraction with an upsampling arm that returns the image to its initial dimensions making it especially useful for segmentations tasks.

5.3 Methods

The study was approved by the University of Nottingham Medical School Research Ethics Committee (H14082014 and E14032013), and East Midlands Research Ethics committee REC reference: 17/LO/2036 and 15/EM/0274.

5.3.1 MRI Data Acquisition

All kidney MRI scans were acquired on a 3T Philips Ingenia system (Philips Medical Systems, Best, The Netherlands) using a 2D T_2 -weighted Half-Fourier Single-shot Turbo spin Echo (HASTE) sequence optimised to achieve the maximum contrast between the kidneys and surrounding tissue (Echo Time (TE) = 60 ms, Repetition Time (TR) = 1300 – 1800 ms, Sensitivity Encoding (SENSE) factor = 2.5, refocus angle 120°, bandwidth, 792 Hz, Field Of View (FOV) = 350 x 350 mm², voxel size = 1.5 x 1.5 x 5 mm³ and a slice gap of 0.5 mm with approximately 13 coronal slices, enough to image the entire kidney [36, 37], in a single 17 - 23 s breath hold.

The dataset consisted of 60 subjects, 30 HC (10 female, 20 male) with a mean age of 26 ± 11 (19–77) years and 30 CKD patients (6 female, 24 male) with a mean age of 59 ± 14 (19–80) years and mean CKD Stage 3.5 ± 1.2 (1-5). Ten of the subjects (5 HCs and 5 CKD patients) were scanned five times in the same scan session for use as test data. In each test data scan session, subjects were repositioned between each acquisition (removed from the scanner, asked to sit up and move on the bed), additionally the scanner operator attempted to vary the acquisition geometry between each scan while still acquiring full kidney coverage. These repeated test datasets allow the consistency of the networks ability to measure TKV to be assessed.

In total, 649 2D image slices from the 50 subjects in the training data and 650 2D image slices from the 10 subjects in the test data, were collected. A summary of the data collected is provided in Table 5.1 and Figure 5.9.

5.3.2 Manual Segmentation

The manual binary mask of the kidneys of each subject were generated by one of three observers (A, B and C who had been trained on kidney segmentation and had an average of 2 years of experience), with each observer segmenting data from both the training and testing datasets. Kidney boundaries were manually traced using freely available software (MRIcron [38]) and any area of non-renal parenchyma, such as the renal hilum and cysts, were excluded from the manual definition. Binary masks of the kidney were generated, and the volume of each kidney was computed from the product of the number of voxels in each kidney mask and the voxel volume. Separate kidney volume for the left and right kidneys was determined and summed to compute TKV. All measurements were performed by observers blinded for patient number and previous TKV measurements.

For the training phase, for each subject a manual mask was used from a single observer (randomised between observer A, B, or C). For the testing phase, all five scans from a given subject were segmented by a single reader with the ten subjects being segmented by a mix of the three readers i.e. the test data comprised of subjects segmented by all readers but the repeat scans of each subject were segmented by the same reader. For four HC subjects from the test dataset, manual masks were drawn by all three observers for all five repeat acquisitions to allow assessment of inter-observer variability in the manual masks. HCs were chosen for this analysis as they healthy kidneys have a more consistent morphology and thus will give a best-case measure of observer variability and provide a comparison of the automated method to the highest standard of manual segmentation.

5.3.3 Automated Segmentation Using a CNN Architecture

Voxel intensities were normalised between 0 and 255, where 0 was set to the mean voxel intensity minus 0.5 times the standard deviation of that slice and 255 was set to the mean voxel intensity plus four times the standard deviation of the volume. This empirically derived windowing led to a clear contrast between the kidneys and surrounding tissue while negating the effects of bulk signal changes between volumes. Each dataset volume was then split into 2D coronal slices and resampled to a matrix size of 256×256 . Twenty percent of slices were reserved for validation during the network optimisation process, this validation data was used to monitor over-fitting and direct the optimisation process between

5.3. Methods

epochs. Once the data had been split into training and validation sets, the slice order was randomised within sets. Splitting the data before slice randomisation limited the possibility of slices from only one subject being split over both the training and validation datasets. During training, data augmentation was applied. At the start of each epoch, a batch of images and their corresponding masks was selected at random from the training data and a series of random shifts (up to 25 % of the image in both the horizontal and vertical direction), zooms (between 0.75 and 1.25 magnification), rotations (within a 20° range), and sheers (within a 5° range) were applied to the image/mask pair to produce different yet anatomically reasonable images. The weights of the network were then adjusted based on this augmented data before selecting a new batch of images for the next epoch. Augmenting the data reduces the tendency of a model to over-fit the training data and thus increases accuracy when the model is applied to unseen images.

The U-Net consists of two Fully Convolutional Neural Network-like structures that are cascaded in the form of an encoder-decoder (autoencoder) structure. The encoder is used for feature extraction and the decoder is used for feature mapping to the original input resolution. A summary of the network architecture is shown in Figure 5.6. The convolution layers use a set of small parameterised filters, referred to as kernels, to perform convolution operations to produce different feature maps of their input. Here each convolution and deconvolution layer uses a 3 x 3 kernel. Activation layers use a ReLU. Following convolution at each resolution, max pooling with a stride 2 is used on the encoding half of the network.

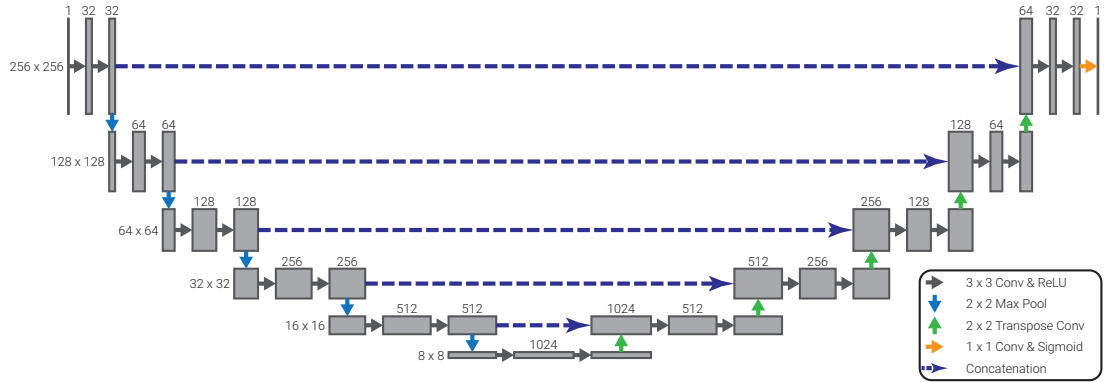


Figure 5.6: The architecture of the network used.

The network was implemented using Keras (v2.2.4) [39] with a TensorFlow backend (v1.13.1) [40] in Python 3.6.9. All training was carried out on an NVIDIA Titan Xp Graphical Processing Unit (GPU) (3840 CUDA cores, 12 GB GDDR5X). The network

5.3. Methods

uses a Dice score loss function, given by,

$$D(A, B) = \frac{2|A \cap B|}{|A| + |B|} = \frac{2TP}{2TP + FP + FN}, \quad (5.1)$$

where TP is true positive, FP is false positive and FN is false negative. A value of 1 implies complete overlap between the automated mask and the manual mask while 0 implies no overlap. This function is ideal for renal segmentation as it does not weight true negatives which represent the majority of voxels input to the network and thus means that while the network is training, it does not become trapped in a local minimum outputting solely background voxels. Training was carried out over 150 epochs using stochastic gradient descent with an initial learning rate of 0.01 and learning rate decay of 5×10^{-7} and momentum of 0.8, these parameters help the optimiser converge quickly while also avoiding overshooting. As seen in Figure 5.7, after 150 epochs the validation Dice score plateaued while the training Dice score was still rising slightly, indicating that any further training would lead to over-fitting. Training took approximately thirty minutes.

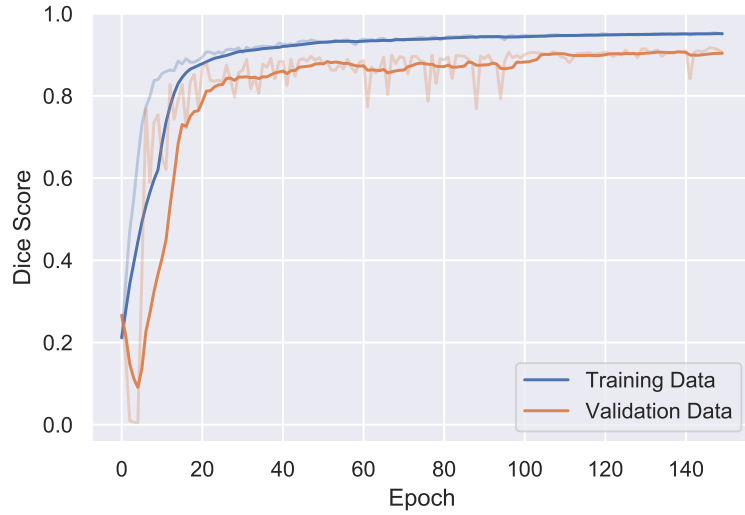


Figure 5.7: Dice score of the network for the training and validation data. Data is shown with a 10 epoch rolling average.

5.3. Methods

5.3.4 Statistical Analysis

Baseline demographics are reported as mean \pm Standard Deviation (SD). Inter-observer variability in manual segmentation and TKV was calculated by comparing the TKV of the manual masks each observer generated for a given volume, and also assessing the Bland-Altman and regression analysis. Intra-observer variability in manual segmentation was calculated by comparing the TKV of the five masks generated by an observer for a given subject. For each, the mean Coefficient of Variation (CoV); defined as standard deviation/mean and Intraclass Correlation (ICC) were used as measures of repeatability of TKV. Voxel-based metrics such as Dice score and surface based metrics such as Hausdorff Distance 95th percentile, the 95th percentile of the largest distance between the two surfaces, were also calculated between each observer.

The performance of the automated segmentation was assessed using multiple voxel and surface based similarity metrics. Performance was further assessed by determining the mean difference in TKV between the automatic and manual methods. Both actual and percentage (%) difference in TKV were evaluated. Bias (mean) obtained from the automatic and manual methods was assessed using a paired sample t-test. The mean CoV and ICC were also used as measures of repeatability of the automated TKV.

5.4 Results

5.4.1 Characteristics of the Training Cohort

Data was collected using a T_2 -weighted HASTE sequence providing optimal contrast between the kidneys and surrounding tissue, examples shown in Figure ??, however there is limited contrast between the left kidney and spleen due to their similar T_2 -weighting. Cysts of variable size are clearly visible in the kidneys of the CKD patient.

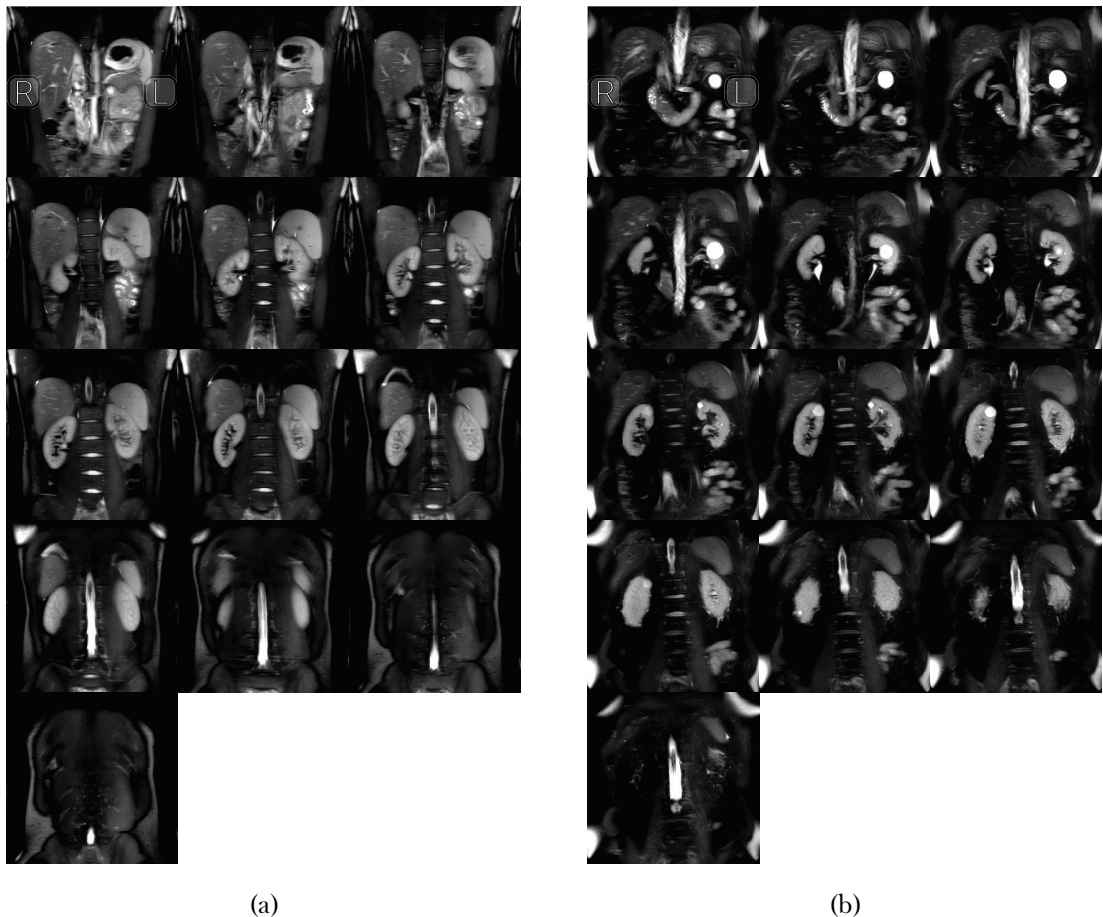


Figure 5.8: All slices of the raw data from representative subjects of the HC cohort, shown in a, and CKD cohort, b.

The training data comprised 25 healthy controls (9 female, 16 male) with a mean age of 26 ± 12 (19–77) years and 25 CKD patients (6 female, 19 male) with a mean age of 58 ± 15 (19–80) years and mean CKD stage 3.3 ± 1.1 (1–5). The manual TKV was 277 ± 60 mℓ, ranging between 145 and 422 mℓ. Including both healthy control subjects and CKD patients meant the kidneys had variable morphology (shape, size and heterogeneous

5.4. Results

cysts) within the training dataset. Table 5.1 provides the characteristics of datasets used for training and testing of the CNN, whilst Figure 5.9 shows the distribution of TKV within the training and testing data.

	Number of Subjects	Number of Datasets	Number of 2D Slices	Sex (F/M)	Mean Age	TKV (mℓ)
Training HC	25	25	325	9/16	26 ± 12	296 ± 38
Training CKD	25	25	324	6/19	58 ± 15	258 ± 72
Testing HC	5	25	325	1/4	25 ± 3	330 ± 35
Training CKD	5	25	325	0/5	69 ± 3	274 ± 56

Table 5.1: Characteristics of datasets used for training and validation of the 2D U-Net model CNN.

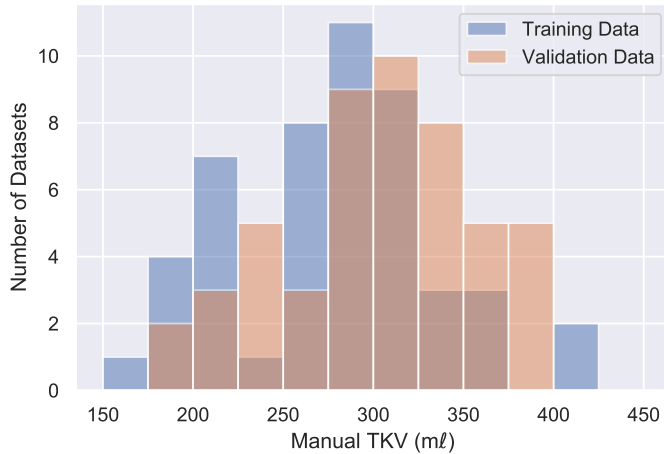


Figure 5.9: Distribution of TKV within the training and testing data.

5.4.2 Reducing Acquisition Time

Initial data was collected with a TR of 1800 ms leading to a breath hold of approximately 28 seconds. Some subjects struggled to hold their breath for this long on expiration, therefore the effects of reducing the TR of the sequence were investigated. As can be seen in Figure 5.10, there is no degradation in image quality from the image with TR of 1800 ms to that with at TR of 1300 ms, the differences between these images are mainly due to the small movements between volumes, as can be seen in the difference data where the largest

5.4. Results

differences are seen around the periphery of the kidneys and in the gut. Moving forward, the TR was reduced to 1300 ms leading to a sequence with a breath hold of approximately 17 seconds.

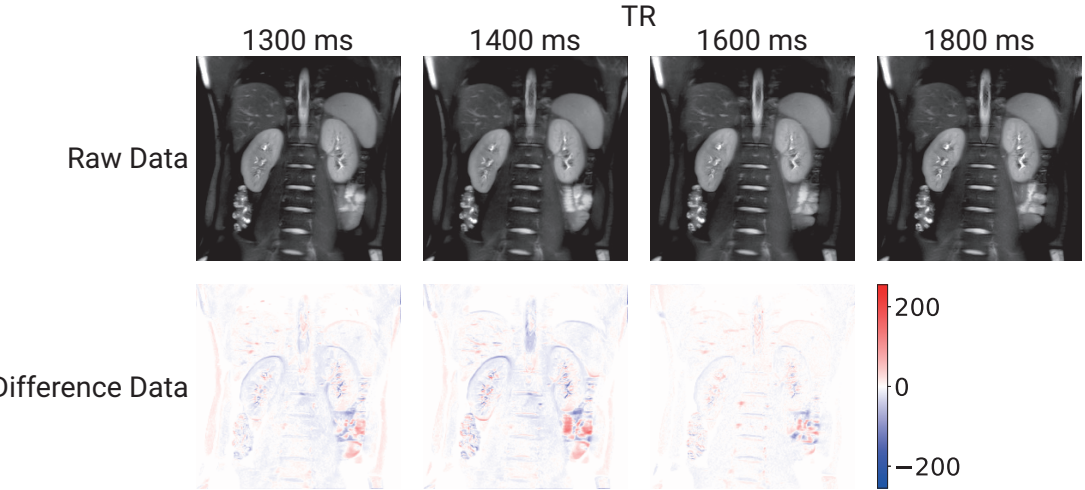


Figure 5.10: The effects of changing the TR of the sequence.

5.4.3 Accuracy of Manual Segmentation

Four of the test subjects were each scanned five times, with the left and right kidneys in the 20 datasets each masked by Observers A, B and C. The intra-observer and inter-observer variability for this manual segmentation was computed, as shown in Table 5.2.

Observer	Kidneys	CoV (%)	ICC
Intra A	Total	2.2 ± 0.7	0.939
	Left	3.2 ± 0.8	0.783
	Right	1.9 ± 0.5	0.957
Intra B	Total	1.9 ± 0.3	0.895
	Left	2.0 ± 0.5	0.807
	Right	2.4 ± 0.3	0.892
Intra C	Total	2.5 ± 0.9	0.908
	Left	2.8 ± 1.3	0.769
	Right	3.1 ± 1.9	0.940
Inter	Total	3.0 ± 1.0	0.897
	Left	4.0 ± 1.4	0.713
	Right	2.9 ± 1.0	0.910

Table 5.2: Repeatability of the manual segmentation for left, right and TKV, with coefficient of variation and intraclass coefficient computed.

Additionally, similarity metrics were used to assess the overlap between each observer's

5.4. Results

manual masks, Table 5.3. Due to the large difference between in-plane and out-of-plane resolution (1.5 mm^3 vs 5.5 mm^3) the Hausdorff distance is very susceptible to inaccuracies in the anterior – posterior direction; this metric is highly sensitive to noise and as such the 95th percentile is used to generate a more representative value. Bland-Altman plots and regression analysis of inter-observer variance in measured TKV are provided in Figure 5.11.

Observer	Kidney	Dice Score	Jaccard Index	Average Distance (mm)	Hausdorff Distance (mm) (95th Percentile)	Volume Difference (ml)
A – B	Both	0.93 ± 0.03	0.87 ± 0.05	0.81 ± 0.58	5.59 ± 2.77	20.84 ± 9.33
	Left	0.92 ± 0.07	0.85 ± 0.10	0.94 ± 1.12	5.53 ± 3.65	13.36 ± 5.76
	Right	0.94 ± 0.01	0.88 ± 0.02	0.65 ± 0.14	4.75 ± 1.15	7.48 ± 5.63
A – C	Both	0.93 ± 0.01	0.87 ± 0.02	0.79 ± 0.18	5.83 ± 1.86	16.01 ± 8.56
	Left	0.93 ± 0.01	0.87 ± 0.02	0.84 ± 0.27	6.83 ± 3.12	6.93 ± 5.78
	Right	0.93 ± 0.01	0.87 ± 0.02	0.72 ± 0.17	4.82 ± 1.25	9.08 ± 5.41
B – C	Both	0.94 ± 0.04	0.89 ± 0.06	0.63 ± 0.62	3.59 ± 2.74	-4.83 ± 9.92
	Left	0.93 ± 0.08	0.88 ± 0.11	0.78 ± 1.22	4.31 ± 3.58	-6.44 ± 6.17
	Right	0.95 ± 0.01	0.90 ± 0.02	0.48 ± 0.14	3.39 ± 1.15	1.61 ± 6.56

Table 5.3: Metrics comparing each combination of observers manual masks (A – B, A – C and B – C). All values are quoted as mean \pm standard deviation.

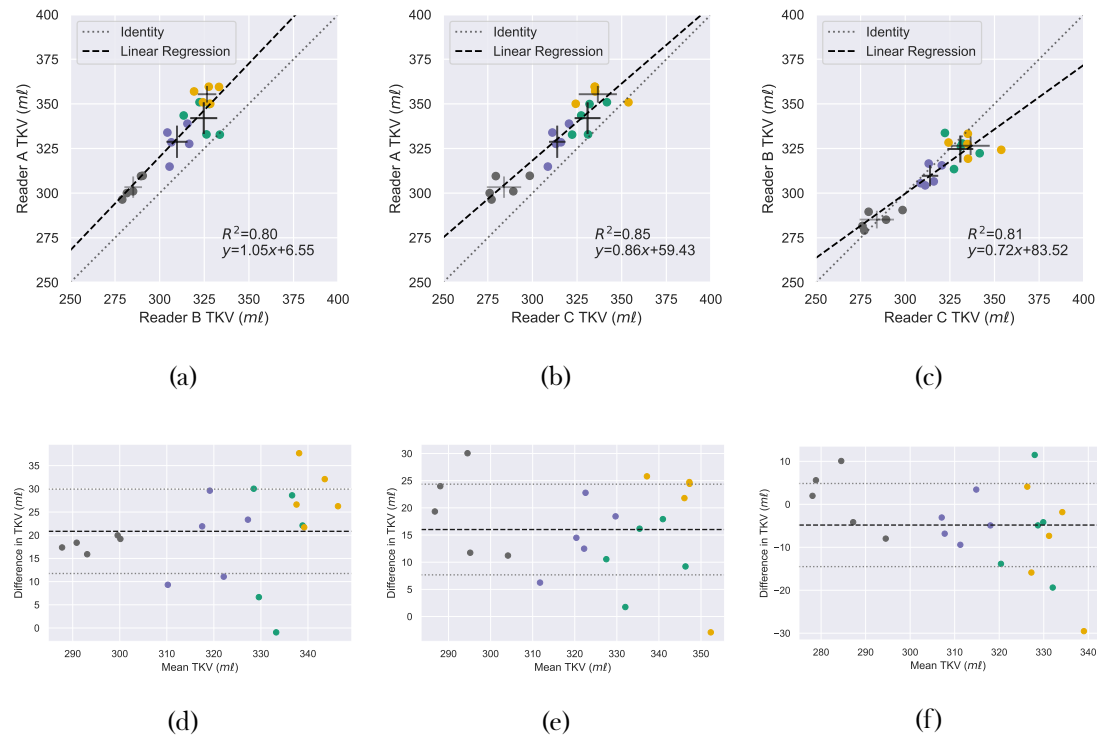


Figure 5.11

5.4.4 Network Testing

To verify that the trained network is behaving as expected saliency maps were produced, Figure 5.12, this is especially important given the black box nature of machine learning methods. This map shows the areas the network is using most in its classification [41]. It verifies that the networks is using the outside areas of the kidney to make its prediction with areas of a similar intensity receiving some attention to distinguish them from the kidney. While this is precisely what is expected of the algorithm, it is important to check this as it is possible for such a method to have learnt a slightly different mechanism for the segmentation, one that is more prone to errors if new data is presented to it.

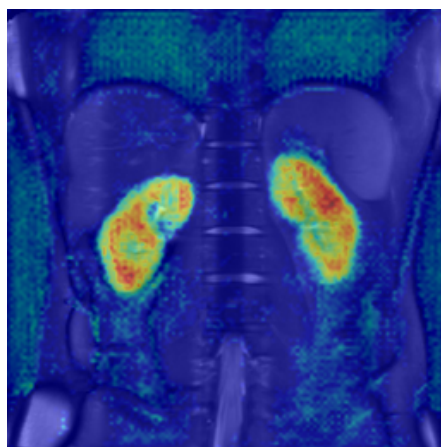


Figure 5.12: An example saliency map of the areas the network uses most when segmenting the kidney.

The trained network was used to predict segmentations of the 2D kidney slices and compute TKV for each of the unseen test volumes. The mean Dice score over the 50 test volumes was 0.93 ± 0.01 (0.94 ± 0.02 for HC and 0.92 ± 0.01 for CKD patients). The TKV predicted by the network was, on average, 1.2 ± 16.2 mℓ less than the manually segmented TKV and thus not significantly different ($p = 0.615$) (Figure 5.13) This accuracy was comparable for the HC and CKD cohorts, with automated CNN TKV measurements of 4.7 ± 17.7 mℓ greater than manual and 7.0 ± 12.4 mℓ less than manual respectively. A summary of the CNN accuracy when evaluated using similarity metrics and volume difference from manual measures is shown in Table 5.4. Note a slightly larger discrepancy for the left compared to the right kidney. Figure 5.13 shows plots of the difference in volume between manual segmentation and automated segmentation of the test dataset.

5.4. Results

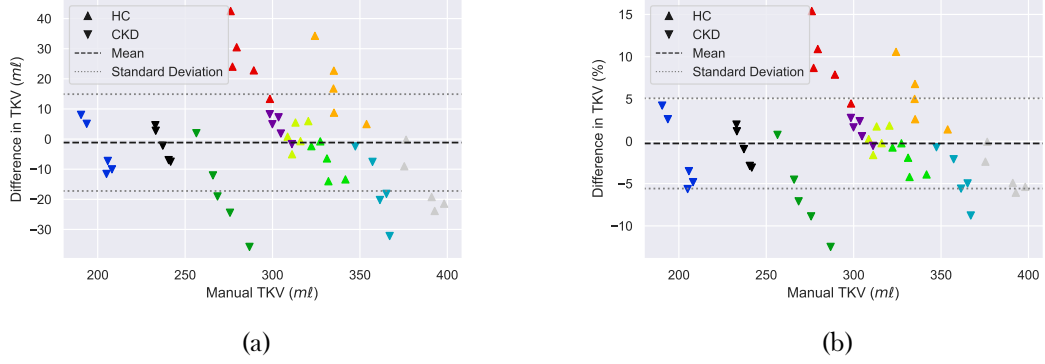


Figure 5.13: The difference between the TKV predicted by the CNN and the manually segmented true TKV. Mean and standard deviation TKV difference are shown as dashed and dotted lines respectively. Each subject is shown in a different colour. (a) shows the absolute volume difference (b) shows the percentage volume difference.

Cohort	Kidney	Dice Score	Jaccard Index	Sensitivity	Specificity	Precision	Accuracy	Mean Surface Distance (mm)	Hausdorff Distance (mm) (95th Percentile)	Volume Difference (p)
All	Total	0.93 ± 0.01	0.87 ± 0.03	0.93 ± 0.03	0.997 ± 0.001	0.93 ± 0.02	0.995 ± 0.001	0.65 ± 0.21	4.33 ± 1.64	-1.16 ± 16.23 (0.615)
	Left	0.92 ± 0.02	0.86 ± 0.04	0.91 ± 0.05	0.997 ± 0.001	0.94 ± 0.03	0.994 ± 0.002	0.76 ± 0.31	4.42 ± 1.52	-3.95 ± 12.38 (0.029)
	Right	0.94 ± 0.02	0.89 ± 0.03	0.95 ± 0.03	0.997 ± 0.001	0.93 ± 0.03	0.996 ± 0.001	0.54 ± 0.21	3.66 ± 1.76	2.79 ± 6.84 (0.006)
HC	Total	0.94 ± 0.02	0.88 ± 0.03	0.95 ± 0.05	0.997 ± 0.001	0.93 ± 0.03	0.995 ± 0.001	0.68 ± 0.27	4.50 ± 1.97	4.66 ± 17.72 (0.201)
	Left	0.93 ± 0.02	0.87 ± 0.04	0.94 ± 0.05	0.997 ± 0.001	0.93 ± 0.03	0.994 ± 0.002	0.79 ± 0.37	4.47 ± 1.81	1.91 ± 12.93 (0.467)
	Right	0.95 ± 0.02	0.90 ± 0.03	0.96 ± 0.03	0.997 ± 0.001	0.94 ± 0.02	0.996 ± 0.001	0.56 ± 0.26	3.81 ± 2.11	2.75 ± 7.70 (0.087)
CKD	Total	0.92 ± 0.01	0.86 ± 0.02	0.91 ± 0.02	0.998 ± 0.001	0.94 ± 0.02	0.995 ± 0.001	0.63 ± 0.14	4.16 ± 1.24	-6.98 ± 12.38 (0.009)
	Left	0.92 ± 0.02	0.85 ± 0.03	0.89 ± 0.04	0.998 ± 0.001	0.95 ± 0.02	0.994 ± 0.002	0.73 ± 0.24	4.37 ± 1.21	-9.81 ± 8.62 (0.00001)
	Right	0.93 ± 0.01	0.88 ± 0.02	0.94 ± 0.02	0.997 ± 0.001	0.92 ± 0.03	0.996 ± 0.001	0.51 ± 0.13	3.51 ± 1.34	2.83 ± 6.02 (0.027)

Table 5.4: The accuracy of the CNN compared to manual segmentations using a variety of metrics stratifying the testing data by cohort and left vs right kidney. All values are given as mean ± standard deviation.

5.4. Results

In Figure 5.14, the TKV predicted by the CNN is plot against the manual TKV, in ninety percent of subjects, the standard deviation of TKV measurements between each volume for a subject was smaller when the TKV was measured using the CNN as oppose to manually. The mean CoV and ICC were $2.7 \pm 0.9\%$ and 0.979 respectively across the 5 repeats of the manually segmented test data (using masks from observers A, B and C), compared to a value of $1.5 \pm 0.5\%$ and 0.993 respectively for the automatic segmentations of the 5 repeats of test data. The CNN produced a significantly lower CoV than the manual segmentations ($p = 0.008$).

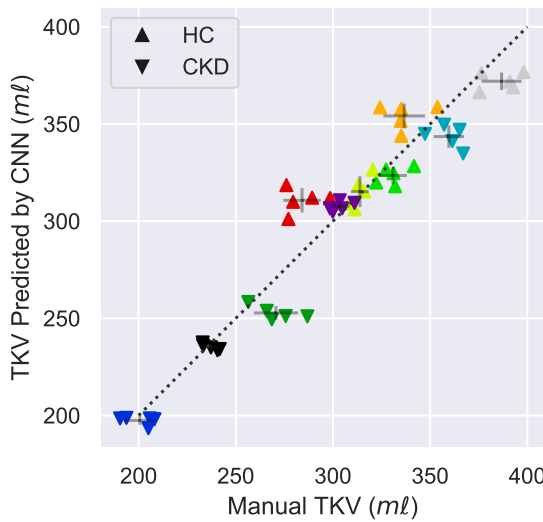


Figure 5.14: The TKV predicted by the CNN plot against the manually segmented true TKV with each subject plot in a different colour. The standard deviation measured using both methods is shown as error bars originating from the mean of each subject. The dotted line represents perfect correlation between the CNN and manual segmentation.

Representative examples of the output from the network for both HC and CKD data are shown in Figure 5.15. The automated CNN accurately segments the kidneys, and for CKD patients, often omits cysts from the masks.

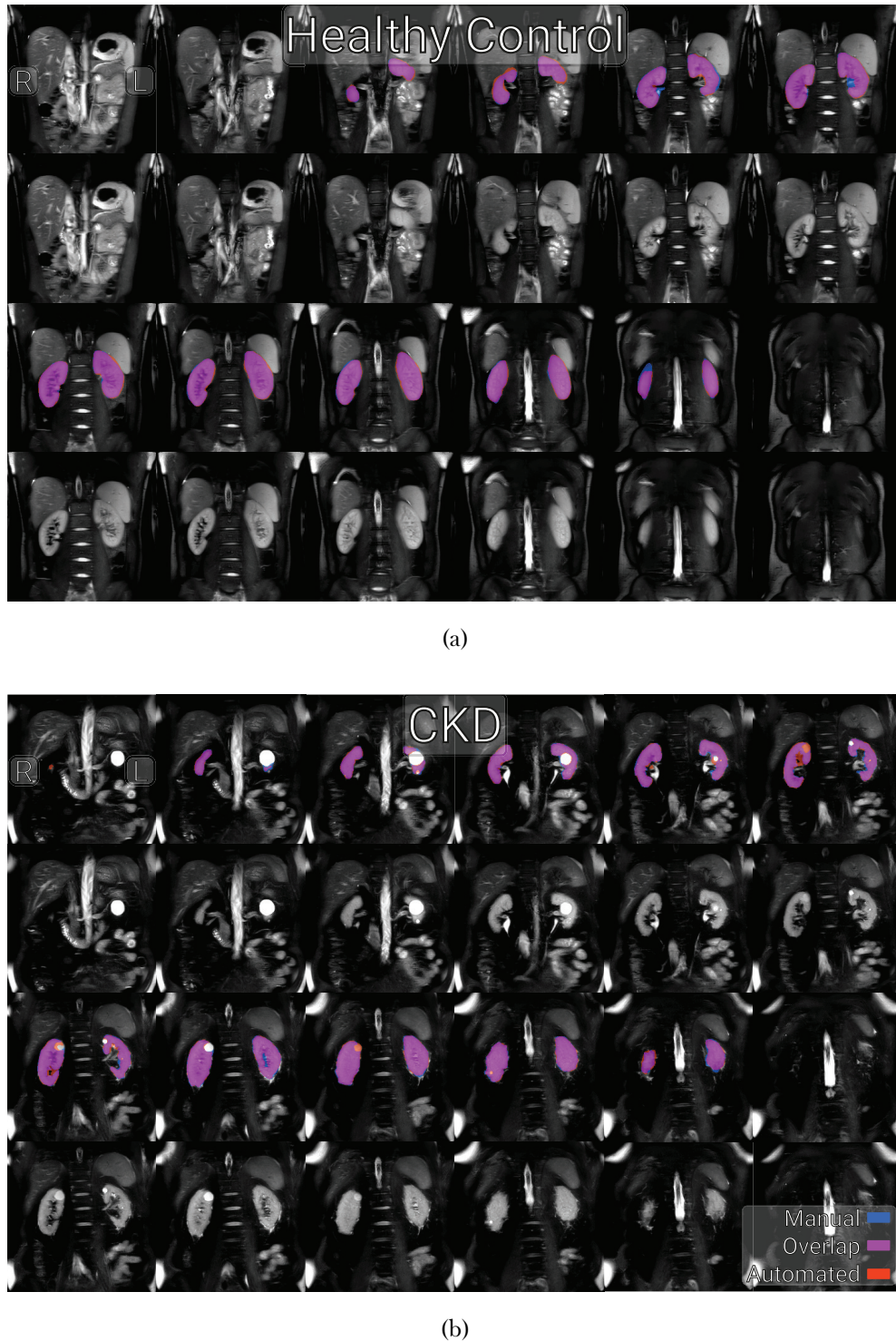


Figure 5.15: Representative raw test data and corresponding masks of a HC, (a), and CKD subject, (b). Manually generated masks are shown in blue, automatically generated masks are shown in red and the overlap of the two is shown in magenta.

Since this is a 2D CNN, it is important to assess the accuracy across the anterior – posterior 2D slices of the kidney. This was achieved by comparing the Dice score of the

5.4. Results

CNN to the inter-reader Dice scores, Figure 5.16. A decrease in accuracy in the outer slices can be seen in both the CNN and manual masks.

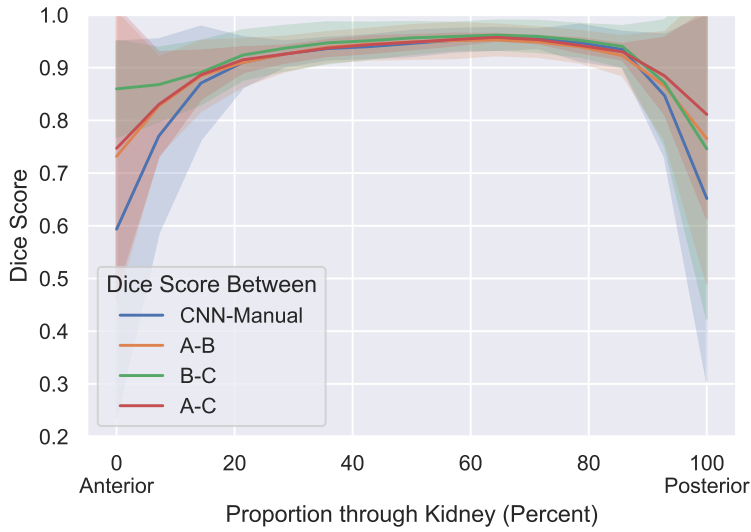


Figure 5.16: Mean Dice score for 2D slices from anterior to posterior. The shaded area represents one standard deviation from the mean Dice score.

This decrease in accuracy manifests itself on the outer slices of the volume, where the proportion of kidney per slice is smaller and as such the 2D network, with a lack of spatial context in the anterior – posterior direction, finds these outer slices more challenging. This decrease in accuracy can partly be explained by the fact that larger structures (in terms of number of voxels) will in general produce higher scores for comparable errors because the vast majority of errors are on the perimeter of the kidney in each slice, slices with fewer voxels of kidney have a smaller area to perimeter ratio, Figure 5.17.

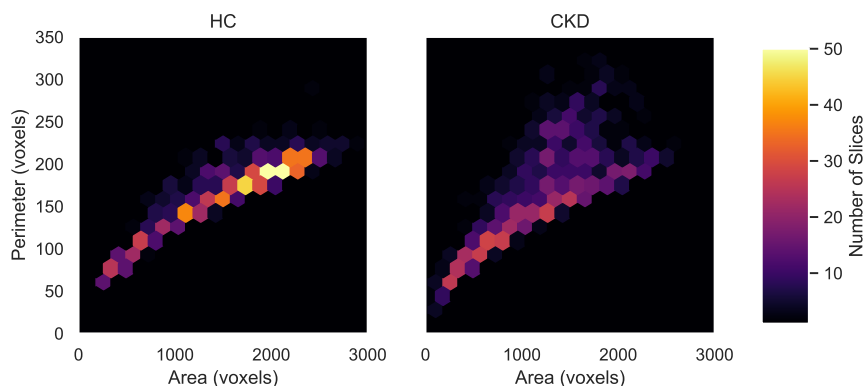


Figure 5.17: A 2D histogram of the perimeter and area of each slice for both the HC and CKD cohorts.

5.5 Discussion

In this chapter, a 2D CNN has been trained to generate automatic segmentations of healthy control and CKD patients. Segmentations of the left and right kidneys are computed from which total kidney volume is estimated. The CNN was trained on both healthy control and CKD kidneys with a range of TKV (144.76 – 422.49 m ℓ) which included the presence of cysts. The automated segmentation by the CNN yielded a mean Dice score of 0.93 ± 0.01 and took an average time of 9 s to measure TKV compared to 15 – 30 minutes [13] for manual segmentation. The automated CNN can be run as a self-contained Graphical User Interface (GUI) with the data and programme freely available [42] and thus avoid the need for complicated software setup. Note the software released at present can only be used to process coronal HASTE images and will not be accurate with other geometries/contrasts, for this, training of the network with a different dataset would be required and thus necessitate the use of a GPU.

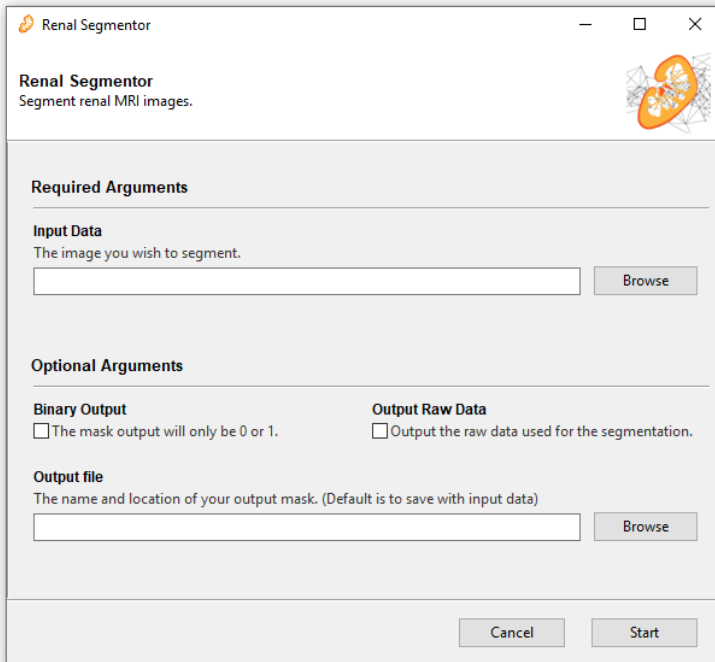


Figure 5.18: The Graphical User Interface used to segment kidneys.

5.5.1 Evaluation of Methodology

The network performed with high precision on the test data with a 1.2 ± 16.2 m ℓ , statistically insignificant, discrepancy between manual and automated TKV measurements. Table 5.4 shows the agreement between the CNN and manual masks is higher for the right than left kidney, this is in part due to the proximity and lack of contrast between the left kidney and the spleen making distinguishing this boundary difficult for the CNN. This difficulty also leads to inconsistencies in manual masks, borne out by the increased CoV and decreased ICC and similarity metrics of the left kidney when compared to the right kidney in Table 5.2 and Table 5.4 assessing the variability in manual masks between observers. From Table 5.4 it can also be seen that the agreement between the CNN and manual masks is greater for the healthy control cohort than the CKD cohort, this is expected due to the increased variation in kidney morphology and the presence of cysts in the CKD cohort. Figure 5.13 shows that the difference between the manual TKV and CNN predicted TKV is not dependent on the true TKV, therefore the training data is balanced and well augmented as the network is able to accurately perform over the full range of kidney size in the test data.

Here, five volumes of test data were collected for each subject by repositioning the subject in the scanner within an hour scan session, and therefore any variance in measured TKV is purely due to inaccuracies in the kidney ROI definition. On assessing the correlation between manual and CNN measured TKV in Figure 5.14, it can be seen that, in 90 % of subjects the intra-observer variance in manual TKV between the segmentation of the five volumes collected in each subject is larger than using the CNN to estimate TKV, as reflected by the lower CoV and increased ICC of the TKV measured using the CNN (CoV 1.5 ± 0.5 %, ICC 0.993) compared to the manual measures (CoV 2.7 ± 0.9 %, ICC 0.979). As the network is trained on the kidney segmentations from three observers (A, B and C), it has been optimised by inheriting the most accurate tendencies of each observer e.g. one observer may have been very accurate when excluding cysts but not as accurate at defining the kidney-spleen boundary. The network will have learnt to exclude cysts from this observer but to delineate between kidney and spleen from another observer. Thus the network can become more precise than each individual observers manual segmentations. This increased precision can be seen in Figure 5.13 when compared to Figure 5.14 where the variance in difference in TKV is driven by the larger variance in manual TKV. The smallest TKV per subject is consistently overestimated when compared to its manual mask

and vice versa the largest manual TKV per subject is often an underestimation compared to the manual TKV.

Figure 5.15 illustrates the masks produced by the manual segmentation and the CNN for both a HC and CKD patient. For the HC, the CNN includes more voxels around the edge of its mask than manual segmentation, and the network is more anatomically accurate e.g. where the interface between the kidney and spleen is very narrow, the CNN predicts the kidney is adjacent to the spleen whilst the observers manual segmentation leaves a gap. The CKD data shown in Figure 5.15b includes a cyst in each of the kidneys. The network was trained on a combination of healthy and CKD data, with 19 of the 25 CKD training datasets containing at least one cyst. The CNN can be seen to segment out the cysts, despite their highly variable morphology and prevalence in the overall training data.

The amount of augmentation applied to the training data was empirically derived (random shifts up to 25 % of the image in both the horizontal and vertical direction, zooms between 0.75 and 1.25 times magnification, rotations within a 20 degree range, and sheers within a 5 degree range) and led to the potential for large transforms being applied to the data and masks if the extremes of each transform were randomly selected. This large degree of augmentation was advantageous as it mirrors the large variation in acquisition planning in abdominal imaging.

A 2D CNN was used to process each 2D slice of a full volume, rather than a 3D volume. This was advantageous for the relatively small training dataset the network was optimised on, as it avoids overfitting and allows the network to easily be used on volumes of variable slice number. However, this can come at the expense of accuracy as 2D CNNs do not leverage the information from adjacent slices in the segmentation as is done in 3D CNN, but 3D CNN come with a computational cost as a result of the increased number of parameters used. 3D networks have successfully been implemented on neural data using patching methods where the image volume is divided up into smaller cubes [27] to reduce memory requirements and allow for differing input shapes. While this works well in the brain, there are a number of reasons why this method may not be as successful for body applications. The out-of-plane resolution is significantly less than the in-plane resolution; this results in far fewer slices in one direction than the other two. To avoid overfitting for a certain number of slices e.g. training on a 11 slice image with a 113 patch, and subsequently the network not performing well when the patch is applied to a 16 slice image, the patch would

need to be much smaller than the number of slices, thus diminishing the benefits of the 3D methodology. Additionally, the extra memory requirements for a 3D network limit the ease of use of the software for inference on many standard office computers.

5.5.2 Future Directions

Future work will explore alternative network architectures. As the main source of inaccuracy with the current network is its lack of slice-to-slice context, there are multiple architectures that can address this. A relatively simple method would be exploiting the fact that the Keras framework is designed to work with colour images. By combining three slices into a single image where each slice represents either the red, green or blue channel, Figure 5.19, the network would be able to use contextual information about the adjacent slices to help inform its predictions. This method result in two slices from each volume being becoming impossible to process and as such the FOV would have to be increased. Alternatively multiple network architectures such as Recursive Neural Network (RNN) [43], and Long Short-Term Memory (LSTM) [44] are designed to have a memory therefore enabling them to retain contextual information from slice to slice. Alternatively, if more training data were available, a 3D CNN could be explored to ascertain if the any improved accuracy is worth the increase in hardware requirements and reduced generalisability.

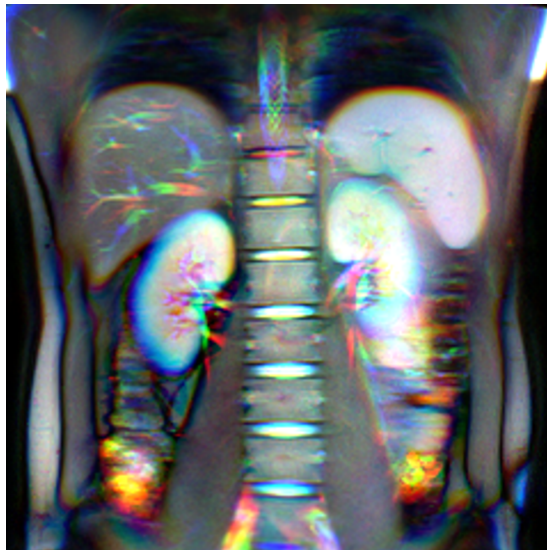


Figure 5.19: An example of using colour information to represent adjacent slices for processing by a CNN. Vessels in the liver can clearly be seen travelling through the three slices as they change from red to green to blue.

5.5. Discussion

This image contrast was chosen as a result of recent publications comparing T_1 - and T_2 -weighted images for TKV assessment reporting that T_2 -weighted images provide better quality to enable TKV measurements, leading to improved reproducibility with lower intra- and inter-reader variability [45]. Other contrasts e.g. a T_1 -weighted scan, could also be collected, registered to the T_2 -weighted images and used as another channel to inform segmentation.

This network was validated on healthy subjects and CKD patients, but has not been trained and validated on subjects with ADPKD. These subjects have many more cysts in their kidneys, while the CNN was able to segment cysts encountered in the CKD cohort, it would be beneficial for future work on ADPKD to retrain the network with HC, CKD and ADPKD data, where TKV is a recognised biomarker of disease progression.

Another common segmentation task in renal imaging is generating an ROI for the renal cortex and medulla. There are some automated methods of achieving this once a total kidney mask has been produced [2, 46], however there has been no work on the application of deep learning to this task. In addition to the acquisition of the T_2 -weighted dataset used here, a T_1 -weighted dataset designed to optimise the contrast between cortex and medulla was also collected on each subject [87], an example of which is shown in Figure 5.20. Using this data, it may be possible to develop this method further such that an automated mask for each tissue type is produced.



Figure 5.20: An example of the data collected to enable segmentation of the renal cortex and medulla.

5.6 Conclusions

A CNN has been shown to successfully segment the kidneys of both HC and CKD subjects from T_2 -weighted data delivering a mean Dice score of 0.93 ± 0.01 leading to a mean volume of $1.2 \pm 16.2 \text{ ml}$ less than the manually segmented TKV and mean surface distance of $0.65 \pm 0.21 \text{ mm}$. The CNN produces higher than human precision, with a CoV and ICC of $1.5 \pm 0.5 \%$ and 0.993 respectively. The accuracy of the network could be further increased via the acquisition of more training data, something the renal group at Sir Peter Mansfield Imaging Centre (SPMIC) are actively pursuing.

The methods developed here can easily be deployed via the self contained, easy to use GUI, thus moving renal segmentation from a 15 to 30 minute skilled task, to a 10 second task for anyone, on any hardware. Additional, this executable can be called from a terminal, making it suitable for use in scripting applications and pipelines.

Future development will focus around exploring different network architectures, use of additional contrasts and expanding the tool to produce masks of both the cortex and medulla.

5.7 Acknowledgements

We gratefully acknowledge the support of NVIDIA Corporation with the donation of the Titan Xp GPU used for this research.

5.8 References

1. Daniel, A. *et al.* Automated Renal Segmentation in Healthy and Chronic Kidney Disease Subjects Using A Convolutional Neural Network in *Proc. Intl. Soc. Mag. Reson. Med.* 28 International Society of Magnetic Resonance in Medicine Annual Meeting (Online, Aug. 2020).
2. Cox, E. F. *et al.* Multiparametric Renal Magnetic Resonance Imaging: Validation, Interventions, and Alterations in Chronic Kidney Disease. *Frontiers in Physiology* **8**. ISSN: 1664-042X (2017).
3. Cohen, E. I., Kelly, S. A., Edye, M., Mitty, H. A. & Bromberg, J. S. MRI Estimation of Total Renal Volume Demonstrates Significant Association with Healthy Donor Weight. *European Journal of Radiology. Rheumatoid Disease and Imaging* **71**, 283–287. ISSN: 0720-048X (1st Aug. 2009).
4. Van den Dool, S. W., Wasser, M. N., de Fijter, J. W., Hoekstra, J. & van der Geest, R. J. Functional Renal Volume: Quantitative Analysis at Gadolinium-Enhanced MR Angiography—Feasibility Study in Healthy Potential Kidney Donors. *Radiology* **236**, 189–195. ISSN: 0033-8419 (1st July 2005).
5. Chapman, A. B. *et al.* Kidney Volume and Functional Outcomes in Autosomal Dominant Polycystic Kidney Disease. *Clinical Journal of the American Society of Nephrology* **7**, 479–486. ISSN: 1555-9041, 1555-905X (1st Mar. 2012).
6. Tangri, N. *et al.* Total Kidney Volume as a Biomarker of Disease Progression in Autosomal Dominant Polycystic Kidney Disease. *Canadian Journal of Kidney Health and Disease* **4**, 2054358117693855. ISSN: 2054-3581 (1st Jan. 2017).
7. Grantham, J. J. *et al.* Volume Progression in Polycystic Kidney Disease. *New England Journal of Medicine* **354**, 2122–2130. ISSN: 0028-4793 (18th May 2006).
8. Buchanan, C. E. *et al.* Quantitative Assessment of Renal Structural and Functional Changes in Chronic Kidney Disease Using Multi-Parametric Magnetic Resonance Imaging. *Nephrology Dialysis Transplantation* (29th June 2019).
9. Stevens, L. A., Coresh, J., Greene, T. & Levey, A. S. Assessing Kidney Function — Measured and Estimated Glomerular Filtration Rate. *New England Journal of Medicine* **354**, 2473–2483. ISSN: 0028-4793 (8th June 2006).
10. Gong, I. H. *et al.* Relationship Among Total Kidney Volume, Renal Function and Age. *The Journal of Urology* **187**, 344–349. ISSN: 0022-5347 (Jan. 2012).
11. Di Leo, G., Di Terlizzi, F., Flor, N., Morganti, A. & Sardanelli, F. Measurement of Renal Volume Using Respiratory-Gated MRI in Subjects without Known Kidney Dis-

5.8. References

- ease: Intraobserver, Interobserver, and Interstudy Reproducibility. *European Journal of Radiology* **80**, e212–e216. issn: 0720-048X (1st Dec. 2011).
12. Bae, K. T., Commean, P. K. & Lee, J. Volumetric Measurement of Renal Cysts and Parenchyma Using MRI: Phantoms and Patients with Polycystic Kidney Disease. *Journal of Computer Assisted Tomography* **24**, 614–619. issn: 0363-8715 (July–Aug. 2000).
 13. Zöllner, F. G. *et al.* Assessment of Kidney Volumes From MRI: Acquisition and Segmentation Techniques. *American Journal of Roentgenology* **199**, 1060–1069. issn: 0361-808X (1st Nov. 2012).
 14. Sharma, K. *et al.* Kidney Volume Measurement Methods for Clinical Studies on Autosomal Dominant Polycystic Kidney Disease. *PLOS ONE* **12**, e0178488. issn: 1932-6203 (30th May 2017).
 15. Simms, R. J. *et al.* A Rapid High-Performance Semi-Automated Tool to Measure Total Kidney Volume from MRI in Autosomal Dominant Polycystic Kidney Disease. *European Radiology* **29**, 4188–4197. issn: 1432-1084 (1st Aug. 2019).
 16. Cheong, B., Muthupillai, R., Rubin, M. F. & Flamm, S. D. Normal Values for Renal Length and Volume as Measured by Magnetic Resonance Imaging. *Clinical Journal of the American Society of Nephrology* **2**, 38–45. issn: 1555-9041, 1555-905X (1st Jan. 2007).
 17. Spithoven, E. M. *et al.* Estimation of Total Kidney Volume in Autosomal Dominant Polycystic Kidney Disease. *American Journal of Kidney Diseases* **66**, 792–801. issn: 0272-6386 (1st Nov. 2015).
 18. Seuss, H. *et al.* Development and Evaluation of a Semi-Automated Segmentation Tool and a Modified Ellipsoid Formula for Volumetric Analysis of the Kidney in Non-Contrast T2-Weighted MR Images. *Journal of Digital Imaging* **30**, 244–254. issn: 1618-727X (1st Apr. 2017).
 19. Magistroni, R., Corsi, C., Martí, T. & Torra, R. A Review of the Imaging Techniques for Measuring Kidney and Cyst Volume in Establishing Autosomal Dominant Polycystic Kidney Disease Progression. *American Journal of Nephrology* **48**, 67–78. issn: 0250-8095, 1421-9670 (2018).
 20. Coulam, C. H., Bouley, D. M. & Sommer, F. G. Measurement of Renal Volumes with Contrast-Enhanced MRI. *Journal of Magnetic Resonance Imaging* **15**, 174–179. issn: 1522-2586 (2002).

5.8. References

21. Karstoft, K. *et al.* Different Strategies for MRI Measurements of Renal Cortical Volume. *Journal of Magnetic Resonance Imaging* **26**, 1564–1571. issn: 1522-2586 (2007).
22. Gloger, O. *et al.* Prior Shape Level Set Segmentation on Multistep Generated Probability Maps of MR Datasets for Fully Automatic Kidney Parenchyma Volumetry. *IEEE Transactions on Medical Imaging* **31**, 312–325. issn: 1558-254X (Feb. 2012).
23. Kim, Y. *et al.* Automated Segmentation of Kidneys from MR Images in Patients with Autosomal Dominant Polycystic Kidney Disease. *Clinical Journal of the American Society of Nephrology* **11**, 576–584. issn: 1555-9041, 1555-905X (7th Apr. 2016).
24. Ronneberger, O., Fischer, P. & Brox, T. *U-Net: Convolutional Networks for Biomedical Image Segmentation in Medical Image Computing and Computer-Assisted Intervention – MICCAI 2015* (eds Navab, N., Hornegger, J., Wells, W. M. & Frangi, A. F.) (Springer International Publishing, Cham, 2015), 234–241. isbn: 978-3-319-24574-4.
25. Lu, F., Wu, F., Hu, P., Peng, Z. & Kong, D. Automatic 3D Liver Location and Segmentation via Convolutional Neural Network and Graph Cut. *International Journal of Computer Assisted Radiology and Surgery* **12**, 171–182. issn: 1861-6429 (1st Feb. 2017).
26. Sharma, K. *et al.* Automatic Segmentation of Kidneys Using Deep Learning for Total Kidney Volume Quantification in Autosomal Dominant Polycystic Kidney Disease. *Scientific Reports* **7**, 2049. issn: 2045-2322 (1 17th May 2017).
27. Wachinger, C., Reuter, M. & Klein, T. DeepNAT: Deep Convolutional Neural Network for Segmenting Neuroanatomy. *NeuroImage. Segmenting the Brain* **170**, 434–445. issn: 1053-8119 (15th Apr. 2018).
28. Fu, Y. *et al.* A Novel MRI Segmentation Method Using CNN-Based Correction Network for MRI-Guided Adaptive Radiotherapy. *Medical Physics* **45**, 5129–5137. issn: 2473-4209 (2018).
29. Hassanzadeh, T., Hamey, L. G. C. & Ho-Shon, K. Convolutional Neural Networks for Prostate Magnetic Resonance Image Segmentation. *IEEE Access* **7**, 36748–36760. issn: 2169-3536 (2019).
30. Li, X. *et al.* H-DenseUNet: Hybrid Densely Connected UNet for Liver and Tumor Segmentation From CT Volumes. *IEEE Transactions on Medical Imaging* **37**, 2663–2674. issn: 1558-254X (Dec. 2018).
31. Kline, T. L. *et al.* Performance of an Artificial Multi-Observer Deep Neural Network for Fully Automated Segmentation of Polycystic Kidneys. *Journal of Digital Imaging* **30**, 442–448. issn: 1618-727X (1st Aug. 2017).

5.8. References

32. Van Gastel, M. D. A. *et al.* Automatic Measurement of Kidney and Liver Volumes from MR Images of Patients Affected by Autosomal Dominant Polycystic Kidney Disease. *Journal of the American Society of Nephrology* **30**, 1514–1522. issn: 1046-6673, 1533-3450 (1st Aug. 2019).
33. Shin, T. Y. *et al.* Expert-Level Segmentation Using Deep Learning for Volumetry of Polycystic Kidney and Liver. *Investigative and Clinical Urology* **61**, 555–564. issn: 2466-0493 (Nov. 2020).
34. Fukushima, K. Neocognitron: A Hierarchical Neural Network Capable of Visual Pattern Recognition. *Neural Networks* **1**, 119–130. issn: 0893-6080 (1st Jan. 1988).
35. Lecun, Y., Bottou, L., Bengio, Y. & Haffner, P. Gradient-Based Learning Applied to Document Recognition. *Proceedings of the IEEE* **86**, 2278–2324. issn: 1558-2256 (Nov. 1998).
36. Petzold, K. *et al.* Building a Network of ADPKD Reference Centres across Europe: The EuroCYST Initiative. *Nephrology Dialysis Transplantation* **29**, iv26–iv32. issn: 0931-0509 (suppl_4 1st Sept. 2014).
37. Will, S., Martirosian, P., Würslin, C. & Schick, F. Automated Segmentation and Volumetric Analysis of Renal Cortex, Medulla, and Pelvis Based on Non-Contrast-Enhanced T1- and T2-Weighted MR Images. *Magnetic Resonance Materials in Physics, Biology and Medicine* **27**, 445–454. issn: 1352-8661 (1st Oct. 2014).
38. Rorden, C. *Neurolabusc/MRIcron* 18th Jan. 2021.
39. Chollet, F. *Keras* version 2.2.4. Keras, 2015.
40. Abadi, M. *et al.* TensorFlow: Large-Scale Machine Learning on Heterogeneous Distributed Systems, 19 (9th Nov. 2015).
41. Mahapatra, D. & Buhmann, J. M. Visual Saliency-Based Active Learning for Prostate Magnetic Resonance Imaging Segmentation. *Journal of Medical Imaging* **3**, 014003. issn: 2329-4302, 2329-4310 (Feb. 2016).
42. Daniel, A. *Alexdaniel654/Renal_Segmentor: V1.0.0* version v1.0.0. Zenodo, 6th Oct. 2020.
43. Chen, J., Yang, L., Zhang, Y., Alber, M. & Chen, D. Z. in *Advances in Neural Information Processing Systems* 29 (eds Lee, D. D., Sugiyama, M., Luxburg, U. V., Guyon, I. & Garnett, R.) 3036–3044 (Curran Associates, Inc., 2016).
44. Stollenga, M. F., Byeon, W., Liwicki, M. & Schmidhuber, J. in *Advances in Neural Information Processing Systems* 28 (eds Cortes, C., Lawrence, N. D., Lee, D. D., Sugiyama, M. & Garnett, R.) 2998–3006 (Curran Associates, Inc., 2015).

5.8. References

45. Van Gastel, M. D. A. *et al.* T1 vs. T2 Weighted Magnetic Resonance Imaging to Assess Total Kidney Volume in Patients with Autosomal Dominant Polycystic Kidney Disease. *Abdominal Radiology* **43**, 1215–1222. ISSN: 2366-0058 (1st May 2018).
46. Morris, D. *et al.* Segmentation of the Cortex and Medulla in Multiparametric Magnetic Resonance Images of the Kidney Using K-Means Clustering in Proc. Intl. Soc. Mag. Reson. Med. 27 ISMRM. **27** (Montreal, 13th May 2019), 1915.

Chapter 6

Ex-Vivo Renal MRI

Abstract

This work was presented as a digital poster at the International Society of Magnetic Resonance in Medicine (ISMRM) 27th Annual Meeting 2019 [1] and as a poster at United Kingdom Kidney Week (UKKW) 2019 [2].

Lorem ipsum dolor sit amet, consectetuer adipiscing elit. Ut purus elit, vestibulum ut, placerat ac, adipiscing vitae, felis. Curabitur dictum gravida mauris. Nam arcu libero, nonummy eget, consectetuer id, vulputate a, magna. Donec vehicula augue eu neque. Pellentesque habitant morbi tristique senectus et netus et malesuada fames ac turpis egestas. Mauris ut leo. Cras viverra metus rhoncus sem. Nulla et lectus vestibulum urna fringilla ultrices. Phasellus eu tellus sit amet tortor gravida placerat. Integer sapien est, iaculis in, pretium quis, viverra ac, nunc. Praesent eget sem vel leo ultrices bibendum. Aenean faucibus. Morbi dolor nulla, malesuada eu, pulvinar at, mollis ac, nulla. Curabitur auctor semper nulla. Donec varius orci eget risus. Duis nibh mi, congue eu, accumsan eleifend, sagittis quis, diam. Duis eget orci sit amet orci dignissim rutrum.

6.1 Introduction

In the clinic, renal pathologies are currently assessed via blood tests, urine tests or biopsy followed by histological analysis. Given that both blood tests and urine tests are indirect measures of the health of the kidneys this means that biopsy is the most accurate diagnostic method routinely used, however it is not without its shortcomings. From a patient experience point of view, collecting the tissue sample is an unpleasant and invasive process; from a diagnostic point of view, the results ascertained are not representative of the entirety of the kidney biopsied (typically the left), let alone the other kidney. Additionally, due to the invasive and destructive nature of the procedure, it is not ideal for longitudinal monitoring of renal health. Given these drawbacks in the current methodology, there has been a recent drive to enable the use of Magnetic Resonance Imaging (MRI) for renal diagnosis as it has the potential to be better for both patients and clinicians. The non-ionising nature of MRI makes it suitable for longitudinal study of disease progression; the spatial heterogeneity of the organ can also be assessed. A key aspect in the widespread adoption of MRI in renal clinical practice, is a full understanding of the interplay between the current histological pipeline and the newly developed MRI measurements [3].

The best way to gain this insight is by analysing the same kidney in multiple ways. By taking samples from patients who are undergoing a nephrectomy as part of their standard treatment, it is possible to scan the kidneys in-vivo, remove the kidney, carry out histology and scan the sample ex-vivo. These three complimentary streams of data allow for the comparison of histology and in-vivo MRI with the ex-vivo scans acting as an intermediary, providing high-quality, high-resolution MR data.

Looking in the literature, there are two works that resemble this paradigm, the first, by Friedli et al, correlated T_1 and Apparent Diffusion Coefficient (ADC) with renal interstitial fibrosis and inflammation in a rat model [4]. Establishing a MRI predictor of interstitial fibrosis is especially important as it is present in the majority of renal pathologies and has been established as an excellent indicator of functional recovery [5]. Friedli was able to establish these correlations by scanning the organ in-vivo, ex-vivo and then carrying out histology. It is this sort of methodology we intend to apply to whole human samples. These results were verified in a larger dataset by Berchotold et al [6], however, this study correlated MRI measures with interstitial fibrosis scores from biopsy samples rather than whole organ and as such, does not allow for spatial variability in interstitial fibrosis within the kidney and

is subject to sampling bias [7]. Another work by Uribe et al carried out a similar process investigating the diagnostic capabilities of ADC and fractional anisotropy in prostate cancer using human samples [8]. Although there has not been much work correlating human kidney MRI with histology, there has been interesting work on ex-vivo MRI samples using similar methods to those we wish to undertake. A very comprehensive paper by Sengupta et al details their ability to image an 80 mm^3 sample of human occipital lobe generating $60\text{ }\mu\text{m}$ isotropic T_2^* weighted data and $200\text{ }\mu\text{m}$ isotropic quantitative T_2^* maps [9]. This was achieved on a 9.4T human scanner using a custom made 16 channel phased array and shows the benefits that custom hardware can bring to ex-vivo imaging on human scanners.

As the purpose of this study is to compare pre-existing histological analysis with newly developed, but previously documented, renal MRI protocols, the largest area in need of development is the ex-vivo scanning of samples, as such this is a large focus of this chapter. Here, the aim is to collect ADC, T_1 , T_2 and T_2^* data both ex-vivo and in-vivo for comparison. Established protocols exist within the group for ADC, T_1 and T_2^* collection but there are multiple methods of renal T_2 mapping which have not been optimised [10–13]. Here T_2 mapping methods are compared before choosing one to include in the scan card to perform on nephrectomy patients. As well as the MRI acquisition, attention needs to be paid to the fixing process. It will not be possible to scan unfixed organs therefore, a knowledge of the effects fixation has upon the kidneys needs to be gained. No literature on this topic exists and thus, this is an area we need to explore ourselves.

6.2 Methods

6.2.1 Sample Acquisition and Fixation

Initial samples were acquired from a local slaughterhouse, placed into Phosphate-buffered Saline (PBS) for transport to the laboratory before being transferred to ten times the samples volume of 10% Neutral Buffered Formalin (NBF) for twenty four hours. The time between slaughter and transferring the samples to NBF was reduced as much as possible to minimise the effects of ischemic injury. Once the samples had been fixed they were washed in fresh PBS and remained in this solution while being scanned to avoid susceptibility artefacts that would be induced by either scanning the samples immersed in NBF or in air. Where possible, both kidneys were collected from the animal, with one being used for MRI and the other being used to biopsy for histological staining. While the samples acquired from the slaughterhouse were useful for early development work there were consistency issues that will be explained in detail in Section 6.3, for this reason a collaboration between Sir Peter Mansfield Imaging Centre (SPMIC) and The University of Nottingham School of Veterinary Medicine and Science has begun. This allows the procurement of much higher quality samples with a greater degree of control.

6.2.2 T_1 Mapping

Acquisition

Ex-vivo T_1 maps can be acquired at field strengths of 3T and 7T. If the time at which the sample is scanned does not need to be precisely controlled or matched with the time of biopsy then the sample can be scanned at both field strengths successively however if scanning and biopsy needed to be time matched then the sample is only scanned at 3T.

T_1 maps are produced using an ultrafast gradient echo scheme. By carrying out multiple scans with different Inversion Time (TI) it is possible to sample the inversion recovery of the tissue and as such, estimate T_1 . An example of the acquisitions at each inversion time is shown in Figure 6.1

6.2. Methods

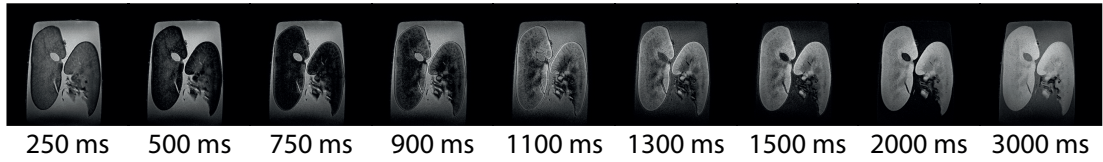


Figure 6.1: Acquisitions at each of the TI at 7T.

The acquisition parameters at 3T are Field Of View (FOV) = $160 \times 160 \times 50$ mm, voxel size = $0.7 \times 0.7 \times 1.0$ mm 3 , Repetition Time (TR)/Echo Time (TE) = 11 ms/5 ms, Flip Angle (FA) = 8° , Bandwidth = 41.6 Hz/pixel, Turbo Field Echo (TFE) Factor = 64, Sensitivity Encoding (SENSE) Factor = 2.5, Acquisition Time \approx 270 sec per TI collected. The acquisition parameters at 7T are FOV = $192 \times 170 \times 24$ mm, voxel size = $0.6 \times 0.6 \times 0.6$ mm 3 , TR/TE = 7.2 ms/3.3 ms, FA = 8° , Bandwidth = 56.8 Hz/pixel, TFE Factor = 240, SENSE Factor (P/S) = 2.0/1.5, Acquisition Time \approx 270 sec per TI collected. Initially inversion times of 400 ms, 500 ms, 750 ms, 900 ms, 1100 ms, 1300 ms and 1500 ms were collected at 3T and inversion times of 250 ms, 500 ms, 750 ms, 900 ms, 1100 ms, 1300 ms, 1500 ms, 2000 ms and 3000 ms at 7T however to reduce the scan time of the 3T protocol, this was reduced to inversion times of 400 ms, 500 ms, 750 ms, 900 ms, 1100 ms and 2600 ms. The choice of these inversion times will be elaborated upon later.

Analysis

The signal recorded at each inversion time is proportional to the modulus of the true longitudinal magnetisation, Figure 6.2. To combat this we can apply polarity correction to the data by saving the phase information and applying the methods of Szumowski et al [14]. This results in a greater dynamic range and thus smaller confidence intervals than using the none polarity corrected data.

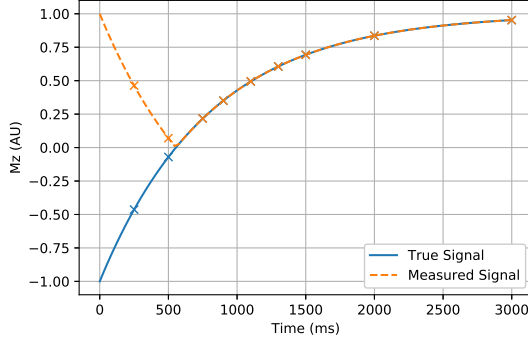


Figure 6.2: A simulation of the true and measured magnetisation for a T_1 of 800 ms. The crosses represent the inversion times at which the inversion recovery is sampled.

Once the data has been polarity corrected a voxel by voxel least squares trust region reflective method is used to fit the data to Equation (6.1) and estimate the T_1 and M_0 of the tissue in that voxel along with an uncertainty in the fit [15]. This data processing is carried out using an in-house Python package. Once the T_1 maps are generated, Region Of Interest (ROI) are defined for the renal medulla and renal cortex and the mean T_1 in these ROI recorded.

$$M_z = M_0 \left(1 - 2 \cdot e^{-TI/T_1} \right) \quad (6.1)$$

6.2.3 T_2 Mapping

Compared to other quantitative renal measurements, T_2 mapping is still relatively un-explored in-vivo or ex-vivo with little consensus in the community about which methods are best suited to each situation [16]. This lack of consensus and existing literature meant that more work was required to establish the optimum protocol for our use case. Due to this works interest to the wider community out of the context of the nephrectomy paradigm, the development and comparison of T_2 mapping protocols is explored in Chapter 3.

6.2.4 T_2^* Mapping

Acquisition

Ex-vivo T_2^* maps can be acquired at both 3T and 7T using a multi-slice Fast Field Echo (FFE) sequence with scans being performed at a range of different echo times. An example of the acquisition at each echo time is shown in Figure 6.3

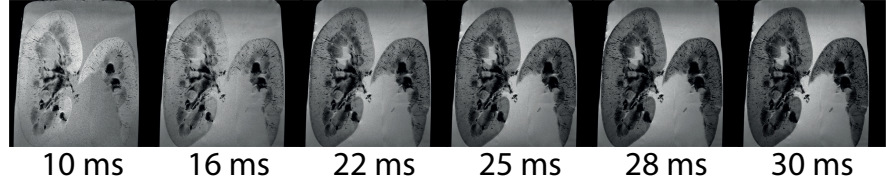


Figure 6.3: Acquisitions at each of the TE at 7T.

The acquisition parameters at 3T are $\text{FOV} = 145 \times 145 \times 15 \text{ mm}$, voxel size = $0.6 \times 0.6 \times 1.5 \text{ mm}^3$, $\text{TR} = 697 \text{ ms}$, $\text{FA} = 38^\circ$, SENSE Factor = 2.0, Acquisition Time $\approx 180 \text{ sec}$ per TE collected. The acquisition parameters at 7T are $\text{FOV} = 145 \times 145 \times 10 \text{ mm}$, voxel size = $0.5 \times 0.5 \times 1.0 \text{ mm}^3$, $\text{FA} = 38^\circ$, SENSE Factor = 2.0, Acquisition Time $\approx 180 \text{ sec}$ per TE collected. Initially echo times were 15 ms, 20 ms, 25 ms, 30 ms, 35 ms, 40 ms and 50 ms at 3T and 10 ms, 16 ms, 22 ms, 25 ms, 28 ms and 30 ms at 7T however to reduce acquisition times, the 3T echo times were reduced to 15 ms, 20 ms, 25 ms, 40 ms and 50 ms.

Analysis

The data is fit voxel by voxel using a weighted echo time fit from the log of the exponential signal decay (Equation (6.2)) to generate the T_2^* maps [17]. This data processing is carried out using an in-house Python package. The ROI were defined using the T_1 weighted data if available as it has a greater cortical medullary contrast at shorter times from fixation. The mean T_2^* in these ROI is recorded.

$$S(t) = S_0 \cdot e^{-TE/T_2^*} \quad (6.2)$$

6.2.5 Apparent Diffusion Coefficient

Acquisition

Optimisation of b values

Post-Processing and Analysis

6.2.6 Diffusion Tensor Imaging

As part of the nephrectomy protocol, Chapter 6, we want to be able to assess the microstructure of the kidneys, one avenue to pursue for this is the use of Diffusion Tensor Imaging (DTI). FA has been shown to correlate with Glomerular Filtration Rate (GFR) [18] and mean tract length is an indicator of ureteropelvic junction obstruction [19] showing that tractography can be used to assess renal structure.

One of the major hurdles to overcome in developing a renal DTI protocol for this study was correction of both Echo Planar Imaging (EPI) readout distortions and eddy current induced distortions. This was achieved using a pipeline based around fMRIB Software Library (FSL)'s topup [20, 21] and eddy [22] routines. Key acquisition parameters for the sequence are 64 directions arranged over a whole spherical shell to assist with eddy current correction, this whole acquisition is then repeated with the opposite phase-encode direction to enable EPI distortion correction. A b-value of 600 s/mm^2 is used. FA maps are generated using FSL and tractography is processed using an in-house pipeline developed using the Dipy Python library [23].

Using this pipeline, images such as those in figures 6.4 and 6.5 could be produced. This protocol is now ready to be used on patients undergoing a nephrectomy.

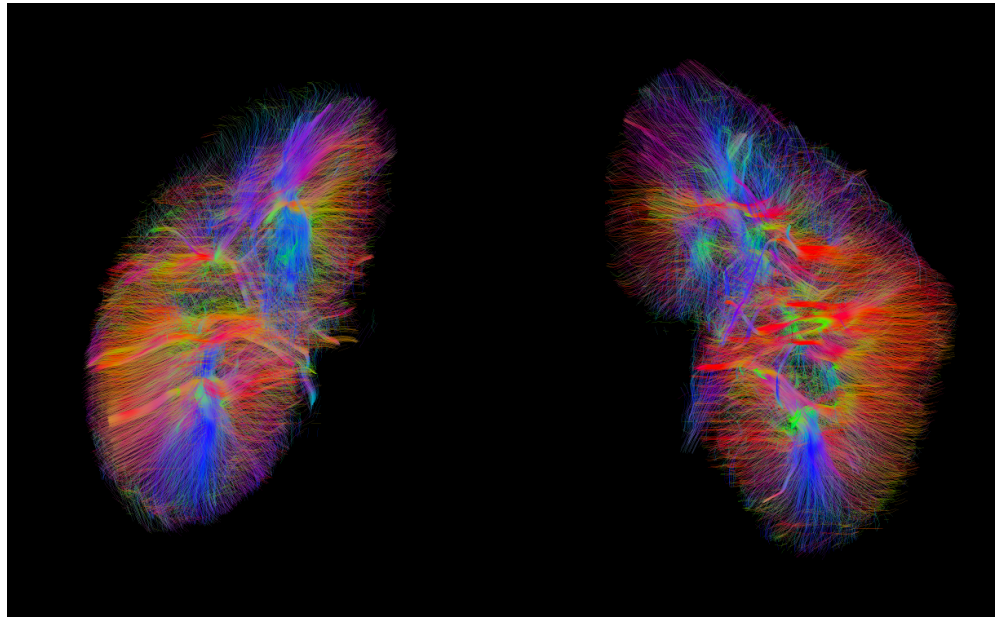


Figure 6.4: Example tractography generated using the above protocol.

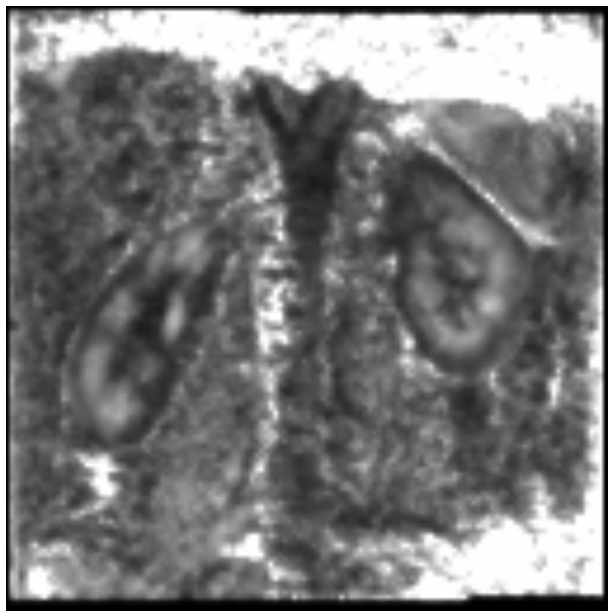


Figure 6.5: An example FA map generated using the protocol above.

Acquisition

Post-Processing and Analysis

Distortion Correction

Fractional Anisotropy

Tractography

6.2.7 Layer Based Analysis

The vast majority of analysis of renal MRI data is based around defining ROI within the kidneys. While this method has provided excellent results, it is by no means perfect as these ROI need to be manually defined, leading to human bias, or defined by an automated method which, as outlined in Chapter 5, can be difficult to generalise.

Taking inspiration from the analysis pipelines used by neuroimagers [24–26], a method of dividing the kidneys into layers of equal thickness was developed. This method uses a three-dimensional FreeSurfer mesh on the surface of the kidney [27] and levelsets to produce a map of how far each voxel is from the surface. From this map it is possible to place voxels into layers of any thickness. An example of this method being applied to both the brain and an ex-vivo kidney sample can be seen, figures 6.6a and 6.6b respectively.

One of the main challenges in transferring this technique is coping with the reduced FOV that comes with body imaging. Given that the method essentially asks how far is each voxel from the closes vertex on the mesh, if the mesh has a large hole in it where the slices stop covering the kidney, then the quantitative nature of this depth map is compromised.

6.2. Methods

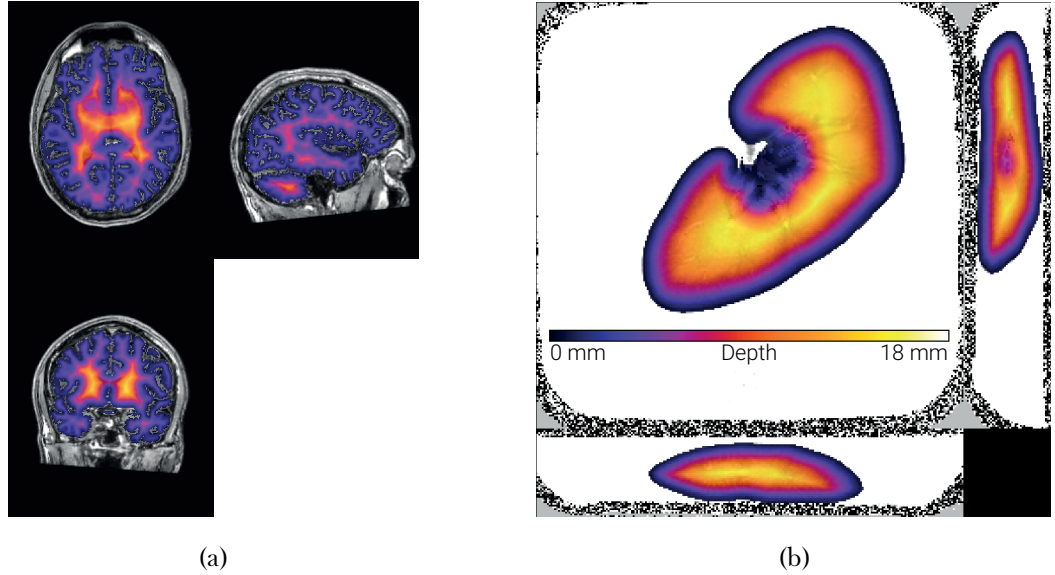


Figure 6.6: (a) A depth mask of the brain. Lighter areas are deeper inside the brain. (b) A depth mask applied to a quantitative T_1 map.

This levelset method was compared to two other methods of producing layers in the kidneys, a two-dimensional and a three-dimensional version of the Twelve Layer Concentric Objects (TLCO) method [28, 29]. Each method was tested with a volume that included the entire kidney, and a cropped volume that only included the central section of the kidney, simulating the reduced FOV that is common in body imaging. The layers generated were applied to a T_1 map with the mean and standard deviation of T_1 in each layer being plotted, Figure 6.7.

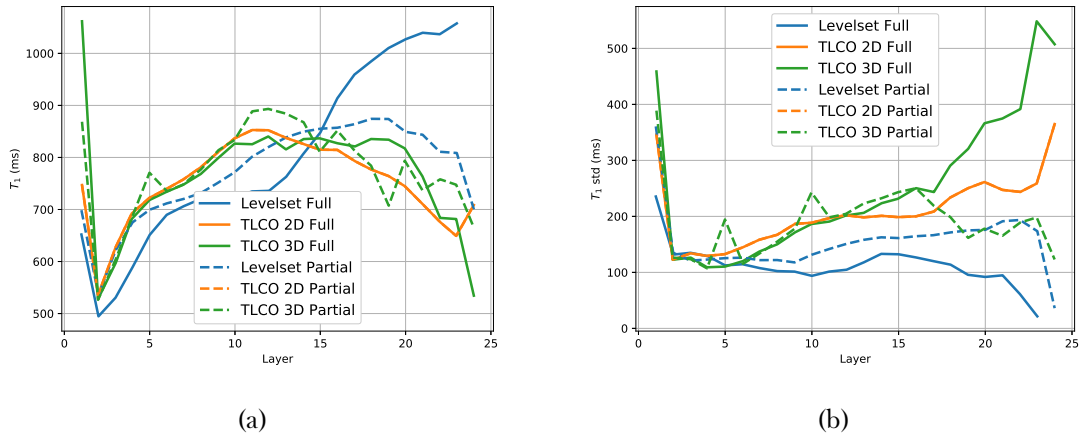


Figure 6.7: (a) The mean T_1 within each layers produced by each of the three methods when processing either the full volume of the kidney or only the central slices. (b) The standard deviation of the T_1 within the layers produced by each method.

6.2. Methods

In Figure 6.7b we can see that the layers output by the levelset method when applied to a full volume dataset produce the minimum standard deviation, this means the layers are the most anatomically sensible as a smooth transition of T_1 is expected with depth in the kidney and therefore the variance in each layer should be relatively small. Given this method produces the most realistic layers, other methods will be compared to it.

Neither of the TLCO methods manage to capture the increase in T_1 that can be seen deeper in the kidney. They also have a much larger standard deviation per layer for deeper layers than the levelset method implying that the layers produced are a mixture of cortex and medulla. When comparing the performance of each method with only a partial volume of kidney, the levelset method produces the results that are closer to that of the full volume levelset.

Given this method can be used both in-vivo and on ex-vivo samples, they will make for an interesting additional analysis pipeline for the work in Chapter 6.

6.3 Results and Discussion

6.3.1 Fixation and Protocol Development

As was alluded to in Section 6.2.1, there was significant variability in the quality of the samples collected from the slaughterhouse. This was largely due to the legislation surrounding animals slaughtered to enter the human food chain. If any part of the animal is destined for human consumption then the carcase must be thoroughly inspected before any tissue can be released. This can cause two issues. As part of the inspection, the kidneys need to be examined for parasites, this is done by making an incision in the organ, however, the quality of this incision can vary massively with some samples having a 20 mm slice cut into them while others are roughly cut in half. The second issue is caused by the variable time between slaughter and the tissue being released after inspection. For these reasons kidneys began to be procured from Veterinary Science collaborating with Prof David Gardner. The animals slaughtered there are not destined for human consumption and as such the kidneys can be placed into PBS and subsequently NBF far quicker and the kidneys do not need to be sliced open for inspection. The difference in the samples from these two sources can clearly be seen in Figure 6.8. This collaboration also enables the procurement of kidneys from a greater range of animals including different ages of pigs and therefore different degrees of fibrosis and inducing Acute Kidney Injury (AKI) in the animals prior to scanning and histology. Veterinary Science can also carry out the histology in house, thus streamlining the protocol by avoiding transporting one kidney to Derby for histology and the other to SPMIC for scanning.

6.3. Results and Discussion

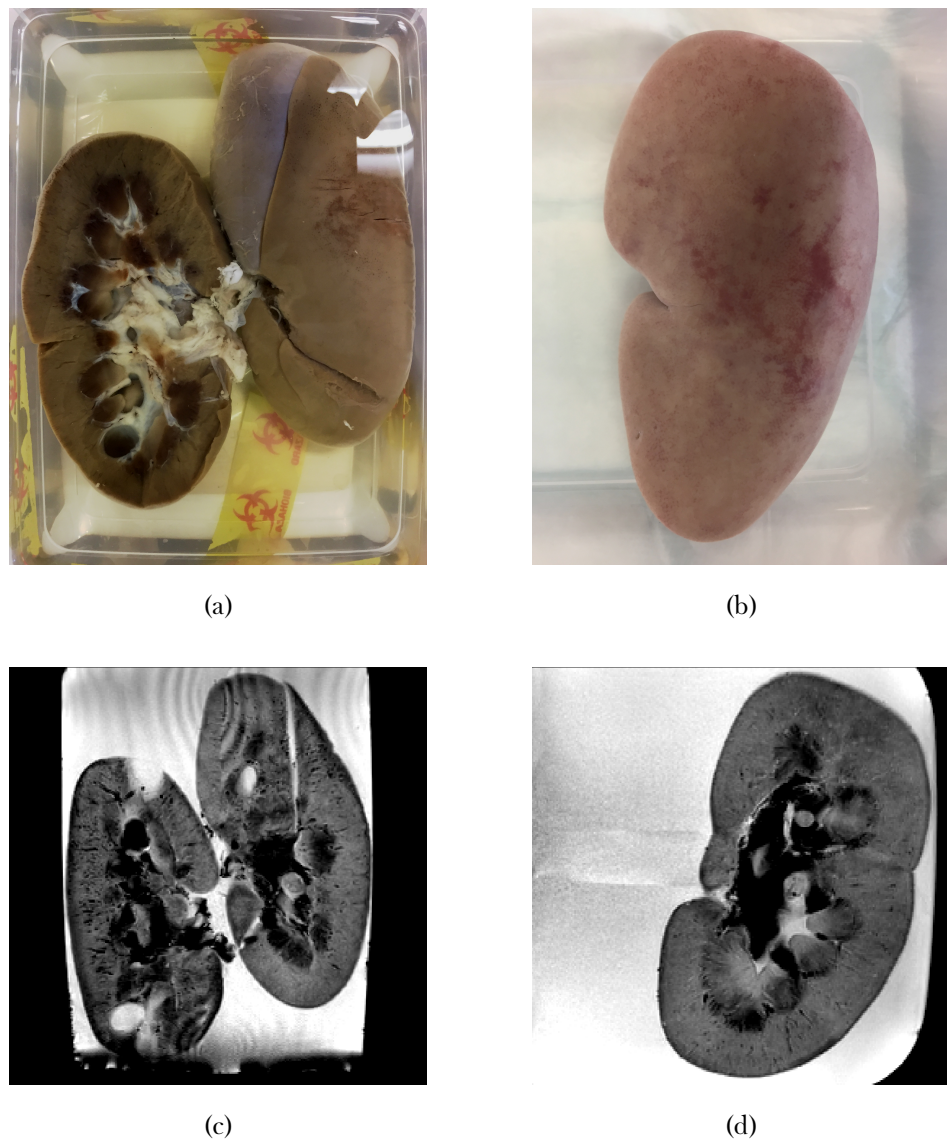


Figure 6.8: (a) An example of a sample procured from the slaughterhouse after it has been fixed. The left hand kidney has been sliced in half; the right hand kidney has the incisions from the meat inspector clearly visible. (b) An example of a sample procured from Veterinary Science post fixing. (c) An example of a T_2 weighted FFE with $TE = 40$ ms of a kidney procured from the slaughterhouse. (d) An example of a T_2 weighted FFE with $TE = 40$ ms of a kidney procured from Veterinary Science.

Once samples had been fixed and transferred to PBS they could be placed into the scanner. Using the protocols outlined above it was possible to generate maps as shown in Figure 6.9.

6.3. Results and Discussion

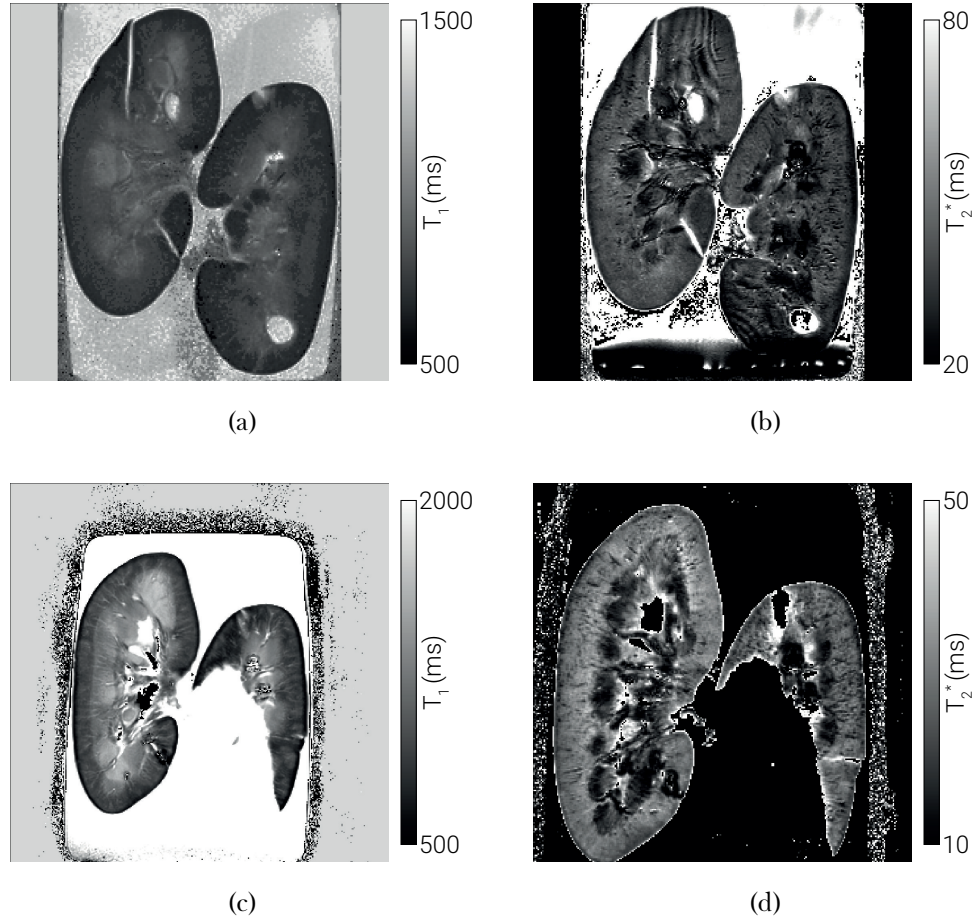


Figure 6.9: (a) T_1 map of a kidney twenty four hours after fixation at 3T (b) T_2^* map twenty four hours after fixation at 3T (c) T_1 map twenty four hours after fixation at 7T (d) T_2^* map twenty four hours after fixation at 7T. The sample shown in the 3T and 7T figures is different.

6.3.2 Monitoring Changes in MR Parameters Post Fixation

To study the effects of the fixation process upon MR measurements, a kidney was fixed as per the method in Section 6.2.1 and scanned at both field strengths of 3T and 7T. Collecting a T_1 and T_2^* map took approximately 90 minutes per field strength. Once the maps had been generated, ROI were defined and the mean T_1 and T_2^* for the cortex and the medulla were calculated. The sample was monitored for ten weeks. The variation in T_1 and T_2^* over time can be seen in Figure 6.10.

6.3. Results and Discussion

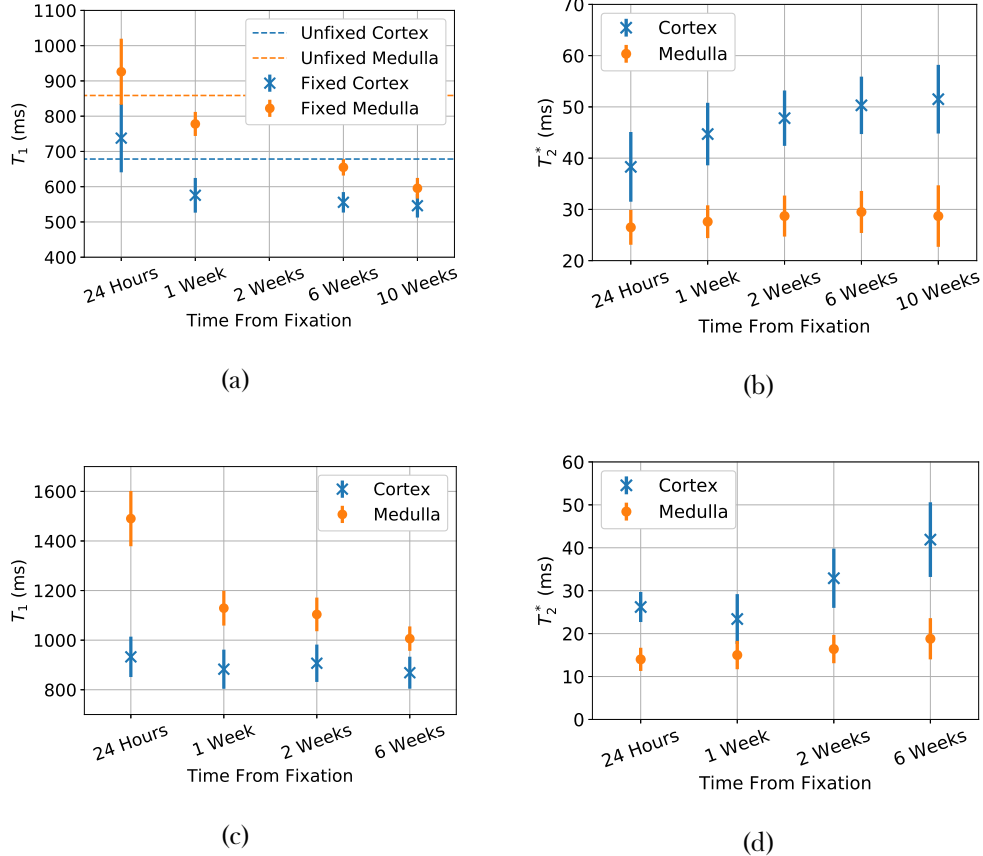


Figure 6.10: (a) Variation in T_1 as a function of time after fixation measured at 3T (b) Variation in T_2^* as a function of time after fixation measured at 3T (c) Variation in T_1 as a function of time after fixation measured at 7T (d) Variation in T_2^* as a function of time after fixation measured at 7T.

Unfortunately due to technical scanner issues, we were not able to scan the sample at 7T at ten weeks and the quality of the 3T T_1 acquisition at two weeks was significantly inferior; as such these data points have been omitted. It can be seen that the largest changes in T_1 and T_2^* occur between twenty four hours and one week after fixation, after that there is a general trend that the T_1 of the cortex and medulla converge while the T_2^* of each tissue type diverges, one could argue that the T_2^* of the cortex measured at 3T is plateauing. This means that, although the samples will reach a steady state, in the first few weeks after fixation, their T_1 and T_2^* will have a dependence on time. This necessitates the need to standardise the protocol, specifically the time at which the samples are scanned. It would have been useful to know the T_1 and T_2^* of unfixed porcine kidneys and as such, a fresh, unfixed kidney was scanned using the same protocol. Unfortunately, due to the difference in stiffness between fixed and unfixed kidneys, the same protocol did not deliver usable T_2^*

6.3. Results and Discussion

data as the unfixed kidney vibrated too much while floating in the PBS. This problem could potentially be reduced by either vibration insulation between the sample and the scanner as per Dawe et al [30] or by embedding the sample in an agarose medium rather than allowing it to float in PBS as per Kolk et al[31]. The T_1 of the unfixed kidney was seen to be between that of the fixed kidney between 24-hours and one week.

To investigate this time dependence over a shorter time scale, a pair of kidneys were acquired and fixed as before. It will be possible to scan most human samples within 24 hours of fixation, as such it is desirable to see how much T_1 , T_2^* and histology change over this period. Scanning was only carried out at 3T as more frequent measurements were preferable to measurements at different field strengths. For this reason the number of inversion times and echo times used to generate the T_1 and T_2^* maps was reduced to TI = 400 ms, 500 ms, 750 ms, 900 ms, 1100 ms, 2600 ms and TE = 15 ms, 20 ms, 25 ms, 40 ms, 50 ms respectively. The choice of these inversion/echo times was arrived at empirically by carrying out the analysis pipeline on a single slice of data using each combination of six and five of the previously used TIs and TEs respectively. The results from each combination of TI/TE were compared to those generated when using the full complement of inversion/echo times and the combination delivering the minimum difference chosen. This reduction in the number of inversion times resulted in a mean error per voxel in the kidney of 20.9 ± 12.8 ms if the full complement of inversion times was taken as the ground truth, the reduction in echo times resulted in a mean error of 0.3 ± 1.2 ms.

Scanning sessions started at 1.5 hours, 2.5 hours, 4 hours, 5.5 hours, 19 hours and 22 hours after the sample was removed from the NBF. Due to the potential for the properties to change relatively quickly, especially T_1 , it was decided to randomise the order in which the inversion/echo times were collected, this way any change in T_1/T_2^* over the 30/20 minute acquisition period would manifest itself as non-systematic noise and thus will increase the uncertainty in the fit rather than affecting the predicted value. At the start of each scanning session, a biopsy was performed on the kidney not being scanned. Masson's trichrome and Haematoxylin and Eosin (H and E) staining was performed on these samples.

6.3. Results and Discussion

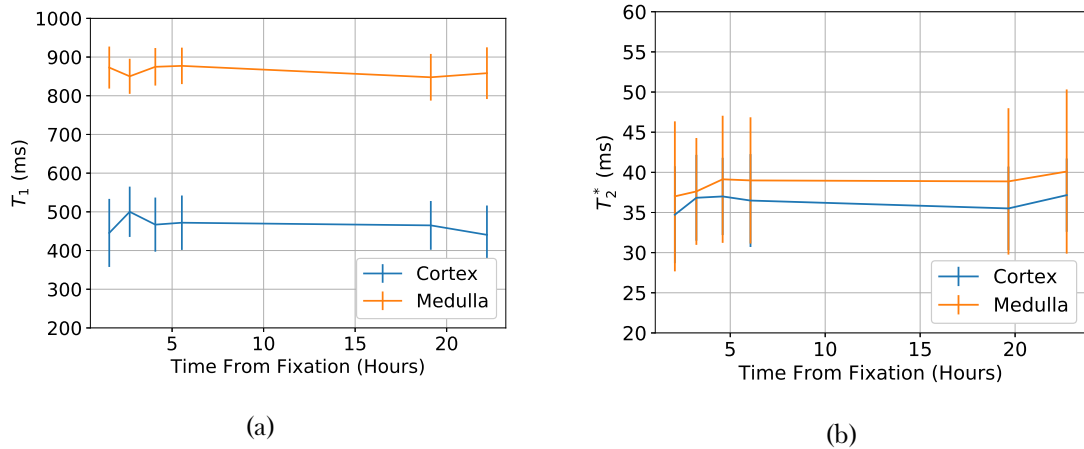


Figure 6.11: (a) Variation in T_1 as a function of time after fixation measured at 3T (b) Variation in T_2^* as a function of time after fixation measured at 3T.

No significant change in T_1 or T_2^* was observed over the period the sample was monitored. This is promising as it means that when this protocol is applied to human samples, there will be a relatively large time window in which the ex-vivo scan can be carried out, making the experimental procedure simpler. The corresponding histology results showed no change in the cortex over this period however there was a noticeable inflammatory response in the medulla.

It was noted that the sample used for this experiment was not of especially high quality, the kidney has two slices in it, one that almost bifurcated the sample along the coronal plane, another cut down one half of the sample along the sagittal plane, visible in Figure 6.12a. These cuts meant that air became trapped within the sample causing it to float in the PBS. If not corrected this would cause large susceptibility artefacts where the sample came into contact with the air at the top of the PBS; to remedy this the sample was entirely bifurcated. Despite the best efforts of investigators, air bubbles remained in the sagittal slice, causing the aforementioned artefacts, especially visible in Figure 6.12b. Given these concerns over sample quality, it was decided to scan the sample again one week after fixation, to match the time period in the previous experiment (Figure 6.10).

6.3. Results and Discussion

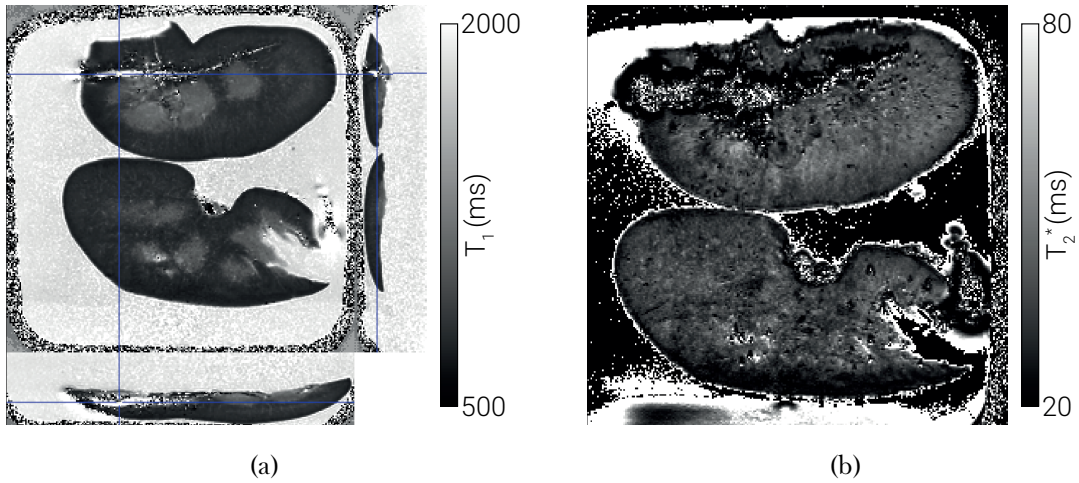


Figure 6.12: (a) An example of the T_1 map collected from the short time scale kidney (b) An example of the T_2^* map collected from the short time scale kidney.

It was expected that upon repeating the measurements one week later, the T_1 of both cortex and medulla would decrease and the T_2^* of the cortex would increase. This was not the case, there was a slight decrease in the T_1 of the medulla but otherwise, no change was observed, Figure 6.13. This lead us to conclude that the large cuts in the sample had lead to a different level of fixation. Subsequent to this, samples were to be procured from Veterinary Science as they are more consistent and therefore more akin to the human samples that will be used.

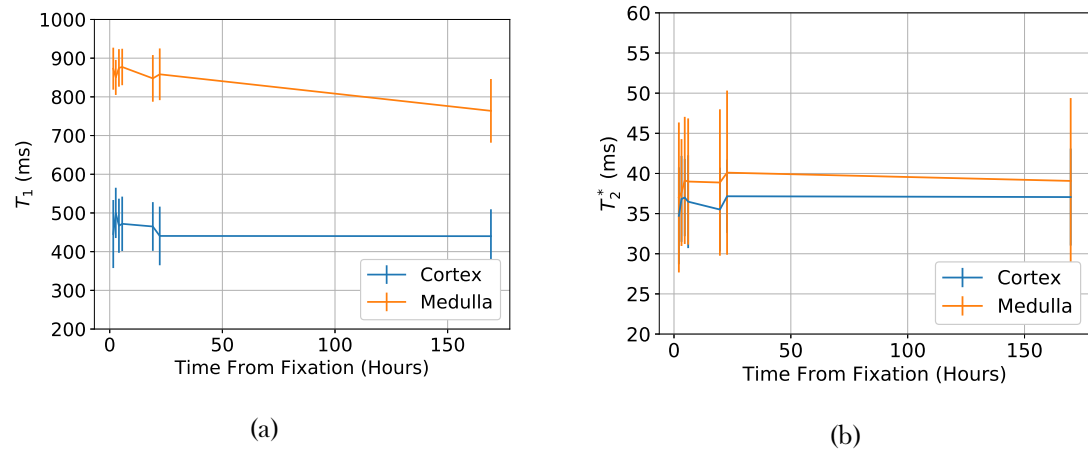


Figure 6.13: (a) Variation in T_1 as a function of time after fixation measured at 8T (b) Variation in T_2^* as a function of time after fixation measured at 3T.

6.3.3 Comparing MR and Histological Measures in Aged Kidneys

To verify the correlation of MR measurements with histology, kidneys were collected from a 0.5 year old and 2.5 year old pig. These different ages were expected to have differing levels of renal inflammation and fibrosis. Figure 6.14 shows example MRI data collected from these samples, Figure 6.15 shows the quantitative differences in T_1 and T_2^* between the two samples.

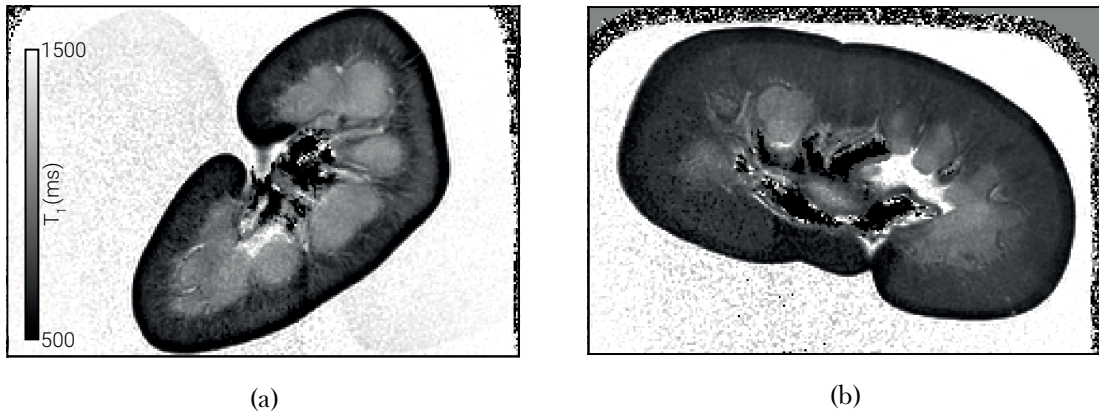


Figure 6.14: (a) T_1 map of a 0.5 year old pig kidney. (b) T_1 map of a 2.5 year old pg kidney.

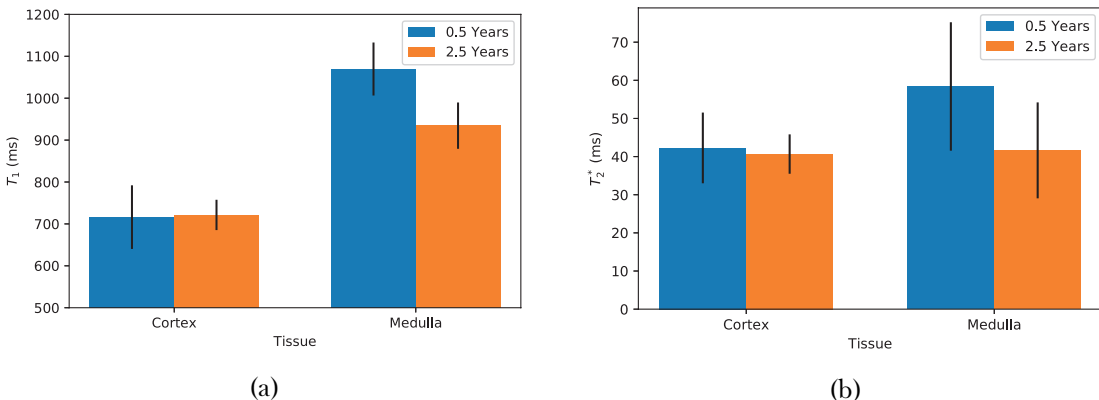


Figure 6.15: (a) The T_1 of the renal cortex and medulla of the two samples. (b) The T_2^* of the renal cortex and medulla of the two samples.

No significant change is observed in the T_1 or T_2^* of cortex the two kidneys. There is however a decrease in T_1 seen in the medulla of the older kidney. Cortical samples were removed from the same animals for histological analysis. These samples were stained using H and E and Masson's trichrome to enable the evaluation of levels of fibrosis, these micrographs are shown in Figure 6.16.

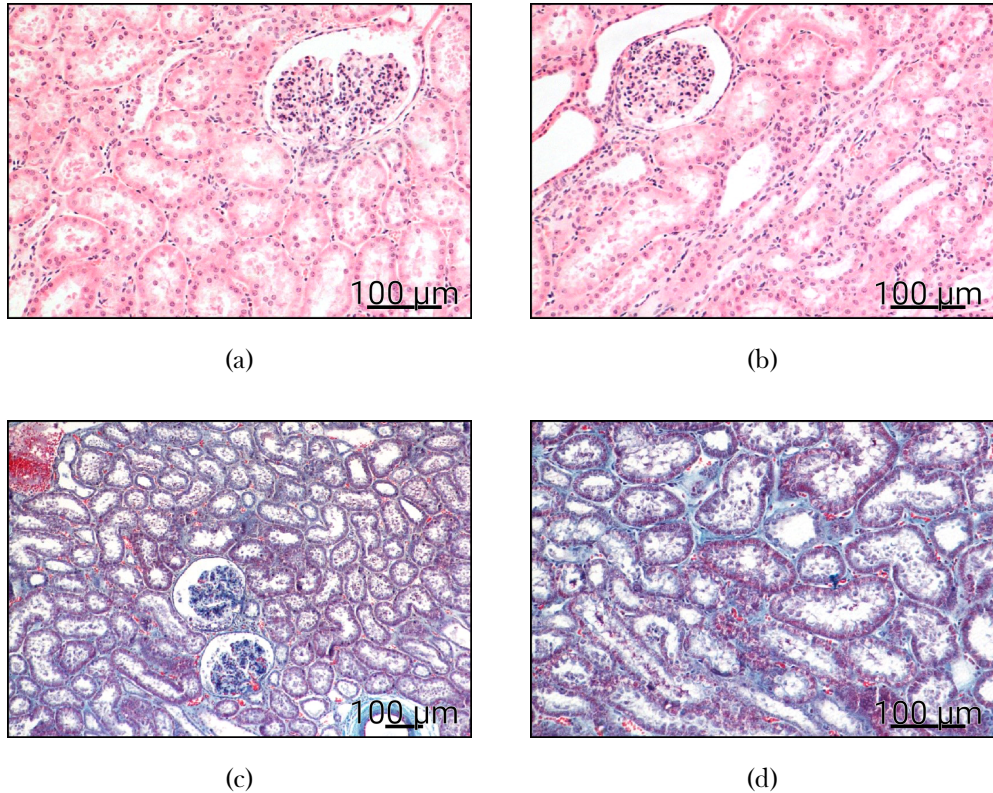


Figure 6.16: (a) A sample of renal cortex from a 0.5 year old pig stained with H and E. (b) A sample of renal cortex from a 2.5 year old pig stained with H and E. (c) A sample of renal cortex from a 0.5 year old pig stained with Masson's trichrome. (d) A sample of renal cortex from a 2.5 year old pig stained with Masson's trichrome.

No significant difference is seen between the histology of these cortical samples. This means that MRI and histology are in agreement. Unfortunately no samples were taken from the renal medulla, the area which showed a change in MR measurements. In future samples with a larger difference in age should be used as these will have a greater difference in fibrosis and samples should be taken from the medulla for histological analysis.

6.4 Conclusions and Future Work

This chapter shows progress towards correlating renal MRI measurements with histology. We are able to acquire high resolution T_1 , T_2 , T_2^* maps. We have also developed protocols to carry out simultaneous biopsy for histology and MRI acquisition. These protocols have shown that the T_1 and T_2^* of the kidneys are not constant after fixation however there is a window of 24-hours after fixation in which scanning is optimum. We have also

6.4. Conclusions and Future Work

shown that these measures agree with histology. Below are listed some of the directions in which future work could explore.

6.4.1 Protocol Validation on a Single Sample

As each protocol, including those in Section ??, has been developed separately, they have not been carried out on the same sample, as the intention is to use all the protocols outlined in Section 6.2 on each nephrectomy sample, it would be useful to collect all protocols on a single sample. This could be coupled with a repeat investigation into the effects of ageing by collecting data from kidneys with a larger difference in ages.

6.4.2 Ex-Vivo Sample Coil

Sengupta demonstrated the benefits of using custom made ex-vivo sample coils in human scanners [9]. Currently scanning uses the standard head coils however this results in a relatively large distance between sample and coils as seen in Figure 6.17. There would certainly be improvements in data quality if a coil specifically designed for small sample imaging at 7T were fabricated.



Figure 6.17: A sample sat within the 32 channel 3T head coil. A bespoke ex-vivo sample coil would have less space between the coil and the sample.

6.4.3 Human Organs

All work thus far has been using porcine kidneys. While these provide an excellent model for protocol development due to their similarities to human kidneys, the utility of this investigation will be enhanced massively when human organs are studied. To this end, once the development work has been completed and protocols finalised, samples will begin to be procured from subjects undergoing a nephrectomy as part of their standard clinical care.

Another source of human organs are those rejected for transplant. Due to the relatively small time window in which a transplant centre has between an organ donation being made and the organ losing its transplant viability, a large number of human kidneys are unable to be successfully donated. While not suitable for transplant any more, these organs would still be useful in providing ex-vivo MRI data and histology in the healthy population. There are pre-existing agreements enabling failed transplant tissue to be used in scientific research, as such, this would be an interesting avenue to explore.

6.5 Acknowledgements

We are grateful for access to the University of Nottingham's Augusta high performance computing service.

6.6 References

1. Daniel, A. *et al.* *The Effects of Fixation and Age on Relaxometry Measurements of Ex-Vivo Kidneys* in *Proc. Intl. Soc. Mag. Reson. Med.* 27 International Society of Magnetic Resonance in Medicine Annual Meeting (Montreal, 13th May 2019).
2. Kazmi, I. *et al.* *Determining Optimal Technique for Tissue Fixation for Ex-Vivo MRI Imaging of Porcine Kidneys* in. United Kingdom Kidney Week (Brighton, 6th May 2019).
3. Simms, R. & Sourbron, S. Recent Findings on the Clinical Utility of Renal Magnetic Resonance Imaging Biomarkers. *Nephrology Dialysis Transplantation* **35**, 915–919. issn: 0931-0509 (1st June 2020).
4. Friedli, I. *et al.* New Magnetic Resonance Imaging Index for Renal Fibrosis Assessment: A Comparison between Diffusion-Weighted Imaging and T1 Mapping with Histological Validation. *Scientific Reports* **6**. issn: 2045-2322. pmid: 27439482 (21st July 2016).
5. Risdon, R. A., Sloper, J. C. & De Wardener, H. E. Relationship Between Renal Function and Histological Changes Found In Renal-Biopsy Specimens From Patients With Persistent Glomerular Nephritis. *The Lancet. Originally Published as Volume 2, Issue 7564* **292**, 363–366. issn: 0140-6736 (17th Aug. 1968).
6. Berchtold, L. *et al.* Validation of the Corticomedullary Difference in Magnetic Resonance Imaging-Derived Apparent Diffusion Coefficient for Kidney Fibrosis Detection: A Cross-Sectional Study. *Nephrology Dialysis Transplantation* **35**, 937–945. issn: 0931-0509 (1st June 2020).
7. Leung, G. *et al.* Could MRI Be Used To Image Kidney Fibrosis? A Review of Recent Advances and Remaining Barriers. *Clinical Journal of the American Society of Nephrology* **12**, 1019–1028. issn: 1555-9041, 1555-905X (7th June 2017).
8. Uribe, C. F. *et al.* In Vivo 3 T and Ex Vivo 7 T Diffusion Tensor Imaging of Prostate Cancer: Correlation with Histology. *Magnetic Resonance Imaging* **33**, 577–583. issn: 0730-725X, 1873-5894 (1st June 2015).
9. Sengupta, S. *et al.* High Resolution Anatomical and Quantitative MRI of the Entire Human Occipital Lobe Ex Vivo at 9.4T. *NeuroImage*. issn: 1053-8119 (20th Mar. 2017).
10. Wolf, M. *et al.* Magnetic Resonance Imaging T1- and T2-Mapping to Assess Renal Structure and Function: A Systematic Review and Statement Paper. *Nephrology Dialysis Transplantation* **33**, ii41–ii50. issn: 0931-0509 (suppl_2 1st Sept. 2018).

6.6. References

11. Franke, M. *et al.* Magnetic Resonance T2 Mapping and Diffusion-Weighted Imaging for Early Detection of Cystogenesis and Response to Therapy in a Mouse Model of Polycystic Kidney Disease. *Kidney International* **92**, 1544–1554. issn: 0085-2538 (1st Dec. 2017).
12. Li, X., Bolan, P. J., Ugurbil, K. & Metzger, G. J. Measuring Renal Tissue Relaxation Times at 7 T. *NMR in Biomedicine* **28**, 63–69. issn: 1099-1492 (2015).
13. Zhang, J. L. *et al.* Reproducibility of R2* and R2 Measurements in Human Kidneys in Proc. *Intl. Soc. Mag. Reson. Med.* 19 ISMRM. **19** (2011), 2954.
14. Szumowski, J. *et al.* Signal Polarity Restoration in a 3D Inversion Recovery Sequence Used with Delayed Gadolinium-Enhanced Magnetic Resonance Imaging of Cartilage (dGEMRIC). *Journal of Magnetic Resonance Imaging* **36**, 1248–1255. issn: 1522-2586 (1st Nov. 2012).
15. Branch, M., Coleman, T. & Li, Y. A Subspace, Interior, and Conjugate Gradient Method for Large-Scale Bound-Constrained Minimization Problems. *SIAM Journal on Scientific Computing* **21**, 1–23. issn: 1064-8275 (1st Jan. 1999).
16. Dekkers, I. A. *et al.* Consensus-Based Technical Recommendations for Clinical Translation of Renal T1 and T2 Mapping MRI. *Magnetic Resonance Materials in Physics, Biology and Medicine*. issn: 1352-8661 (22nd Nov. 2019).
17. Cox, E. F. *et al.* Multiparametric Renal Magnetic Resonance Imaging: Validation, Interventions, and Alterations in Chronic Kidney Disease. *Frontiers in Physiology* **8**. issn: 1664-042X (2017).
18. Liu, Z. *et al.* Chronic Kidney Disease: Pathological and Functional Assessment with Diffusion Tensor Imaging at 3T MR. *European Radiology* **25**, 652–660. issn: 0938-7994, 1432-1084 (1st Mar. 2015).
19. Delgado, J. *et al.* Pilot Study on Renal Magnetic Resonance Diffusion Tensor Imaging: Are Quantitative Diffusion Tensor Imaging Values Useful in the Evaluation of Children with Ureteropelvic Junction Obstruction? *Pediatric Radiology* **49**, 175–186. issn: 1432-1998 (1st Feb. 2019).
20. Andersson, J. L. R., Skare, S. & Ashburner, J. How to Correct Susceptibility Distortions in Spin-Echo Echo-Planar Images: Application to Diffusion Tensor Imaging. *NeuroImage* **20**, 870–888. issn: 1053-8119 (1st Oct. 2003).
21. Smith, S. M. *et al.* Advances in Functional and Structural MR Image Analysis and Implementation as FSL. *NeuroImage. Mathematics in Brain Imaging* **23**, S208–S219. issn: 1053-8119 (1st Jan. 2004).

6.6. References

22. Andersson, J. L. R. & Sotiroopoulos, S. N. An Integrated Approach to Correction for Off-Resonance Effects and Subject Movement in Diffusion MR Imaging. *NeuroImage* **125**, 1063–1078. issn: 1053-8119 (15th Jan. 2016).
23. Garyfallidis, E. *et al.* Dipy, a Library for the Analysis of Diffusion MRI Data. *Frontiers in Neuroinformatics* **8**. issn: 1662-5196 (2014).
24. Self, M. W., van Kerkoerle, T., Goebel, R. & Roelfsema, P. R. Benchmarking Laminar fMRI: Neuronal Spiking and Synaptic Activity during Top-down and Bottom-up Processing in the Different Layers of Cortex. *NeuroImage* **197**, 806–817. issn: 1053-8119 (15th Aug. 2019).
25. Muckli, L. *et al.* Contextual Feedback to Superficial Layers of V1. *Current Biology* **25**, 2690–2695. issn: 0960-9822 (19th Oct. 2015).
26. Waehnert, M. D. *et al.* Anatomically Motivated Modeling of Cortical Laminae. *NeuroImage. In-Vivo Brodmann Mapping of the Human Brain* **93**, 210–220. issn: 1053-8119 (1st June 2014).
27. Dale, A. M., Fischl, B. & Sereno, M. I. Cortical Surface-Based Analysis: I. Segmentation and Surface Reconstruction. *NeuroImage* **9**, 179–194. issn: 1053-8119 (1st Feb. 1999).
28. Piskunowicz, M. *et al.* A New Technique with High Reproducibility to Estimate Renal Oxygenation Using BOLD-MRI in Chronic Kidney Disease. *Magnetic Resonance Imaging* **33**, 253–261. issn: 0730-725X (1st Apr. 2015).
29. Milani, B. *et al.* Reduction of Cortical Oxygenation in Chronic Kidney Disease: Evidence Obtained with a New Analysis Method of Blood Oxygenation Level-Dependent Magnetic Resonance Imaging. *Nephrology Dialysis Transplantation* **32**, 2097–2105. issn: 0931-0509 (1st Dec. 2017).
30. Dawe, R. J., Bennett, D. A., Schneider, J. A., Vasireddi, S. K. & Arfanakis, K. Post-mortem MRI of Human Brain Hemispheres: T2 Relaxation Times during Formaldehyde Fixation. *Magnetic Resonance in Medicine* **61**, 810–818. issn: 1522-2594.
31. Van der Kolk, A. G. *et al.* Imaging the Intracranial Atherosclerotic Vessel Wall Using 7T MRI: Initial Comparison with Histopathology. *American Journal of Neuroradiology*. issn: 0195-6108, 1936-959X. pmid: 25477359 (4th Dec. 2014).

Chapter 7

Conclusion

Science happened